

**MICROMACHINED PIEZOELECTRIC-ON-SILICON PLATFORM
FOR RESONANT SENSING AND ENERGY HARVESTING**

A Dissertation
Presented to
The Academic Faculty

by

Jenna L. Fu

In Partial Fulfillment
of the Requirements for the Degree
Doctor of Philosophy in the
School of Electrical and Computer Engineering

Georgia Institute of Technology
August 2013

Copyright © 2013 by Jenna L. Fu

**MICROMACHINED PIEZOELECTRIC-ON-SILICON PLATFORM
FOR RESONANT SENSING AND ENERGY HARVESTING**

Approved by:

Professor Farrokh Ayazi, Chair, Advisor
School of Electrical and Computer Engineering
Georgia Institute of Technology

Professor Ying Zhang
School of Electrical and Computer Engineering
Georgia Institute of Technology

Professor Mark G. Allen
School of Electrical and Computer Engineering
Georgia Institute of Technology

Professor Michael H. Bergin
Schools of Civil and Environmental Engineering
and Earth and Atmospheric Sciences
Georgia Institute of Technology

Professor Oliver Brand
School of Electrical and Computer Engineering
Georgia Institute of Technology

Date Approved: June 25, 2013

To my parents,

Ta-Wei and Hui-Ying Chen Fu

ACKNOWLEDGMENTS

It would be impossible to convey in writing all that I have gained from this experience, but I do have many people to thank for accompanying me throughout this phase of life and contributing to my development as a researcher and person.

I would first like to express my sincere appreciation and gratitude to Dr. Farrokh Ayazi for his advising and mentorship over the past several years. In spite of my slowness, he continually encouraged me to do and think far beyond my own perceived capabilities. I greatly admire his passion, dedication, and excellence as a leading expert and worldwide authority in his field. I hope to be a good ambassador of all the valuable lessons learned while under his guidance.

I am grateful to Drs. Mark Allen, Oliver Brand, and Ying Zhang for devoting their time to my proposal and defense, as well as Dr. Mike Bergin for taking an interest in my research and serving on my defense committee in the midst of summer travels. I gained valuable insight and learned immensely from all committee members in my time spent with them. I also thank Jin-Jyh Su and Chris Carron for their generosity of time and resources that enabled me to generate valuable experimental results for this thesis.

None of this research could have materialized without the Georgia Tech IEN cleanroom staff: Gary Spinner, Vinny Nguyen, Eric Woods, Jason Herrington, Ben Hollerbach, John Pham, Charlie Suh, Thomas Averette, Mikkel Thomas, and the dedicated staff who work so hard to maintain a top-notch research environment for hundreds of users. I especially thank scientists David Gottfried and Walter Henderson for never hesitating to lend a helping hand with often finicky tools that I tried to use for unconventional purposes.

What an incredible opportunity to interact with such brilliant and diverse colleagues in the IMEMS group! I've learned so much from past members, who laid the foundations for our research, as well as current members with whom I had the privilege to work and become great friends. Thanks to Drs. Reza Abdolvand, JD Fang, Wanling Pan, and Mina Rais-zadeh for getting me started in the cleanroom/lab; Dr. Milap Dalal, impending-Drs. Logan Sorenson and Roozbeh Tabrizian for the amazing collaborations and fun times; long-time friends Xin Gao, Diego Emilio, Handsome Wang, Dr. Ashwin, and newer "masters students" Arashk N., Yaesuk Jeong, and P. Liu. I will forever cherish our time together and look forward to the next IMEMS reunion.

I'm thankful to still be in touch with friends from my earlier years in WV and CMU undergrad; it's truly exciting to see how far we've all come. I'd also like to acknowledge friends made in Atlanta during my graduate career: Ian Yang, Rama Ravindran, Ryan Westafer, Sarah Bryan (Reynoso), Kevin Brenner, Farhana Zaman, Zac Lochner, Shuodan Chen, Wenjun Xu, Hakan Töreyn, Luke Beardslee, Spyros Pavlidis, Hommood Al-Rowais, and the MiRC community for amazing times and fruitful research discussions; TSRB buddies Negar Tavassolian, Ken Chiu, Devangi Parikh, David Chung, Haewon Park, Adilson Cardoso, Stan Phillips, Jung, Shubha Ramakrishnan, Degs, and Scott Koziol; swing dance friends Jon Scholz, John Bustamante, Arya Irani, Kate Bennett, Tobias Kunz, Amber Rumble, Briana Sell, Matthew Habib, and Richard Roberts; roommates Bhavna Kumar, Shabana Charaniya, Stephanie Mma, Shannon Statham, and Fidela Chiang, who provided essential female support for a Georgia Tech engineer; Mathias Henry, Mike Joe, Daniel Yao, Tinny Washington, Bruce Chou, Mu Wei, Lee and Mike Lo, and so many more. It has been a joy to share life with you all.

I've been blessed with a family that has loved me unconditionally from the beginning. I thank my grandparents and parents for teaching me to do everything with integrity, humility, and loyalty through their own living examples. Growing up wouldn't have been half the fun without my big sisters Angela and Julia, and their other halves Dave and Christian. Also, I cannot thank Kevin Chan enough for going through this arduous process before I did, providing much-needed support and encouragement with patience, and perhaps most difficult of all, giving practical advice at times that it would be difficult to do so.

None of this would have been possible without God, who has given me daily peace and strength outside my own abilities to complete this journey while providing direction and guidance to begin a new chapter of life.

“Trust in the Lord with all your heart and lean not on your own understanding; in all your ways acknowledge Him, and He will make your paths straight.” - Proverbs 3:5-6

TABLE OF CONTENTS

ACKNOWLEDGMENTS	iii
LIST OF TABLES	ix
LIST OF FIGURES	x
SUMMARY	xvi
1 INTRODUCTION	1
1.1 Sensor System Overview	1
1.2 Current Micro-Sensing Technology	3
1.2.1 Relative Humidity and Temperature (RH&T) Sensors	3
1.2.2 Commercial Portable Environmental Sensors	4
2 RESONANT MICROSENSORS.....	9
2.1 Gravimetric Resonators	9
2.2 Resonator Transduction Methods	11
2.2.1 Capacitive and Thermal Actuation	11
2.2.2 Piezoelectric Transduction.....	12
2.3 Piezoelectric Acoustic Wave Micro-Devices	13
2.3.1 Piezoelectric Materials.....	13
2.3.2 Piezoelectric Micro-Resonators	13
2.4 Sensor Implementation Challenges.....	15
3 THIN-FILM PIEZOELECTRIC-ON-SILICON MICRO-PLATFORM.....	16
3.1 Platform Overview	16
3.2 Fabrication Process Flow	18
3.2.1 Choice of Piezoelectric Material.....	18
3.2.2 ZnO-on-Si Fabrication Process Flow.....	19
3.2.3 AlN-on-Si Fabrication Process Flow	22
3.3 Materials for Sorption-Based Micro-Sensing	24
3.3.1 Porous Materials and Frameworks.....	24
3.3.2 Polymeric Materials	25

4	TPOS GRAVIMETRIC RESONANT SENSORS	27
4.1	TPoS Resonator With Annexed Platforms	28
4.2	ZnO-on-Si Resonant Temperature and Humidity Sensor	30
4.2.1	Temperature and Humidity Effects on Resonance Frequency	30
4.2.2	Resonant Temperature and Humidity Sensing	31
4.2.3	Functionalization Process for Humidity Sensing.....	32
4.2.4	Sensor Measurement and Characterization.....	34
4.3	AlN-on-Si Resonant VOC Sensor	39
4.3.1	Sensor Design and Optimization	39
4.3.2	Functionalization for Toluene and Xylene Sensing.....	44
4.3.3	Experimental Setup and Sensor Measurement Results.....	47
4.3.4	Humidity Effects on VOC Measurements	50
5	TPOS DUAL-MODE RESONATORS AND OSCILLATORS FOR TEMPERATURE MEASUREMENT	53
5.1	Dual-Mode Temperature Measurement.....	54
5.1.1	Principle of Operation.....	54
5.1.2	Dual-Mode Oscillator Considerations	55
5.1.3	TPoS Dual-Mode Resonators	57
5.2	ZnO-on-Si Dual-Mode Oscillator	58
5.2.1	System Architecture.....	58
5.2.2	Dual-Mode Resonator Design.....	59
5.2.3	Interface Circuitry	60
5.2.4	Oscillator Measurement and Characterization.....	62
5.3	Optimized AlN-on-Si Dual-Mode Resonators.....	66
5.3.1	Limitations of Fundamental and Higher-Order Modes	66
5.3.2	TCF _b Enhancement By Beat Frequency Reduction.....	67
5.3.3	Effect of Orientation on WS/WE Resonator TCF	73
5.3.4	Dual-Mode Excitation for Temperature-Stable Beat Frequency	75
6	TOWARDS INTEGRATED MICROMECHANICAL KINETIC ENERGY HARVESTING.....	77
6.1	Multi-Degree-of-Freedom Energy Harvesting	77
6.2	Mechanical Frequency Upconversion.....	77

6.3	AlN-on-Si MEMS Kinetic Energy Harvesters	78
6.3.1	Out-of-Plane Energy Harvester.....	79
6.3.2	In-Plane Energy Harvester	80
6.4	Fabrication Process Integration.....	81
6.5	KEH Device Characterization.....	84
6.5.1	Out-of-Plane Energy Harvester.....	85
6.5.2	In-Plane Energy Harvester	86
7	CONCLUSIONS AND FUTURE DIRECTIONS.....	90
7.1	Technical Contributions.....	90
7.2	Future Work	92
7.2.1	Wafer-Level Sensor Functionalization and Optimization	92
7.2.2	Wafer-Level Packaging For TPoS Micro-Platform.....	92
7.2.3	Energy Harvester Reliability And Performance Optimization	93
7.2.4	Energy Harvester Implementation and Interfacing.....	94
	REFERENCES	96

LIST OF TABLES

Table 1.1: Comparison of commercial RH&T micro-sensors.....	3
Table 3.1: Parameters used for ZnO RF sputter deposition in the Georgia Tech IEN cleanroom.	21
Table 4.1: Change in frequency and Q vs. RH.	50
Table 4.2: Comparison of resonant toluene sensors in literature.....	52
Table 5.1: Summary of WS/WE mode DM resonator performance.....	70

LIST OF FIGURES

Figure 1.1:	Schematic diagram of basic sensor operation, where an electrical signal is produced in response to an external stimulus.	2
Figure 1.2:	(a) Diagram of a Figaro gas sensor; (b) potential barrier after adsorbing a reducing gas.	7
Figure 1.3:	Schematic diagram of a CO ₂ NDIR sensor.	8
Figure 2.1:	Silicon resonators utilizing (a) capacitive [22], (b) thermal [24], and (c) piezoelectric actuation [25].	12
Figure 2.2:	Piezoelectric resonant sensors based on (a) bulk/thickness shear (quartz and FBAR with piezoelectric material sandwiched between metal electrodes), (b) surface (SAW device with interdigitated electrodes on a piezoelectric substrate), and (c) flexural (cantilevers with piezoelectric stack deposited on a structural material).	14
Figure 3.1:	Schematic diagram of integrated micro-platform consisting of TPOs gravimetric resonant sensors and kinetic energy harvesting (KEH) devices.	17
Figure 3.2:	Scanning electron microscope (SEM) image of released ZnO-on-Si resonator and accompanying process flow.	20
Figure 3.3:	Typical XRD rocking curve (ω) scan to confirm <i>c</i> -axis orientation of ZnO sputtered in the Georgia Tech Pettit cleanroom facility.	21
Figure 3.4:	Fabrication process flow for AlN-on-Si resonant sensors: (a) top Mo patterning; (b) backside oxide mask patterning and AlN etch to expose bottom Mo; (c) device Si trench definition; and (d) handle Si and BOX layer removal.	23
Figure 4.1:	Diagram of AlN-on-Si resonant sensor with annexed platforms.	28
Figure 4.2:	(a) ANSYS mode shape of gravimetric sensor with annexed platforms; (b) comparison of relative modal displacement between conventional LE sensor and sensor with platforms.	29
Figure 4.3:	ANSYS mode shapes of ZnO-on-Si sensors at (a) f_1 and (b) f_3 ; $L = 120 \mu\text{m}$, $W = 120 \mu\text{m}$	31
Figure 4.4:	(a) Patterns deposited using a Jetlab II tool. Colored rings indicate thickness variations as confirmed by Wyko optical profilometer measurement (inset); (b) patterns deposited with the Bioforce Nano eNabler, showing minimal thickness variations.	32

Figure 4.5:	(left) Optical image of PEI-loaded SPT with stuck platform (H ₂ O evaporated mid-deposition); (right) close-up views of SPT reservoir (inset) with dried PEI and clogged channel.	33
Figure 4.6:	(a) Optical image of ZnO-on-Si humidity sensor functionalized with PEI; (b) frequency response of PEI-patterned RH sensor; $f_{l,RH} = 37$ MHz, $Q = 1340$ in air.	34
Figure 4.7:	Temperature response of $f_{b,ref}$ at constant RH.	35
Figure 4.8:	RH sensitivity of beat frequency $f_{b,ref}$ and $f_{b,RH}$ over temperature.	36
Figure 4.9:	Sensor response after thermal compensation.	37
Figure 4.10:	Sensor f_l response to RH prior to thermal compensation.	37
Figure 4.11:	Sensor response to RH increase from 20 to 40 %RH at 25°C.	38
Figure 4.12:	Frequency response measurements of 16-MHz sensor: (left) optimized sensing mode with platforms and central block in phase and (right) lower sensitivity mode with platforms out of phase with central block.	39
Figure 4.13:	Simulated and measured mass sensitivity of 16-MHz sensor ($L = 168$ μ m, $W = 80$ μ m, $L_p = 40$ μ m); measured data for 0 pg, 368 pg, and 737 pg of mass loading; (inset left) measured sensor frequency response; (inset right) close-up SEM image of FIB-deposited Pt on annexed platform.	40
Figure 4.14:	Simulated mass sensitivity of 19-MHz sensor ($L = 156$ μ m, $W = 206$ μ m, $L_p = 30$ μ m) with reduced R_m compared to 16-MHz sensor.	41
Figure 4.15:	Wide-span frequency response for (a) 16-MHz sensor (inset: optical image); (b) 19-MHz sensor with improved IL and spurious suppression. Peaks within 5 dB IL of f_0 have 180° phase shift (inset: optical image of fabricated device).	43
Figure 4.16:	Optical images of Nano eNabler patterning trials with various PIB solutions: (a-c) 0.1% PIB/xylene solution with no DEP added, showing quick evaporation of a micro-pipetted drop in 3 minutes; (d-f) 1:1 ratio of 2% PIB/toluene to DEP. Optical images over a 10-minute time period show very little polymer remaining upon DEP evaporation.	45
Figure 4.17:	(a) SEM image of unpatterned AlN-on-Si sensor; (b) optical image of sensor during PIB patterning (SPT shown above right platform); (c) optical image of PIB-patterned sensor; (d) Olympus	

	LEXT thickness profile of PIB on platforms (z -axis exaggerated to clearly illustrate PIB pattern shape).	46
Figure 4.18:	Measured frequency response before and after PIB patterning; (b) photo of customized test board for VOC sensor testing.	46
Figure 4.19:	Measured frequency change for toluene concentrations of 20600 ppm, 14400 ppm, 7200 ppm, and 3600 ppm.	48
Figure 4.20:	Measured change in Q vs. toluene concentration for sensing mode f_0 compared to 29-MHz mode f_1 ; arrows denote platform motion.	48
Figure 4.21:	Measured frequency change for xylene concentrations of 6250 ppm, 5000 ppm, 3750 ppm, 2500 ppm, and 1250 ppm.	49
Figure 4.22:	Measured change in Q vs. xylene concentration for f_0 and f_1 (for comparison).	49
Figure 4.23:	Measured frequency change for xylene concentrations of 6250 ppm, 5000 ppm, 3750 ppm, 2500 ppm, and 1250 ppm.	50
Figure 4.24:	Measured change in Q vs. relative humidity (RH) for f_0 and f_1 of PIB-coated sensor.	50
Figure 5.1:	(a) Single-loop Colpitts oscillator with one-port resonator; (b) dual-loop DM oscillator with two-port MEMS resonator in feedback with TIAs followed by mixing, multiplication, and filtering blocks to generate output frequency f_b	56
Figure 5.2:	Block diagram of dual-mode (DM) interface and readout architecture for ZnO-on-Si BAW resonator.	58
Figure 5.3:	ZnO-on-Si BAW mode shapes at f_1 and f_3	59
Figure 5.4:	SEM image and frequency response of ZnO-on-Si DM resonator.	60
Figure 5.5:	Schematics of interface ICs for f_1 (left) and f_3 (right).	61
Figure 5.6:	(top) Measured oscillator response for f_1 and f_3 SM excitation; (bottom left) DM excitation at f_1 and f_3 ; (bottom right) DM output signal after averaging.	62
Figure 5.7:	(top) Spectral response for f_1 and f_3 SM excitation; (bot.) DM excitation with f_{mix} at 57.3 MHz.	63
Figure 5.8:	Measured f_3 phase noise response in SM and DM configuration.	64
Figure 5.9:	Measured temperature response of (a) f_1, f_3 ; (b) f_b	65

Figure 5.10: Measurement correlation (R^2) vs. Q_{min}	65
Figure 5.11: (left) strain distribution for DM AlN-on-Si resonator based on first and third width-extensional (WE/WE3) modes; (right) simulated f_b vs. support width for a 27-MHz resonator ($W = 156 \mu\text{m}$).....	67
Figure 5.12: Measured f_b vs. length L for AlN-on-Si WE/WE3 resonator; (inset) SEM image of device with interdigitated electrodes to excite WE and WE3 modes.	67
Figure 5.13: ANSYS mode shapes of width-shear (WS) and WE modes for dual-mode operation.....	68
Figure 5.14: Simulated frequency of width-shear (WS) and WE modes vs. L for $W = 156 \mu\text{m}$, corresponding to $f_{WE} = 27 \text{ MHz}$	68
Figure 5.15: Measured vs. simulated f_b for WS/WE resonator designs with $W = 156 \mu\text{m}$, L varied to modify f_b values ($f_b = f_{WS} - f_{WE}$); (inset) SEM image of WS/WE resonator ($W = 156 \mu\text{m}$, $L = 204 \mu\text{m}$).....	69
Figure 5.16: Extracted $\text{TC}f_b$ of WS/WE DM resonator with $f_b = 17 \text{ kHz}$; measured $\text{TC}f_{WS} = -30.1 \text{ ppm}/^\circ\text{C}$, $\text{TC}f_{WE} = -31.1 \text{ ppm}/^\circ\text{C}$	70
Figure 5.17: Measured response of DM resonators with $ f_b = 1.5 \text{ MHz}$ and 134 kHz ($ f_b = f_{WS} - f_{WE} $), showing Q_{WE} degradation when f_{WS} and f_{WE} converge.	71
Figure 5.18: WS/WE DM terminal configurations: (a) dual-loop oscillator with two-port operation; (b) two separate one-port oscillators, which provide better isolation of each mode.	72
Figure 5.19: Measured $\text{TC}f_{WS}$ and $\text{TC}f_{WE}$ for [100]-aligned WS/WE resonator, exhibiting $2\times$ larger ΔTCF than [110]-aligned devices; (inset) SEM image of [100]-aligned resonator.....	74
Figure 5.20: Measured response of [100]-oriented WS/WE resonator with $f_b = 120 \text{ kHz}$ ($W = 156 \mu\text{m}$, $L = 268 \mu\text{m}$).	74
Figure 5.21: Measured response for f_{WS} and f_{WE} of [100]-aligned resonator with $f_b = 1.5 \text{ MHz}$ and near-zero $\text{TC}f_b$ ($W = 156 \mu\text{m}$, $L = 242 \mu\text{m}$).....	76
Figure 5.22: Extracted $\text{TC}f_b$ of [100]-aligned WS/WE DM resonator with nearly temperature-stable f_b	76
Figure 6.1: Schematic diagrams depicting conversion mechanism in previously reported MEMS resonant kinetic energy harvesters: (a)	

	without mechanical frequency upconversion [112]; (b) with mechanical frequency upconversion [113].	78
Figure 6.2:	Backside view of a silicon die with in-plane and out-of-plane kinetic energy harvesters fabricated side-by-side.	79
Figure 6.3:	Out-of-plane harvester mode shapes ($f_{mass} = 149$ Hz and $f_{beam} = 13.7$ kHz) and basic principle of operation.	79
Figure 6.4:	Conceptual diagram of in-plane harvester: (a) rest position, (b) side view of low-frequency seismic mass vibration, (c) side view of high-frequency spring transducer vibration.	80
Figure 6.5:	Spring transducer strain patterns showing charge formation for in-plane modes at 2.23 kHz (upper) and 6.24 kHz (lower).	81
Figure 6.6:	Cross-section view of TPoS sensors and energy harvesters on SOI substrate.	82
Figure 6.7:	Static structural simulation showing 260- μ m thick seismic mass deflection resulting from 1g gravitational acceleration, demonstrating the need for shock stops to maintain in-plane alignment with μ -picks.	82
Figure 6.8:	SEM images of out-of-plane harvester. AlN and top Mo are patterned to sense the fundamental clamped-clamped beam mode, exposing bottom Mo in the beam center.	83
Figure 6.9:	(a) SEM image of in-plane harvester z -shock stop removed to show seismic mass formed by handle Si; (b) SEM image of intact shock stop resting on handle Si (anchored to substrate); (c) SEM image of μ -picks and spring transducer; (d) backside optical view of entire device.	83
Figure 6.10:	Schematic of KEH device measurement setup for out-of-plane harvesters and in-plane harvesters. A vertical shaker table (MB Dynamics, Inc.) was used for out-of-plane testing while an accelerometer setup (built in-house by former colleagues) was utilized for in-plane testing.	84
Figure 6.11:	Optical images indicating electrical connections made to testing setup: (a) all top electrodes of the out-of-plane harvester were wirebonded for testing; (b) a single spring transducer of the in-plane harvester was connected.	84
Figure 6.12:	Out-of-plane beam transducer output at $a_{in} = 0.3$ g, $a_{in} = 0.5$ g, and $a_{in} = 0.7$ g.	85

Figure 6.13:	Out-of-plane beam transducer output with periodic upconversion spikes; (inset) close-up view of signal ring-down with 12kHz spectral component.....	86
Figure 6.14:	In-plane spring transducer output at various accelerations ($R_L = 560 \Omega$).	87
Figure 6.15:	In-plane spring transducer output with upconversion spikes ($R_L = 560 \text{ k}\Omega$); (inset) close-up view of 7 kHz signal ring-down.	88
Figure 6.16:	Measured peak power vs. R_L for in-plane harvester.	89
Figure 7.1:	SEM image of in-plane harvester with mis-aligned shock stop.....	93
Figure 7.2:	Schematic diagram of a MEMS energy harvesting system describing the process of harvesting ambient mechanical energy with a micro-mechanical system, converting it to usable electrical energy by various transduction mechanisms, and processing it for storage and eventual delivery.....	95

SUMMARY

This dissertation presents a microelectromechanical systems (MEMS)-based environmental monitoring platform comprising silicon-based, piezoelectrically-actuated resonant sensors and kinetic energy harvesters. All devices are realized using thin-film piezoelectric-on-substrate (TPoS) technology, which provides a path to integrate various functionalities on a single substrate with MEMS components. TPoS resonators, which exhibit high quality factors (Q s) in air, are suitable for sensing when access to the outside world is required. The low-power operation of TPoS oscillators further qualifies such a platform for mobile and portable systems.

To validate the TPoS platform, gravimetric humidity sensing is demonstrated with thermally-corrected output response by an uncoated “reference” temperature sensor. Also presented are AlN-on-Si sensors for toluene and xylene, which are pollutants of great importance for indoor and outdoor air quality as well as health screenings. Silicon dual-mode resonators and oscillators for self-temperature sensing are also explored. Dual-mode thermometry exploits the inherent frequency-temperature dependence of silicon to accurately and locally measure device temperature, forming an essential building block of highly stable oscillators and sensors.

Multi-axis kinetic energy harvesting (KEH) devices with integrated frequency-upconverting transducers are introduced. Devices are micromachined on the same substrate as TPoS resonant sensors and have an individual volume in mm^3 , enabling applications in wireless autonomous sensor nodes. In remote locations where continuous operation may be required, TPoS energy harvesters can provide battery replacement or recharging alternatives that do not increase overall system size.

1 INTRODUCTION

The world contains an abundance of sophisticated sensors that transform external stimuli into useful information. All living organisms are sensitive to aspects of the external environment, such as light, temperature, vibration, electric fields, and biomolecules. Besides natural sensors, we interact with countless man-made sensors every day. For example, industrial processes require continuous monitoring of temperature, humidity, and other parameters, while today's automobiles are equipped with sensors that control emissions levels, deploy airbags, and regulate cabin climate. Additionally, smart buildings have sustainable features and sensing systems that conserve energy while maintaining a healthy indoor environment for all users.

The increasing ubiquity of mobile devices in today's society has increased the demand and potential for miniaturized, integrated sensors. Each generation of smartphone has provided users with enhanced experiences via gaming, navigation, and various location-based services, many of which utilize microelectromechanical systems (MEMS) devices. The versatility of micromachining technology has opened the door to additional functionalities that have yet to be fully explored.

1.1 SENSOR SYSTEM OVERVIEW

A complete sensor system comprises several functional blocks (Figure 1.1), the first of which is typically a filter/pre-conditioner that collects and prepares the chemical, biological, or physical analyte for measurement. This interface with the surrounding environment is coupled to a transducer that transforms the analyte to a measurable signal. Post-transduction data requires mixing or amplifying via conditioning circuitry. Finally, the output module produces a quantity that can be easily interpreted by the user (e.g.

voltage, frequency) [1]. This thesis focuses on the micro-scale transducers that convert the analyte to an electrical signal, while considering the effects of device performance on oscillator interface circuitry used to generate sensor readout.

Sensors are typically characterized by the following metrics: *sensitivity*, the ratio of change in sensor output to a change in analyte; *resolution*, the minimum detectable change in analyte quantity at the sensor output; and *selectivity*, or the capability of distinguishing one analyte from another [2]. Although most sensing applications require high sensitivity, low resolution, and high selectivity, the exact specifications are application-dependent. For example, ultra-stable reference oscillators benefit from the highest sensitivity, lowest resolution thermometers to compensate for thermal effects on frequency, while consumer applications can sacrifice sensitivity or resolution to enable portability and low-power operation. Selectivity, which becomes challenging for environmental monitors, can be addressed by implementing sensor arrays.

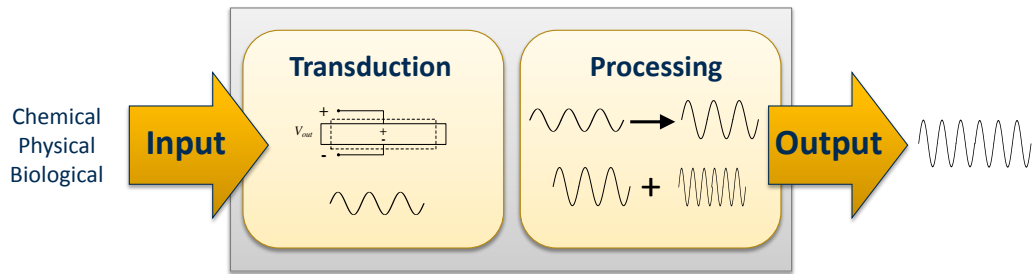


Figure 1.1: Schematic diagram of basic sensor operation, where an electrical signal is produced in response to an external stimulus.

1.2 CURRENT MICRO-SENSING TECHNOLOGY

1.2.1 RELATIVE HUMIDITY AND TEMPERATURE (RH&T) SENSORS

Chemical and biological microsensors were predicted to enter the mobile phone market in 2014-2015 via portable health and air quality monitoring applications [3]. While micromachined inertial and pressure sensors have become standard amenities in many of today's mobile devices, the various challenges associated with environmental sensor integration have yet to be thoroughly addressed. This year, however, marks a milestone for miniaturized environmental monitors: the Samsung Galaxy S4, top-rated by Consumer Reports within a month of its release [4], touted the integration of Sensirion's latest single-chip relative humidity and temperature (RH&T) sensor among numerous attractive features. A comparison of commercial RH&T micro-sensing technology provides insight into Sensirion's success cracking the consumer market (Table 1.1).

Table 1.1: Comparison of commercial RH&T micro-sensors.

Company	Temp. Sensor	ΔT [°C]	RH Sensor	ΔRH [% RH]	Volume [mm ³]	Electronics Integration	Unit Price
IST	Pt1000	± 2	Capacitive	± 1.5 (15–90%)	$4 \times 2 \times 0.4$	None	£16.76
GE	Bandgap	± 0.6 to 3	Capacitive	± 2 (20–80%)	$9.5 \times 6 \times 3.2$	SoC	\$6-11
Honeywell	Bandgap	± 1	Capacitive	± 4	$4.9 \times 3.9 \times 1.9$	SoC	\$10-18
Silicon Laboratories	Bandgap	± 1 (0–70%)	Capacitive	± 4.5 (20–80%)	$4 \times 4 \times 0.9$	Monolithic	\$7-8
Sensirion	Bandgap	± 0.4 (10–60°C)	Capacitive	± 4.5 (20–80%)	$2 \times 2 \times 0.8$	Monolithic	\$20

Information obtained from digikey.com and official company websites. Unit price range provided for 1 to 1000 parts (if possible) except for Sensirion, which currently only sells parts in quantities of 50,000.

Most RH&T chips employ similar principles of operation: humidity sensing is achieved by a thin-film polymer capacitor that changes dielectric constant with absorbed or

desorbed moisture, while a silicon diode band-gap circuit performs on-chip thermometry (in IST's device, a platinum resistance temperature detector is used). What truly separates one generation of sensors from the next is the level of system integration. IST sells a combined RH&T sensor but the discrete interface electronics dramatically increase system footprint. GE and Honeywell's sensors and circuits, although separate entities, are co-located in a single system-on-chip (SoC) package to eliminate performance issues resulting from discrete components. Silicon Laboratories and Sensirion, however, take a monolithic approach to achieve single-chip RH&T solutions small enough to fit in a mobile phone. Sensirion's technology seamlessly integrates sensors with CMOS analog and digital signal processing circuitry on the same silicon substrate, enabling a low-power, high-performance system that occupies 4× less area than the already-small Silicon Laboratories chip.

Samsung utilizes the RH&T sensor to display optimum comfort and fitness levels for users, which only scratches the surface of beneficial smartphone apps. Temperature and humidity measurement are fundamental to any multi-sensing platform that discerns chemical compounds and bio-molecules with varying complexity, much like an electronic nose ("e-nose") [5, 6]. Proper tracking of temperature and humidity in conjunction with important target gases would enable smartphones to not only assess local environmental conditions but also provide information specific to each user.

1.2.2 COMMERCIAL PORTABLE ENVIRONMENTAL SENSORS

Although the term "environmental sensing" initially conjures images of meteorological forecasting, assessment of one's surroundings based on various environmental parameters is in fact required by a wide spectrum of applications. Because

smartphones travel everywhere with their owners, mobile devices provide a unique platform to implement functionalities that benefit individuals and society on a larger scale. Health and safety ratings for outdoor air are currently provided from stationary locations; however, mobile phone monitoring would enable users to obtain local and customized information depending on their sensitivity to certain contaminants.

Various measures have been taken in the last few decades to reduce emissions, but unhealthy air still persists in many areas of the country and around the world. The U.S. Environmental Protection Agency (EPA) defined exposure standards for common air pollutants considered harmful to public health and the environment: carbon monoxide (CO), nitrogen dioxide (NO₂), ozone (O₃), particulate matter, and lead [7]. Development of a portable system to monitor the gaseous compounds would be particularly beneficial to residents in urban and industrialized locations.

While a person's choice of activities could be positively influenced by personalized advice about outside air, time spent indoors often exceeds durations of outdoor exposure. According to comprehensive EPA studies [8], volatile organic compounds (VOCs) from both natural and man-made processes have been linked to both acute and chronic adverse health effects. Indoor concentrations are on average 2 to 5 times higher and even up to 10x higher, regardless of location (rural or industrial). Additionally, elevated concentrations can persist in the air long after a compound-containing product is used. Aside from indoor air quality (IAQ) concerns, VOCs can form explosive mixtures in air (at high enough concentrations) and have been identified as precursors to formation of low-level ozone [9], which reduces agricultural yield and

overall outdoor air quality [10]. In conjunction with temperature and humidity, VOC levels also strongly influence indoor air quality [11].

Portable integrated micro-sensors can be used to provide built-in health and safety features. While technology will never substitute for face-to-face interaction with medical professionals, previous costly and invasive screenings may be quickly performed by devices equipped with smart sensors. Recent examples of great interest include detecting compounds in the breath with lung cancer signatures [12] or even public safety risks such as drunk driving, which could be prevented by a “smartphone breathalyzer” capable of determining dangerous levels of ethanol.

While monolithic RH&T sensors have successfully achieved size and power reduction without sacrificing performance, the CMOS-only platform is limited by the lack of flexibility to integrate different sensing methods required for gas and chemical detection. The most common VOC and gas sensing methods in commercial devices are described in the following two sections.

Semiconductor (Potentiometric) Gas Sensors

Potentiometric gas sensors, which determine the amount of analyte adsorbed onto a sensitive material by measuring changes in electric potential, are realized using n-type thick films such as tin dioxide (SnO_2) (Figure 1.2a). SnO_2 adsorbs negatively-charged oxygen atoms onto the surface when heated, forming a potential barrier against current flow and generating a high resistance R_s in fresh air. When reducing gases adsorb onto the sensor surface, the potential barrier—and therefore R_s —is decreased significantly (Figure 1.2b) [13]. The target gas concentration C is determined using

$$R_s = A[C]^{-\alpha}, \quad (1)$$

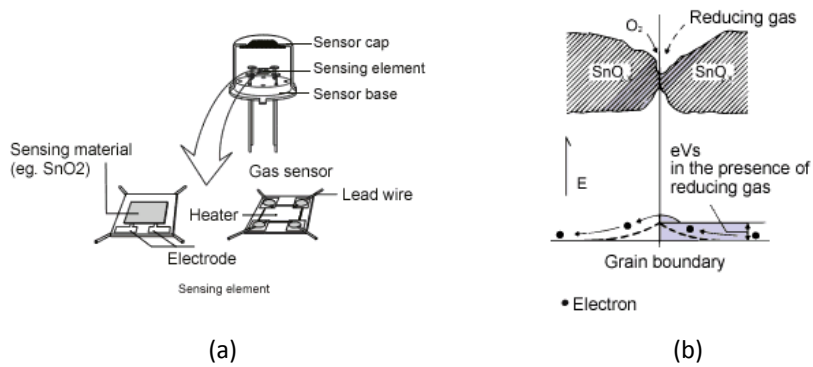


Figure 1.2: (a) Diagram of a Figaro gas sensor; (b) potential barrier after adsorbing a reducing gas.

where A is a constant and α is given by the slope of the R_s curve. Potentiometric sensors have had commercial success for more than 30 years because of their simple thick-film fabrication process and relatively long lifetimes. However, varying temperature and humidity conditions as well as ambient oxygen concentration can affect sensitivity characteristics. To maintain the sensing substrate at a constant temperature, solid-state sensors are equipped with on-chip heaters that require additional power consumption. Potentiometric sensors can have poor selectivity because any reducing gas in the environment can affect the measured conductivity of a metal oxide sensing film.

Non-dispersive Infrared (NDIR) Gas Sensors

NDIR is commonly used for carbon dioxide (CO₂) and certain hydrocarbons that are difficult to detect by other methods. NDIR addresses the selectivity and sensitivity problems with potentiometric sensing by utilizing the specific IR absorption properties of gases. A typical NDIR sensor consists of an emitter source that generates infrared (IR) radiation, a sample cell or chamber through which the gas is directed, and an IR detector at the opposite end to measure the amount of light absorbed by the gas (Figure 1.3) [14].

Gas concentration P is determined using Beer's Law

$$I = I_0 e^{kP}, \quad (2)$$

where I is the light intensity measured by the detector, I_0 is the “reference” light intensity in an empty sample chamber, and k is a system-dependent constant. Any wavelengths not absorbed by the target gas are filtered out before light reaches the detector, enabling highly sensitive and selective detection. However, temperature and humidity variations may still create cross-sensitivity issues in NDIR sensors. Additionally, it is costly and difficult to scale NDIR optics for integration purposes. The only MEMS-based NDIR sensor components fabricated to-date (ICx Photonics, Inc. [15]) are not yet commercially available.

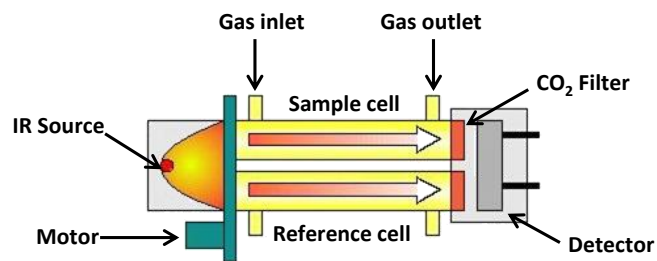


Figure 1.3: Schematic diagram of a CO₂ NDIR sensor.

2 RESONANT MICROSENSORS

Based on the current state of the art in commercial micro-sensing technology, scalability, environmental sensitivity, and integration potential are the main bottlenecks in realizing mobile-friendly systems for trace gas and chemical detection. Devices should be inexpensive to manufacture, yet maintain robust performance with scaling. As illustrated by successful commercial sensors (e.g. Sensirion), the sensing element must ultimately be combined with electronics and signal processing units through monolithic or CMOS-compatible integration. Resonant micro-devices, which provide a frequency output that can be digitally measured with high accuracy [16], meet the aforementioned requirements in terms of integration potential and are strong candidates for implementation of a miniaturized multi-sensing platform.

2.1 GRAVIMETRIC RESONATORS

The model for mechanical resonance in a basic mass-spring system with spring constant k , mass m , and no damping is given by (3), where f_0 represents the system natural frequency:

$$f_0 = \frac{1}{2\pi} \sqrt{\frac{k}{m}}. \quad (3)$$

Thus, modulation of resonator properties such as stiffness or mass will induce a frequency shift. Provided that mass change dominates over stiffness change, Δf due to mass loading can be approximated by

$$\Delta f \cong -\frac{1}{2} f_0 \frac{\Delta m}{m}, \quad (4)$$

where $\Delta m/m$ is the relative mass change ($\Delta m/m \gg \Delta k/k$). Coating the resonator with a material possessing high affinity for the target analyte facilitates mass loading based on a chemical reaction or physical sorption, resulting in a frequency downshift [17]. Sensor frequency can be tracked by interfacing the resonator with electronics to form an oscillation loop. The resulting output signal with frequency f_0 can be measured in real time and correlated to the sensor response.

Reducing the necessary circuit drive levels to lock into oscillations requires a resonator with low motional resistance [18], while frequency stability depends on quality factor Q , which quantifies “sharpness” of the resonance peak. Electrically, Q relates f_0 to the resonator bandwidth (smaller bandwidth indicates higher Q). Mechanically, Q is defined by energy stored versus energy lost per cycle, or (5)

$$Q = 2\pi \frac{\text{energy stored}}{\text{energy dissipated per cycle}} . \quad (5)$$

Because signal amplification naturally occurs by a factor of Q at resonance, small amplitudes can be increased without requiring significant power consumption from amplifying electronics. Furthermore, mechanical resonators achieve Q s in the thousands and even millions [19] compared to electrical LC resonant circuits exhibiting Q s in the tens [20]. In sensor applications, high- Q operation is essential because any broadening of the oscillator frequency spectrum translates to phase-noise (jitter in time domain), which ultimately leads to uncertainty in sensor readout.

2.2 RESONATOR TRANSDUCTION METHODS

This section discusses three common integrated transduction methods for resonators and why piezoelectric actuation is the most promising candidate for gravimetric micro-sensing.

2.2.1 CAPACITIVE AND THERMAL ACTUATION

Capacitive resonators (Figure 2.1a) are excited into resonance when an AC signal is applied to conductive electrodes separated by a capacitive gap, creating a fluctuating electrostatic force [21]. Capacitively-actuated devices typically have very high Q values [22] because the transducers are physically separated from the resonating body, reducing energy loss via actuation and sensing mechanisms [21]. As a result, such devices typically require a large DC polarization voltage (V_p) for operation and also have higher motional resistance, which creates difficulties for electronics interfacing.

Alternatively, resonators can be thermally actuated (Figure 2.1b) by passing a combination of DC and AC current through a structure containing regions of varying electrical resistance. Fluctuating temperature gradients (and therefore, fluctuating thermal expansion) generates sufficient force to excite various extensional resonance modes and has been demonstrated at frequencies as high as 61 MHz [23]. However, the AC and DC components required for thermal actuation also leads to high power consumption; additionally, sensor designs must be thoroughly optimized to prevent adverse effects on the sensitive coating—especially if it is polymer-based—due to high localized temperatures.

2.2.2 PIEZOELECTRIC TRANSDUCTION

While capacitive and thermal actuation enable high-performance resonators via CMOS-compatible processes, both transduction methods present challenges for integrated microsensors. Piezoelectric transduction, utilized in numerous macro-scale applications, has also been employed in micromachined resonators and sensors.

The piezoelectric effect is the conversion of mechanical strain to electric charge that occurs in materials that lack a center of symmetry. Piezoelectric materials also exhibit the inverse piezoelectric effect, in which mechanical deformation results from the application of electric charge. Since its discovery in the late 1800s, the bi-directional behavior of piezoelectricity has been exploited for various sensors and actuators, resonant devices in particular. Piezoelectrically-driven resonators (Figure 2.1c) have several advantages including low motional impedance [26] and the ability to operate without DC voltages. These characteristics make piezo devices desirable for interfacing with electronics and low-power operation compared to capacitively- or thermally-actuated resonators.

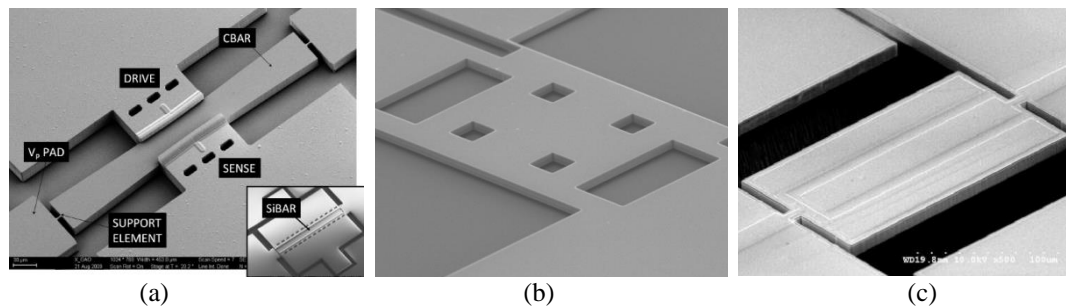


Figure 2.1: Silicon resonators utilizing (a) capacitive [22], (b) thermal [24], and (c) piezoelectric actuation [25].

2.3 PIEZOELECTRIC ACOUSTIC WAVE MICRO-DEVICES

2.3.1 PIEZOELECTRIC MATERIALS

Quartz, a strong crystalline piezoelectric material, has been successfully manufactured for high-precision frequency references, film thickness monitors, and chemical sensors in the past few decades [17, 27-29]. However, the bulk mode frequency of quartz resonators is inversely related to film thickness, which pre-determines the operation frequency for an entire quartz substrate. Various challenges associated with quartz and CMOS integration ignited research and development of micromachined alternatives for timing and sensing, as well as suitable piezoelectric material synthesis methods for such micro-devices. Piezoelectric polymers such as PVDF [30] and polycrystalline thin films including lead zirconate titanate (PZT), zinc oxide (ZnO), and aluminum nitride (AlN) can be realized through sputtering, sol-gel deposition [31], and more recently, inkjet printing [32].

2.3.2 PIEZOELECTRIC MICRO-RESONATORS

Advancements in thin film deposition and fabrication techniques contributed to recent development in piezoelectrically-actuated acoustic wave devices, including thin film bulk acoustic resonators (FBARs) [33], surface acoustic wave (SAW) resonators, and flexural micro-cantilevers.

FBARs comprise a piezoelectric thin film material stack supported over an air cavity or, in solidly-mounted resonator (SMR) configuration, reflecting layers to provide acoustic isolation from the substrate. Devices typically resonate in a thickness-extensional mode but can be designed to excite a thickness-shear mode, as in quartz (Figure 2.2a). FBARs can be batch-fabricated with hundreds to thousands of devices on a

single substrate, achieving high Q and mass sensitivity for various applications into the GHz regime [34]. However, resonant sensors with thickness-dependent frequency are prone to Q degradation since functional coatings are applied in the direct path of the acoustic wave.

SAW resonators exploit a mode with maximum wave propagation in the surface of a piezoelectric material [1] (Figure 2.2b). SAW resonators have been used in various signal processing applications, but the high sensitivity to surface perturbations has also made them attractive for sensing. Because SAW devices are based on mono-crystalline piezoelectric materials such as lithium tantalate (LiTaO_3), lithium niobate (LiNbO_3), or quartz [35], they are incompatible with standard CMOS electronics. Furthermore, devices are not easily miniaturized and typically have dimensions in the mm-range [36].

While in-plane resonance modes have been used to implement cantilever-based chemical sensors [37], micro-cantilevers are typically excited in a flexural, out-of-plane mode (Figure 2.2c). Cantilever resonators often require lasers or external equipment to measure deflection, which further complicates miniaturization and integration.

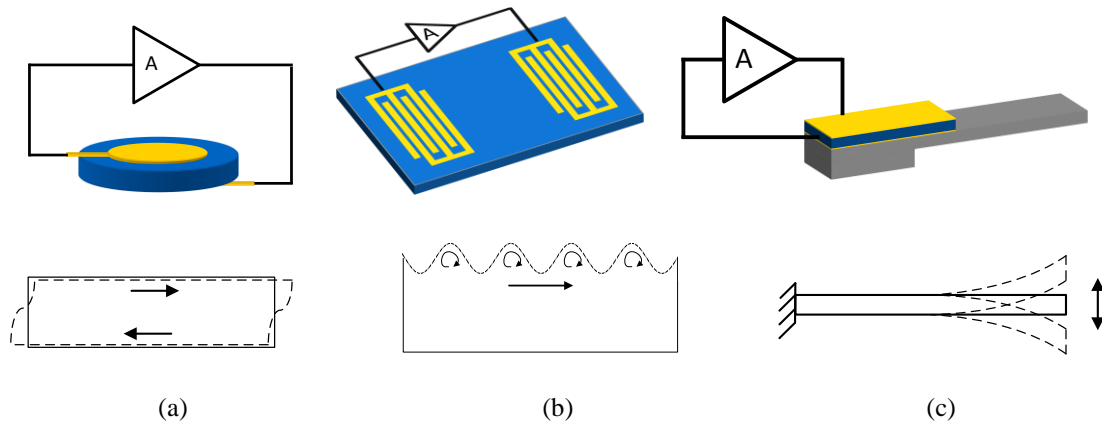


Figure 2.2: Piezoelectric resonant sensors based on (a) bulk/thickness shear (quartz and FBAR with piezoelectric material sandwiched between metal electrodes), (b) surface (SAW device with interdigitated electrodes on a piezoelectric substrate), and (c) flexural (cantilevers with piezoelectric stack deposited on a structural material).

2.4 SENSOR IMPLEMENTATION CHALLENGES

As demonstrated by piezoelectric acoustic wave micro-devices, resonators can be rendered sensitive to physical and chemical quantities via functional coatings, showing that gravimetric resonant detection is a promising alternative to traditional techniques for miniaturized sensors. However, portable, multi-sensing systems require flexibility to accommodate for diverse materials used in sensor functionalization while maintaining low power and low cost.

3 THIN-FILM PIEZOELECTRIC-ON-SILICON MICRO- PLATFORM

Electrostatically-transduced (capacitive) resonators, which typically require vacuum encapsulation to achieve high Q , are not suitable for sensing applications that require exposure to the environment. Furthermore, their high motional resistance and the need for a DC polarization voltage complicate oscillator interfacing and increase system power consumption. Thermally-actuated resonators, which also require DC voltages to operate, are power-hungry and susceptible to reduced analyte sensitivity as a result of sorption layer heating [38]. In contrast, low-power sensing is achievable using thin-film piezoelectric-on-substrate (TPoS) technology [25], which combines efficient piezoelectric transduction requiring no DC voltages with a high- Q structural material such as nanocrystalline diamond or silicon [26, 39]. Single-crystal silicon, which has emerged as a viable alternative to quartz for timing and sensing as a result of its excellent mechanical and acoustic properties, is chosen as the substrate in this work to enable cost-effective fabrication and compatibility with CMOS electronics.

An integrated micro-platform consisting of TPoS gravimetric gas sensors and kinetic energy harvesters is proposed for micro-sensing system implementation (Figure 3.1).

3.1 PLATFORM OVERVIEW

The TPoS gravimetric sensor array can be selectively functionalized to detect key chemical and biological markers in the environment. The maturity of silicon micromachining technology enables a material with desirable electrical and mechanical properties to be exploited for multi-functional integrated systems. Unlike quartz, silicon

resonators are not natively piezoelectric and suffer from large temperature-induced frequency shifts via modulation of elastic properties, while the combined effects of temperature and humidity influence chemical reactions and sorption in sensitive layers. Since sensitivity is directly tied to f_0 , modes with lithographically-definable frequencies enable array implementation on a single wafer to accommodate multiple levels of sensitivity.

Besides mobile and consumer applications, the TPoS platform can also be applied to self-powered wireless data transmission for autonomous sensor networks [40]. Sensors in remote or dangerous locations may need to operate for several years without interruption and require alternatives to battery replacement or recharging that do not increase overall system size. Thus, it would be beneficial to directly integrate kinetic energy harvesting devices with the proposed platform.

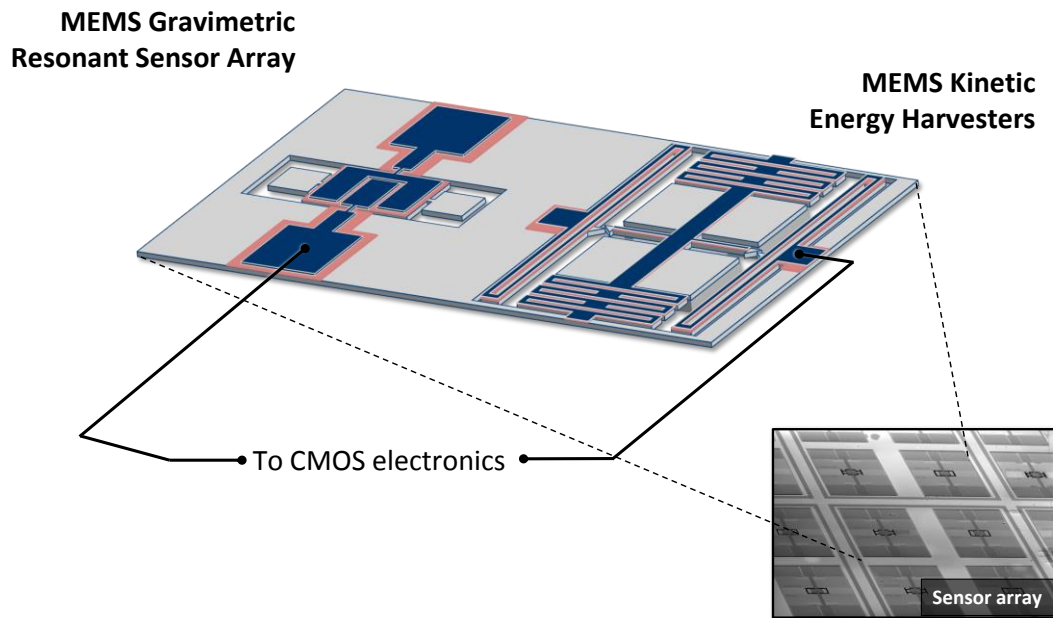


Figure 3.1: Schematic diagram of integrated micro-platform consisting of TPoS gravimetric resonant sensors and kinetic energy harvesting (KEH) devices.

3.2 FABRICATION PROCESS FLOW

The TPoS fabrication process flow [41] was customized to facilitate integration of sensors and energy harvesting devices on a single substrate. All steps except AlN deposition were performed in the Georgia Tech Pettit and Marcus cleanroom facilities.

3.2.1 CHOICE OF PIEZOELECTRIC MATERIAL

Sol-gel deposited films such as PZT require poling, which subjects the film to a strong electric field for an extended period of time, to obtain the required piezoelectric crystal structure. On the other hand, piezoelectric zinc oxide (ZnO) and aluminum nitride (AlN) can be deposited by low-temperature RF magnetron sputtering, which may be necessary for various sensor functionalization processes. Piezoelectrically-transduced sensors based on both ZnO and AlN have been investigated in this work, and advantages and challenges of sensor integration are briefly discussed.

ZnO, which exhibits high electromechanical coupling, is readily available in the Georgia Tech cleanroom and has been optimized to produce RF-sputtered films with high *c*-axis orientation, confirmed by x-ray diffraction (XRD) analysis on actual process wafers. E-beam evaporated gold, which has been previously established as a suitable electrode material for ZnO [25], serves as a useful bio-functionalization layer for self-assembly processes and is also immune to oxidation from exposure to ambient air. However, a major drawback of ZnO is its high reactivity to common wet and dry etchants such as HF, which imposes restrictions on post-deposition fabrication steps. Over time, the reactivity of ZnO in the environment could result in degraded resonator performance. Furthermore, the risk of CMOS contamination by Zn ions eliminates the possibility of monolithic integration and introduces packaging complications in 3D stacked CMOS and

MEMS systems. Finally, without strict stoichiometric control of the deposited film, ZnO can be fairly susceptible to DC leakage and requires additional isolation layers that may also negatively impact sensor performance [37].

AlN, which possesses an identical crystal structure (wurtzite) and similar transverse piezoelectric coefficient to ZnO, is CMOS-compatible and less susceptible to DC leakage than ZnO [42]. Since AlN exhibits lower reactivity to many common wet and dry etchants, AlN-on-Si devices provide additional flexibility for array implementation and post-fabrication sensor functionalization.

3.2.2 ZNO-ON-SI FABRICATION PROCESS FLOW

ZnO-on-Si resonators were fabricated on 5- μm thick, high-resistivity silicon-on-insulator (SOI) wafers (Figure 3.2a-f). First, 0.05 - 0.1 μm of gold is electron-beam evaporated and patterned by liftoff, removing Shipley SC1827 positive photoresist with acetone to form the bottom electrode (Figure 3.2a). To improve adhesion to the Si device layer as well as the piezoelectric film, a thin layer of e-beam evaporated titanium sandwiches the gold layer.

Approximately 0.7 μm ZnO is deposited by RF sputtering with 125 W RF power and substrate temperature of 210 °C for 100 minutes. Parameters consistently used in each ZnO deposition are listed in Table 3.1. After each deposition, *c*-axis orientation required for piezoelectric coupling is confirmed through XRD analysis. Rocking curve analysis (ω scan) revealed typical full-width-half-maximum (FWHM) values of about 2.2°, indicating a narrow distribution around the surface normal and good crystalline quality (Figure 3.3).

The ZnO film is subsequently patterned in acetic acid:deionized water (1 mL:150 mL ratio achieves optimal pH of 3) to remove ZnO from all areas of the wafer except the active resonator body (Figure 3.2b). 0.1 μm of gold is evaporated and patterned by liftoff to create the top electrode and complete the piezoelectric stack (Figure 3.2c). To define resonator supports and the overall shape by forming trenches in the silicon device layer, deep reactive ion etching (DRIE) is performed in an STS ICP system (Figure 3.2d). The device is released by etching the handle layer from the backside with SF_6 (Bosch process, STS ICP) and subsequently removing the buried oxide (BOX) layer from the backside with a C_4F_8 mixture using a Plasma-Therm ICP etcher (Figure 3.2e). More details on sensor functionalization, which is performed after device release (Figure 3.2f), are provided in chapter 4.

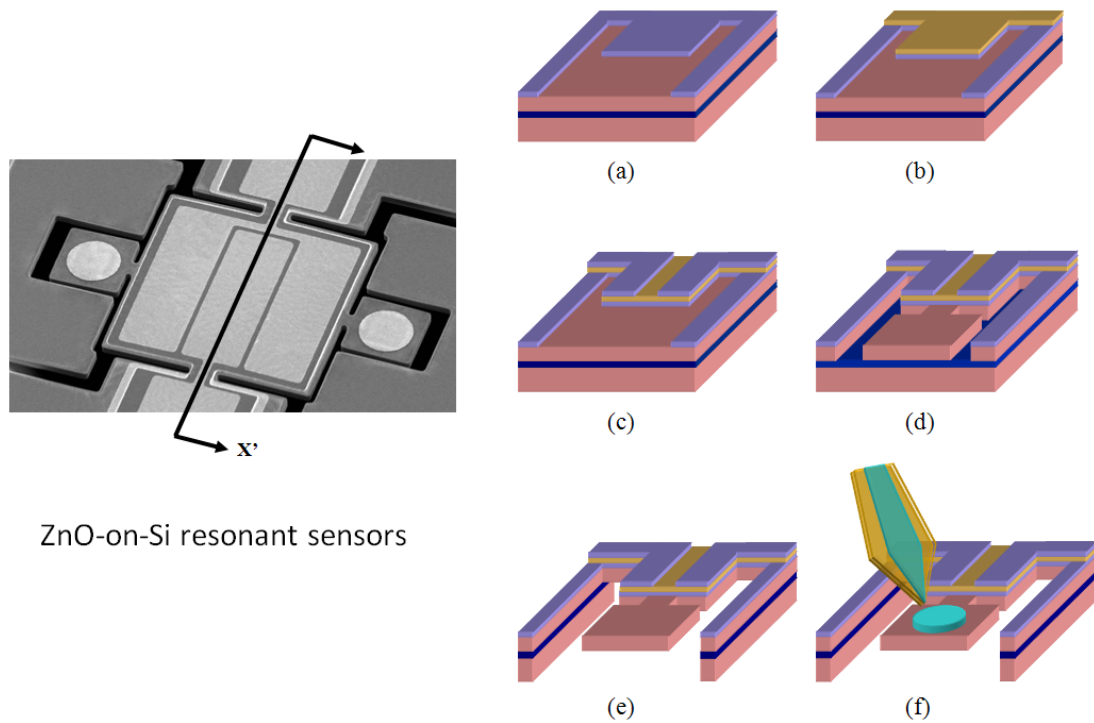


Figure 3.2: Scanning electron microscope (SEM) image of released ZnO-on-Si resonator and accompanying process flow.

Table 3.1: Parameters used for ZnO RF sputter deposition in the Georgia Tech IEN cleanroom.

Initial pumpdown pressure	Process pressure	RF power	Ar/O ₂ flow ratio	Substrate temperature	Target-to-sample distance
4 to 6 μ Torr	6 mTorr	125 W	1:1	210°C	9.5 cm

Process assumes ZnO target used in argon (Ar) and oxygen (O₂) ambient.

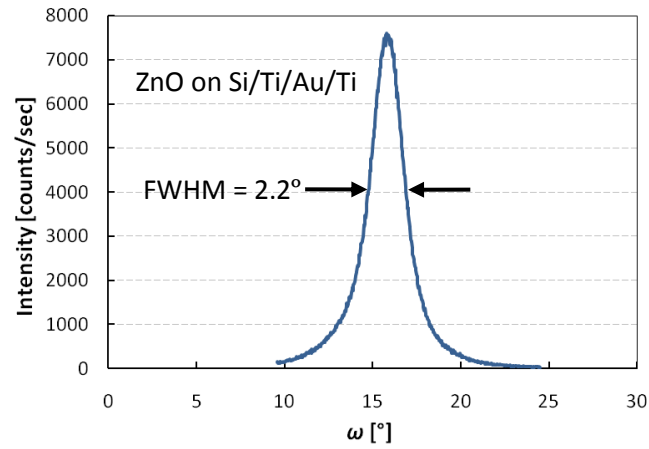


Figure 3.3: Typical XRD rocking curve (ω) scan to confirm *c*-axis orientation of ZnO sputtered in the Georgia Tech Pettit cleanroom facility.

3.2.3 ALN-ON-SI FABRICATION PROCESS FLOW

This section outlines the basic AlN-on-Si process flow for resonators and sensors, fabricated on silicon device layers ranging from 5 to 20 μm . Modifications to facilitate energy harvester integration are described in section 6.4.

Molybdenum electrodes sandwiching a 0.7 – 1 μm thick RF-sputtered AlN layer are deposited on blank SOI wafers by the OEM Group, Inc. and shipped to Georgia Tech for remaining process steps. Typical FWHM of the deposited AlN films, as measured by OEM, ranges from 1.63 to 2°. Because piezoelectric stack layers are successively deposited, fabrication begins with patterning the top Mo electrodes in SF_6 plasma using a Shipley SC1813 photoresist mask (Figure 3.4a). Next, PECVD oxide is deposited on both sides of the wafer (~300 nm topside, ~5 μm backside). The topside thin oxide is protected with photoresist while the backside oxide is BOE-etched to define device release cavities. The top oxide is patterned with an SC1827 photoresist mask, and AlN is subsequently etched in TMAH heated at 40°C to expose ground pads in the bottom Mo layer (Figure 3.4b). Additional oxide is deposited on the wafer topside and patterned with SC1827; a Plasma-Therm ICP tool is used to etch oxide followed by AlN and bottom Mo. The device layer Si is etched in an STS ICP (low-frequency Bosch recipe) to define the resonator geometry (Figure 3.4c). Finally, resonators are released from the wafer backside using a high-frequency Bosch etching recipe (STS ICP) to remove the handle Si and buried oxide layers (Figure 3.4d). As with the ZnO-on-Si resonant sensors, released devices are functionalized using the Bioforce Nano eNabler (discussed in chapter 4, section 4.3.2).

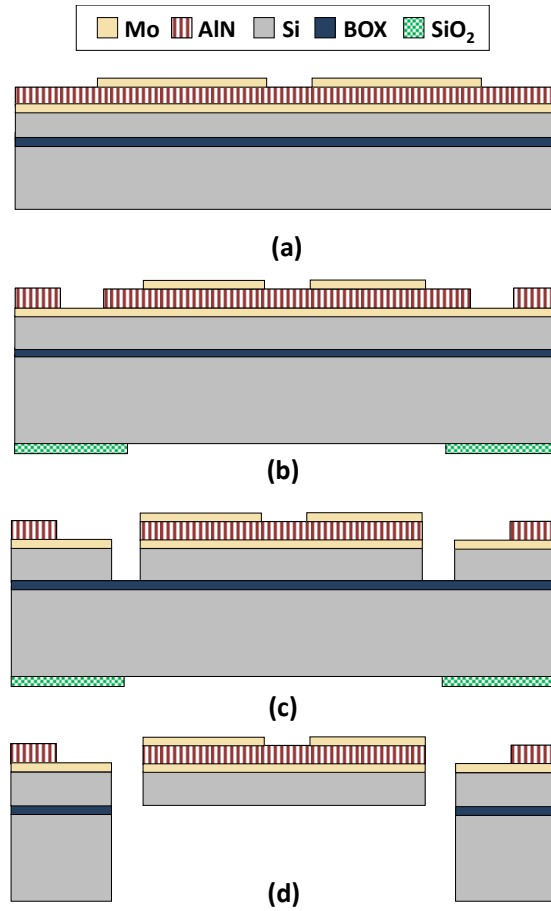


Figure 3.4: Fabrication process flow for AlN-on-Si resonant sensors: (a) top Mo patterning; (b) backside oxide mask patterning and AlN etch to expose bottom Mo; (c) device Si trench definition; and (d) handle Si and BOX layer removal.

3.3 MATERIALS FOR SORPTION-BASED MICRO-SENSING

TPoS resonators function as thermometers based on the intrinsic temperature coefficient of frequency (TCF) of silicon. Sensitizing resonators to a particular gas-phase analyte requires a functional coating that facilitates sorption or a chemical reaction, resulting in mass loading that can be detected by frequency shift. Gravimetric micro-resonators have employed a variety of materials for gas sensing; however, application-dependent factors such as reversibility, repeatability, and response time of analyte reaction should be considered in material selection.

3.3.1 POROUS MATERIALS AND FRAMEWORKS

Adsorbate materials such as carbon and zeolites have been used for years by environmental scientists to remove harmful pollutants from the air. Naturally-porous zeolites, or “molecular sieves,” contain an alumino-silicate crystal structure with uniform nanometer-sized pores determined by silicon-to-aluminum ratio [43]. The Si/Al ratio, which controls the hydrophobicity, defines the analytes to which a particular zeolite structure will have the greatest affinity (non-polar to hydrophobic, polar to hydrophilic). The tunable characteristics of zeolites have been exploited for selective VOC and gas detection using quartz crystal microbalances (QCMs) [44, 45], micro-cantilevers [46], and semiconductor gas sensors [47, 48]. Zeolite-modified sensors exhibited enhanced responses, most likely as a result of increased surface area on which molecules can adsorb. Since zeolites are grown by high-temperature hydrothermal processes, most sensors were functionalized spin-coating, dropping, or evaporating a suspension of crystals [46]. However, uniformity of the final deposited films typically varies significantly from one sensor to the next, which is unacceptable for batch-processing.

Metal-organic frameworks (MOFs) are nano-porous materials with crystalline structure defined by rigid organic molecules linked to metal ion clusters. Various micro-sensors modified with MOFs [49-51] have been used to detect humidity and various gases. However, like zeolites, the MOF functionalization process requires immersion or deposition of a suspension, which creates challenges in achieving uniformity control.

Alumina- and silicon-based porous films have also been utilized for humidity sensing [52, 53]. However, the sensor fabrication process exposes the device to large current density, harsh chemicals, and temperatures in hundreds of degrees Celsius, which is not compatible with CMOS integration and ultimately degrades sensor performance.

Overall, porous materials and frameworks exhibit enhanced analyte adsorption and selectivity while remaining chemically and thermally stable. However, slow diffusion through these materials results in extremely long sensor response times, with certain sensors failing to equilibrate after several hours of constant exposure [49]. Even if the sensor responds rapidly [46], full recovery (complete analyte desorption) requires the material to be heated, consuming excess power that cannot be afforded in miniaturized sensing systems.

3.3.2 POLYMERIC MATERIALS

Polymers are advantageous for real-time sensor array applications where faster response time is required. Adsorption-based reactions are completely reversible and unlike hard, porous materials, do not require thermal desorption to “reset” the sensor. From an integration standpoint, polymeric materials have been applied to sorption-based gravimetric sensing [17, 54-56] because uniform thin films are easily achieved by spin-coating, a repeatable batch-fabrication process. Furthermore, recent studies have shown

that sorptive polymers can be tailored for sensitivity and selectivity by adding functional groups and modifying other properties in synthesis [57].

Polymers are not without drawbacks, however, as they are inappropriate for high-temperature environments and have limited lifetime compared to hard materials because of their lower stability. However, polymeric materials are still strong candidates for sensing in consumer applications and even industrial applications where temperature is not a concern.

Although versatile options to modify the sensitivity of micromachined silicon resonators for VOC and gas detection are available, polymers for sorption-based sensing have been characterized in this dissertation. Details of gravimetric sensor functionalization are provided in chapter 4.

4 TPOS GRAVIMETRIC RESONANT SENSORS

This chapter introduces piezoelectric-on-silicon resonant sensors with annexed platforms. Design principles and tradeoffs between mass sensitivity and resonator performance are discussed.

Section 4.2 presents micromachined temperature and relative humidity (RH) sensors using ZnO-on-silicon, lateral-mode bulk acoustic wave (BAW) resonators. An uncoated reference resonator is utilized in conjunction with an identical, humidity-functionalized resonator to yield a thermally-compensated RH sensor. The reference sensor exploits the dual-mode response of first and third-order in-plane extensional modes to eliminate RH sensor dependence on temperature. Polyethyleneimine (PEI) is deposited on annexed platforms of the BAW resonator, enabling operation from 20 to 92 %RH with high Q in air. A sensitivity of 1.2 kHz/%RH from 20 to 60 %RH and 14 kHz/%RH from 60 to 92 %RH is measured at room temperature. The RH sensor combined with the reference sensor occupies a total area of .053 mm².

The final section in this chapter presents aluminum nitride (AlN) thin-film piezoelectric-on-silicon (TPoS) resonators optimized for gravimetric gas sensing. Sensors with polyisobutylene (PIB)-functionalized annexed platforms exhibit a linear sensitivity of -0.09 Hz/ppm to toluene and -0.18 Hz/ppm to xylene. The annexed platform design enables the sensor to maintain a high Q of 3700 in air and low motional resistance of 1.1 k Ω during operation, which ensures low-power oscillator interfacing and readout. AlN-on-Si resonators with annexed platforms are suitable for array implementation in environmental sensing micro-systems that measure temperature, humidity, and various gases of importance to health and safety.

4.1 TPOS RESONATOR WITH ANNEXED PLATFORMS

Ideally, gravimetric sensor frequency should only be affected by changes in mass based on sorption in the functional material. In reality, various factors dependent on sensor structure and materials can contribute to undesired frequency error (e.g. Q , temperature, stiffness changes, etc.). Therefore, both enhancements in mass sensitivity and device performance should be considered when designing resonant sensors.

Sensors consist of a centrally-clamped bulk acoustic wave (BAW) resonator, which exhibits an in-plane length-extensional (LE) resonance mode at frequency f_0 defined by length L (6)

$$f_0 \propto \frac{1}{2L} \sqrt{\frac{E}{\rho}}, \quad (6)$$

with Young's modulus E of the structural material and density ρ . Sensing material is deposited on platforms connected to the central structure by support beams (Figure 4.1). In the simplest case, W and L_p are assigned equal values such that the sensor resembles a rectangular block; however, W can be increased to fine-tune sensor frequency and reduce motional resistance.

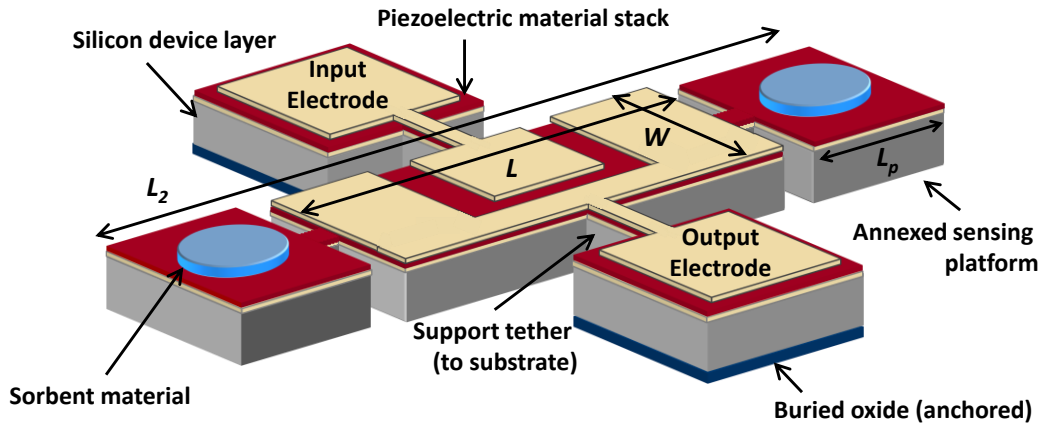


Figure 4.1: Diagram of AlN-on-Si resonant sensor with annexed platforms.

In the sensor mode of operation, platform motion is in phase with the central block extension (Figure 4.2a). In a typical LE resonator (Figure 4.2b), strain varies along L and leads to undesired equivalent stiffness changes due to analyte sorption [58]. In contrast, maximum strain occurs in the central block and beams of the modified sensor (Figure 4.2b). The uniform strain distribution in the platforms enables a predominantly translational motion, minimizing effects on Δk and ensuring that adsorption anywhere on the platforms (except near the beams) yields predictable influences on equivalent mass. Thus, mass loading on the platforms (at the maximum vibration amplitude) contributes most significantly to resonance frequency shift. Besides decoupling modal mass and stiffness effects on frequency, the beams confine longitudinal wave propagation to the central structure where signal actuation and detection occur. Thus, damping introduced by analyte sorption on sensing areas does not interfere with resonator acoustic operation. As a result, the sensor maintains high Q in air, which ultimately impacts frequency stability and minimum limit of detection [38].

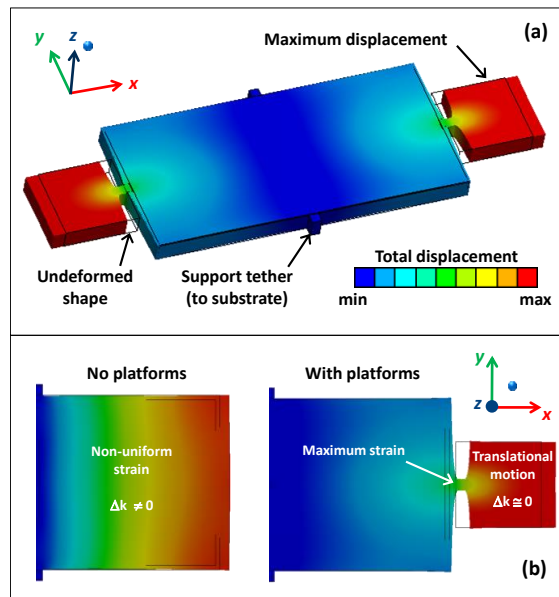


Figure 4.2: (a) ANSYS mode shape of gravimetric sensor with annexed platforms; (b) comparison of relative modal displacement between conventional LE sensor and sensor with platforms.

4.2 ZNO-ON-SI RESONANT TEMPERATURE AND HUMIDITY SENSOR

4.2.1 TEMPERATURE AND HUMIDITY EFFECTS ON RESONANCE FREQUENCY

Frequency variations caused by the negative TCF of silicon have impeded progress in commercializing such devices. In timing-based applications, temperature-induced frequency variations are passively compensated through oxide deposition [59], p-n doping [60], or by engineering the device geometry [61]. With sensing applications, the focus shifts from eliminating resonator TCF to measuring the temperature and properly accounting for thermal effects on different target analytes in the sensor readout.

While temperature is a key contributor to undesired frequency change in silicon resonant sensors, moisture in the surrounding environment can also affect the sensor output. It is useful to consider relative humidity (RH)—the ratio of actual water vapor pressure (p_{H_2O}) to the saturation vapor pressure ($p^*_{H_2O}$)—in most applications [62]. The dependence of p_{H_2O} and $p^*_{H_2O}$ on temperature creates difficulty in accurately measuring RH without an accompanying temperature reading.

To separate temperature effects from the desired sensor response, external thermometers are often used to obtain the local temperature, which leads to inaccuracy as a result of thermal gradients between the thermometer and sensor. Sensors with integrated temperature detectors, dual-resonator temperature measurement, and dual-oscillator systems have been developed to address this challenge [63-65]. However, even integrated thermometers increase the overall system size; additionally, measurement inaccuracies arise when temperature information is extracted from multiple devices, as in the dual-resonator and dual-oscillator system. Rather than consuming additional power or area to control the device temperature [66], the resonator itself can be used as a

thermometer to account for temperature-induced frequency changes through a technique known as self-temperature sensing, where the total frequency change of a resonant sensor is modeled by the sum of both temperature- and analyte-induced frequency changes with negligible contributions from other physical parameters [16].

4.2.2 RESONANT TEMPERATURE AND HUMIDITY SENSING

Two micromachined ZnO-on-silicon, length-extensional (LE) mode BAW resonators are used to implement a resonant temperature and humidity sensor. An uncoated resonator serves as a reference temperature sensor, while an identical resonator coated with moisture-sensitive material measures humidity.

Multi-mode excitation in piezoelectric resonators is often troublesome because spurious peaks can interfere with the main mode operation. However, dual-mode self-temperature sensing exploits this characteristic by utilizing the TCF of two modes in a single device to determine resonator temperature [16]. In this case, the first and third length extensional resonance modes (f_1 and f_3) are actuated and detected by an interdigitated electrode configuration (outlined on the device in Figure 4.3). Any temperature-induced frequency shift in the RH sensor is compensated by extracting local temperature from the reference sensor characteristic to determine the correct value of RH.

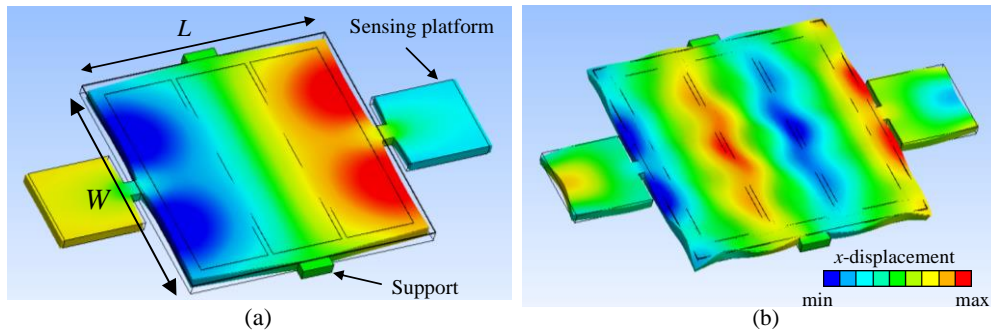


Figure 4.3: ANSYS mode shapes of ZnO-on-Si sensors at (a) f_1 and (b) f_3 ; $L = 120 \mu\text{m}$, $W = 120 \mu\text{m}$.

As shown in Figure 4.3, RH sensing mode f_1 exhibits maximum displacement at the block edges rather than in the platforms. In contrast to the extensional sensing mode described in section 4.1, platforms resonate out of phase with the central structure and are therefore expected to have less effect on mass sensitivity than the lower-frequency in-phase mode (with optimal mass sensitivity), which was not detected in this design.

4.2.3 FUNCTIONALIZATION PROCESS FOR HUMIDITY SENSING

Spray-coating [37], spin-coating, complete immersion [67], and inkjet deposition [68] have been used to functionalize sensor surfaces for various target molecules. The first three techniques are compatible with batch processing but require a mask or stencil to selectively pattern certain areas on a wafer. Although certain polymers have been defined by photolithography [57], water-soluble polymers would be dissolved in standard developer solutions and are therefore not suitable for lithographic patterning. Typical shadow mask feature size is too large unless the mask is placed in direct contact with the wafer, which can damage devices when removed after functionalization. Inkjet deposition does not require additional masks, but extensive characterization is required to achieve a uniform spot size with desired properties. Furthermore, because the nozzle is placed a

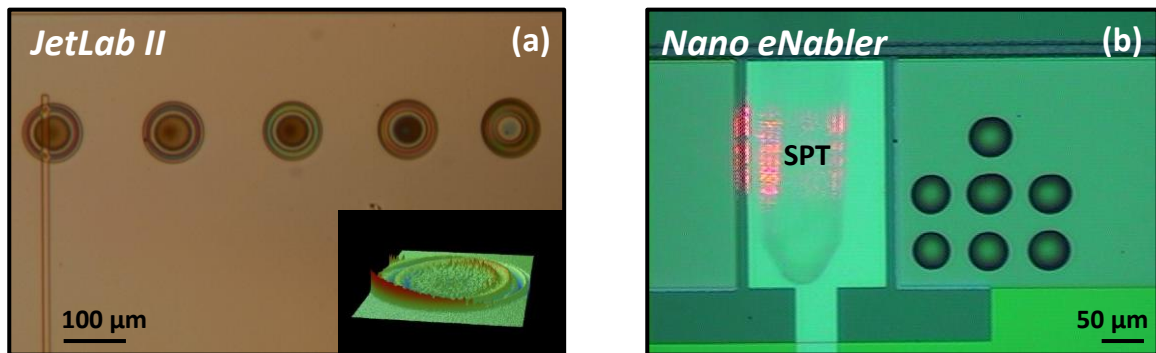


Figure 4.4: (a) Patterns deposited using a Jetlab II tool. Colored rings indicate thickness variations as confirmed by Wyko optical profilometer measurement (inset); (b) patterns deposited with the Bioforce Nano eNabler, showing minimal thickness variations.

considerable distance from the substrate, splashing introduces thickness variations in an un-optimized film (Figure 4.4a). Micro/nanofluidic cantilever arraying tools such as the Bioforce Nano eNabler™ provide an alternative method to selectively pattern nanoliter solutions on various substrates. Contrary to inkjet deposition, the cantilever tip makes direct contact when transferring solution to a substrate (Figure 4.4b). Parameters such as dwell time and contact force are adjustable, enabling precise control over deposited material properties. The Nano eNabler also has built-in capabilities for wafer-level array patterning that can be applied to large-scale sensor functionalization.

Polyethyleneimine (PEI) [69], a hygroscopic (water-attracting) polymer, was selected for humidity sensing based on its high affinity for polar molecules. PEI (50% w/v in H₂O, Sigma-Aldrich) is difficult to selectively pattern for two main reasons: (1) even after dilution to 1% concentration, the solution viscosity is high enough to break the 2- μ m thick nitride surface patterning tools (SPTs) or at least clog the narrow channels; and (2) such small amounts of solution quickly evaporate regardless of the deposition environmental conditions. Figure 4.5 depicts the unfortunate manifestation of both issues at once: clogged channels and evaporated solvent (water in this case) resulted in platforms becoming attached to the SPT by dried PEI. To overcome the first challenge,

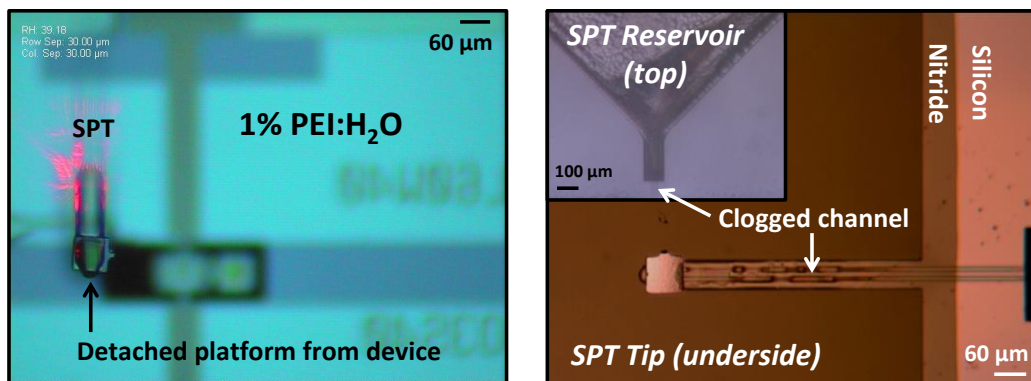


Figure 4.5: (left) Optical image of PEI-loaded SPT with stuck platform (H₂O evaporated mid-deposition); (right) close-up views of SPT reservoir (inset) with dried PEI and clogged channel.

SPT tips were “front-loaded” with solution rather than relying on capillary forces to move polymer from the SPT reservoir through the channel. Using a micro-centrifuge to mix a small amount of low-vapor-pressure alkaline buffer (Bioforce Nanosciences, Inc.) with PEI resulted in a significantly delayed solution evaporation time. Ultimately, ZnO-on-Si sensors were functionalized by loading a 1:10 mixture of PEI:buffer onto an SPT and depositing the solution onto each platform (Figure 4.6a).

4.2.4 SENSOR MEASUREMENT AND CHARACTERIZATION

Resonator frequency response was characterized using an Agilent E8364B Vector Network Analyzer. The reference sensor frequency $f_{1,ref}$ and third-order harmonic mode $f_{3,ref}$ (35 and 86 MHz, respectively) had a measured Q of 1,300 and 2,000 in air, and the RH sensor $f_{1,RH}$ had a Q of 1,340 in air after PEI patterning (Figure 4.6b).

Sensors were simultaneously characterized in a *Tenney BTRC* environmental chamber; to obtain the reference sensor characteristic for self-temperature sensing, the chamber temperature was varied from 25 to 85°C in 15°C intervals at constant RH values. To obtain the RH sensor behavior, RH values were ramped in 20 % intervals from 20 to 92 %RH at constant temperature values. Network analyzer measurements of each sensor f_1 and f_3 were recorded after one hour of stabilization.

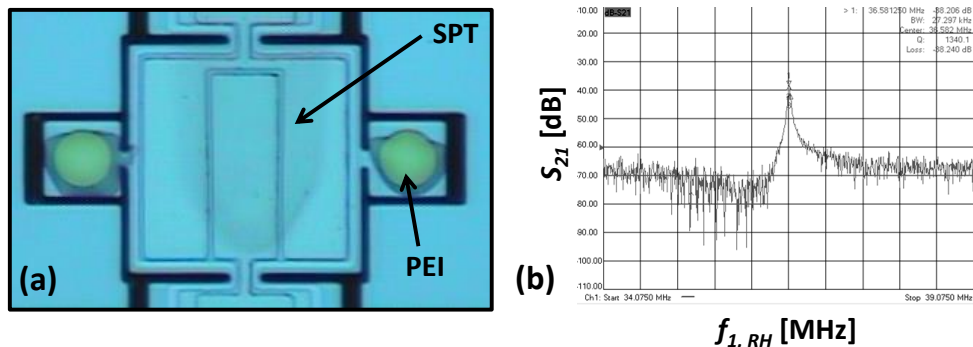


Figure 4.6: (a) Optical image of ZnO-on-Si humidity sensor functionalized with PEI; (b) frequency response of PEI-patterned RH sensor; $f_{1,RH} = 37$ MHz, $Q = 1340$ in air.

Equation (7) models the RH sensor total frequency change Δf_{RH} as a function of temperature T and RH . Because both temperature and RH sensors are structurally identical, they are assumed to have the same temperature response. Thus, the temperature-induced frequency change $\Delta f_{ref}(T)$ is used in place of $\Delta f_{RH}(T)$. $\Delta f_{ref}(T)$ and the total Δf_{RH} are experimentally measured to thermally compensate the RH response $\Delta f_{RH}(RH)$.

$$\Delta f_{RH} = \Delta f_{ref}(T) + \Delta f_{RH}(RH) \quad (7)$$

$\Delta f_{ref}(T)$ is characterized by a combination of f_1 and f_3 denoted as beat frequency $f_b = 3 \cdot f_1 - f_3$. Equation (8), extracted from the reference sensor response over temperature T ($^{\circ}\text{C}$) at constant RH (Figure 4.7), was used to determine TCf_b .

$$\Delta f_{b,ref}(T) = -8.8 \times 10^{-4} \cdot T + 19.35 [\text{MHz}] \quad (8)$$

TCf_b is greater than TCf_1 and linear, providing greater temperature accuracy and more

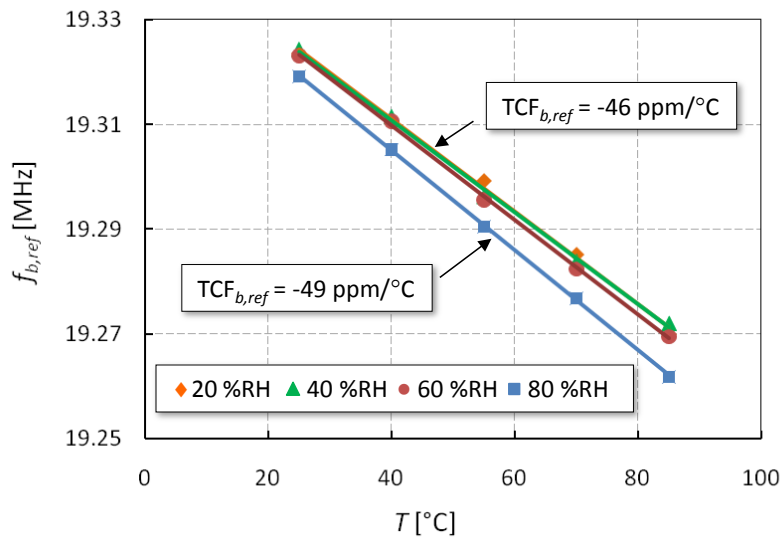


Figure 4.7: Temperature response of $f_{b,ref}$ at constant RH.

convenient future calibration. Moreover, $f_{b,ref}$ shows negligible sensitivity to humidity compared to $f_{b,RH}$, which was confirmed by sweeping RH at constant temperature values to determine the humidity sensitivity $S_{b,RH}$, or $\Delta f_b/\Delta RH$ (Figure 4.8).

The uncompensated RH sensor response exhibits distinguishable shifts with temperature (Figure 4.10). To obtain a compensated RH sensor response (Figure 4.9), the f_I vs. RH characteristics at various temperatures were plotted using thermally-corrected f_I values, confirming that the reference sensor minimizes temperature-induced changes in f_I . The average room temperature sensitivity is 1.2 kHz/%RH from 20 to 60 %RH and 14 kHz/%RH from 60 to 92 %RH. The sensor has a measured average hysteresis of 1.8 %RH at 55°C, which is the mid-point of the tested temperature range.

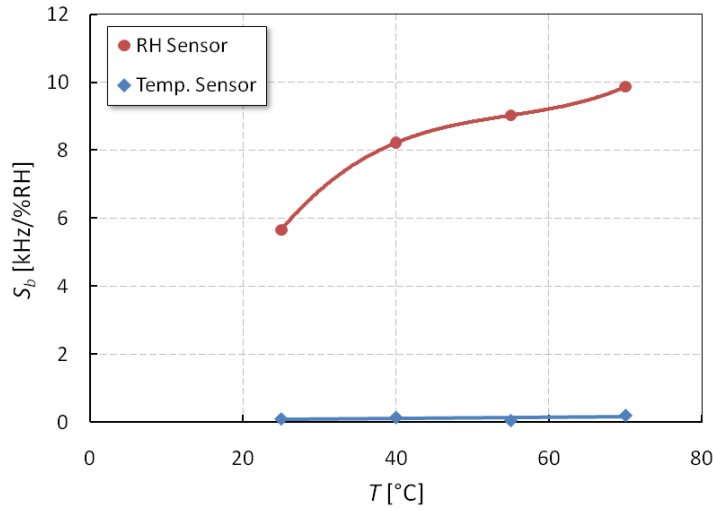


Figure 4.8: RH sensitivity of beat frequency $f_{b,ref}$ and $f_{b,RH}$ over temperature.

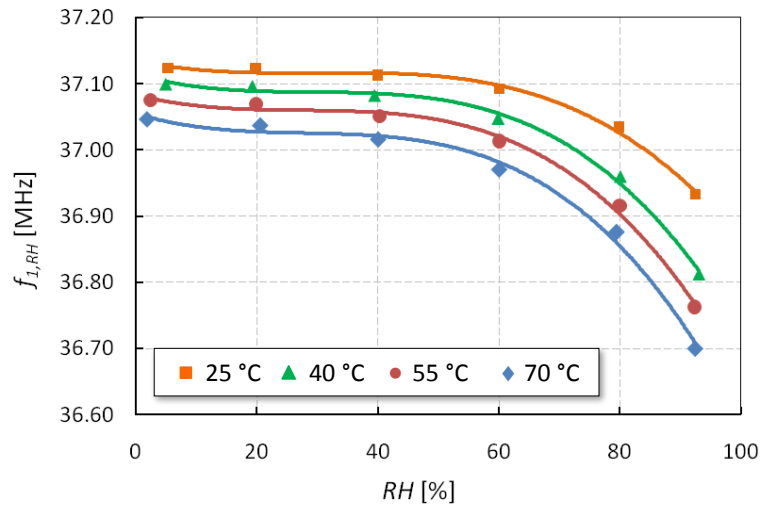


Figure 4.10: Sensor f_I response to RH prior to thermal compensation.

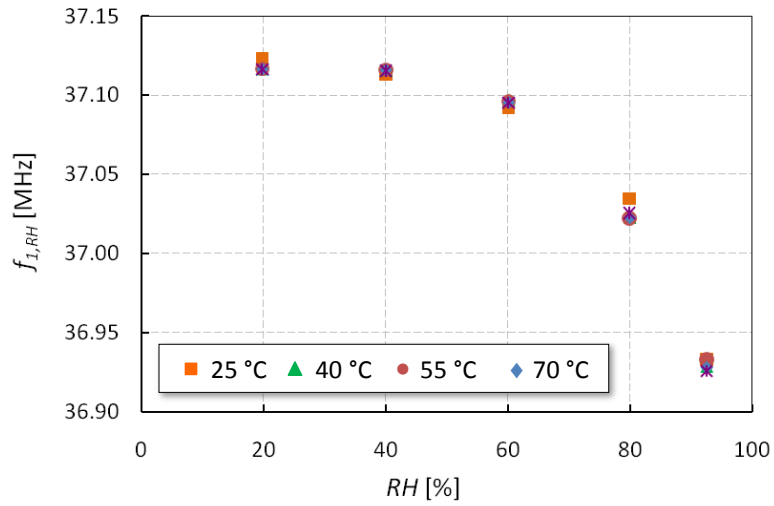


Figure 4.9: Sensor response after thermal compensation.

The RH sensor response to a rapid increase from 20 to 40 %RH was measured at 25°C (room temperature) (Figure 4.11). $f_{1,RH}$ tracks very closely with RH and has a response time of less than 25 seconds, which is limited by measurement setup and network analyzer sweep time.

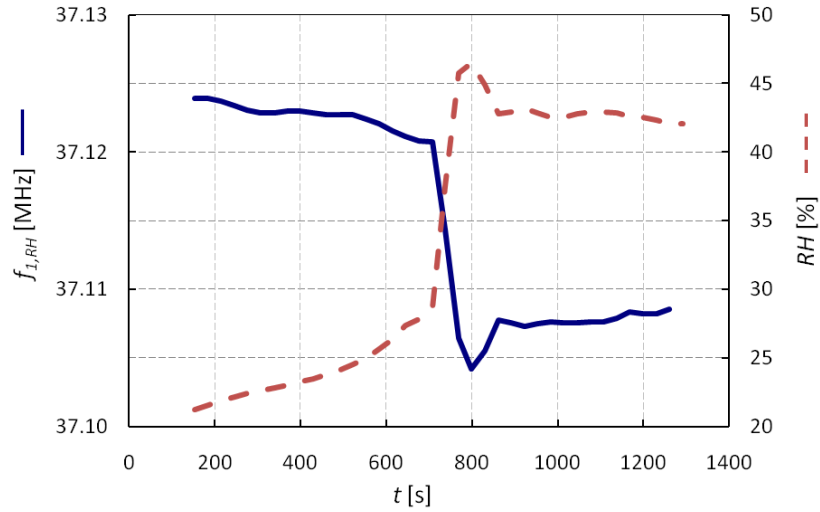


Figure 4.11: Sensor response to RH increase from 20 to 40 %RH at 25°C.

In this section, the highest Q humidity-sensing BAW micro-resonator was presented [70-72]. The selectively-patterned sensor was thermally compensated from 20 to 92 %RH by measuring the local temperature using an identical device that does not drastically increase the overall footprint. The PEI layer responded to humidity over the complete compensated range, but the RH sensor has an increased sensitivity of 14 kHz/%RH from 60 to 92 %RH. The RH sensor sensitivity at room temperature is on the same order of magnitude as previous works [65, 70, 72] but combined temperature and humidity sensors offer a size reduction compared to other micromachined resonant solutions without a temperature sensor [70]. While the RH&T sensors in this work were separate devices, dual-mode temperature sensing ultimately enables a single device to measure {Pierce, 1998 #218}

4.3 ALN-ON-SI RESONANT VOC SENSOR

Combustion-based sensors have often been used to detect VOCs that readily form explosive mixtures in air; however, they are mainly suitable for concentrations well above permissible exposure limits [73] and require additional power to heat a filament that oxidizes the gas mixture. On the other hand, piezoelectrically-transduced, silicon-based resonant sensors can be easily functionalized for various targets and combined with integrated electronics to create a low-cost, portable air quality detection system for temperature, humidity, VOC and gas sensing.

4.3.1 SENSOR DESIGN AND OPTIMIZATION

With $W = L$, the ZnO-on-Si RH sensor utilized an “out-of-phase” extensional mode, which provided lower mass sensitivity than the undetected in-phase mode. Longitudinal extension of the central block (whether $W > L$ or $L > W$) is essential to creating a prominent in-phase sensing mode. An AlN-on-Si resonant sensor with $L = 168 \mu\text{m}$ and $W = 80 \mu\text{m}$ exhibits significant enhancement of the sensing mode (Figure 4.12).

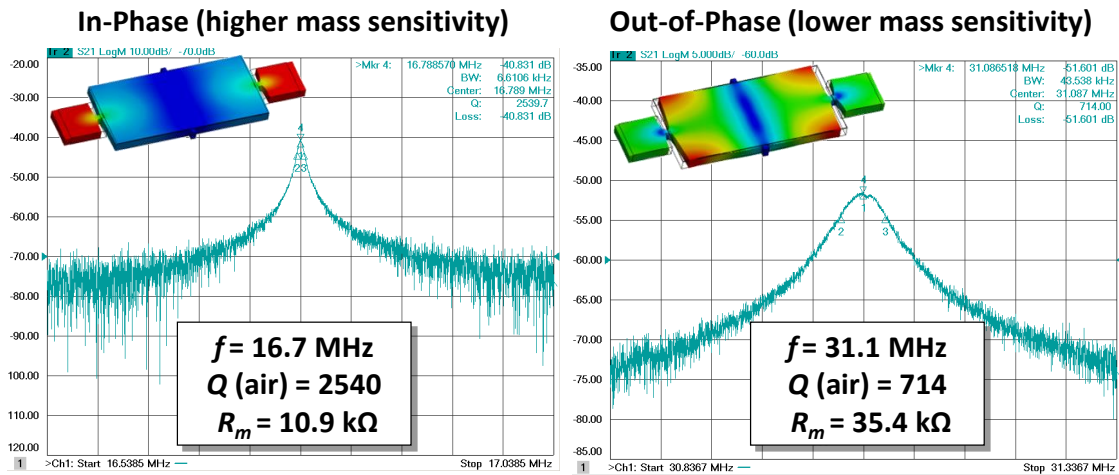


Figure 4.12: Frequency response measurements of 16-MHz sensor: (left) optimized sensing mode with platforms and central block in phase and (right) lower sensitivity mode with platforms out of phase with central block.

Mass sensitivity of the 16-MHz sensor was characterized by depositing platinum (Pt) via focused ion beam (FIB) on each platform and measuring the frequency after each deposition (Figure 4.13). The sensor maintained a Q of 2300 in air and exhibited a linear behavior that agrees well with simulated results. The varying purity of deposited Pt was attributed to discrepancies between calculated and actual mass [26].

In practical sensor implementation, the resonator is connected in feedback with a transimpedance amplifier (TIA) to generate oscillations at f_0 . The Barkhausen criterion for sustained oscillations indicates that resonator motional resistance R_m and electrical phase directly impact TIA design. Because piezoelectric resonators can excite several modes by a single electrode configuration, gain and phase conditions are often met for many frequencies. Therefore, both adequate compensation of resonator electrical loading [74] and spurious mode suppression are crucial in safeguarding the circuit from locking into oscillations at undesired frequencies.

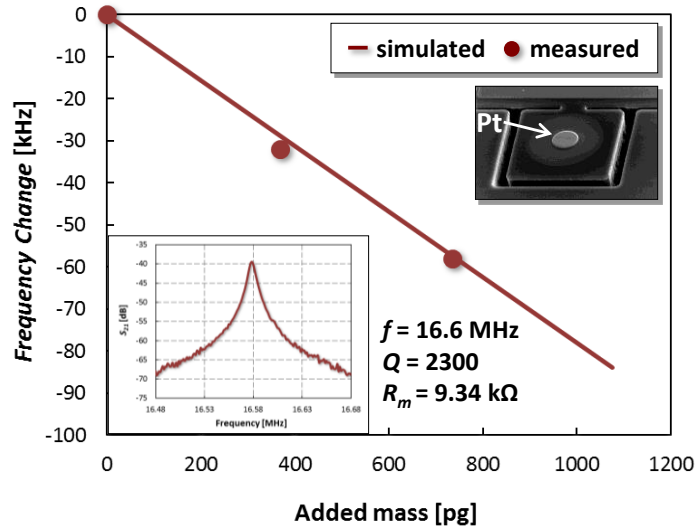


Figure 4.13: Simulated and measured mass sensitivity of 16-MHz sensor ($L = 168 \mu\text{m}$, $W = 80 \mu\text{m}$, $L_p = 40 \mu\text{m}$); measured data for 0 pg, 368 pg, and 737 pg of mass loading; (inset left) measured sensor frequency response; (inset right) close-up SEM image of FIB-deposited Pt on annexed platform.

Increasing W provides a larger electrode area to reduce R_m without significantly affecting resonance frequency. The resulting W/L ratio should be greater or less than 1 (but not equal) to preserve extensional behavior of the central block. A 19-MHz sensor with $2\times$ larger area ($L = 156 \mu\text{m}$, $W = 206 \mu\text{m}$, $L_p = 30 \mu\text{m}$), which is designed and simulated in ANSYS, shows that lower R_m is achievable without sacrificing PE mode mass sensitivity (Figure 4.14).

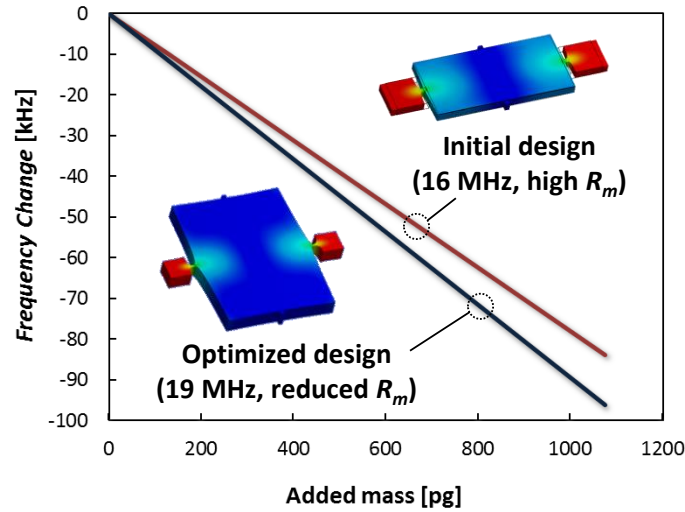


Figure 4.14: Simulated mass sensitivity of 19-MHz sensor ($L = 156 \mu\text{m}$, $W = 206 \mu\text{m}$, $L_p = 30 \mu\text{m}$) with reduced R_m compared to 16-MHz sensor.

The entire central resonant block undergoes expansion and contraction at f_0 , implying that electrical phase shift between input and output electrodes will be 0° regardless of placement on the piezoelectric layer. While interdigitated electrodes reduce the number of spurious modes for the 16-MHz sensor, three peaks with up to 10 dB lower IL than the sensor mode f_0 may complicate oscillator interfacing (Figure 4.15a). Thus, optimization goals for the 19-MHz sensor were to reduce R_m while suppressing undesired modes. Three potentially problematic modes at 29 MHz, 57 MHz, and 84 MHz were identified through ANSYS harmonic analysis. Based on the strain polarities shown in

Figure 4.15b, splitting electrodes symmetrically about the W axis creates 0° phase shift at f_0 and 180° phase shift for the three modes of concern. Therefore, even if a mode exhibits comparable IL to f_0 , circuitry designed for f_0 (0° phase) would not satisfy the phase condition to lock into oscillations at another frequency.

The measured R_m of a fabricated 19-MHz sensor was $1.14 \text{ k}\Omega$, corresponding to an IL value 10 dB lower than the majority of spurious modes up to 100 MHz (Figure 4.15b). While predicted problematic modes f_1 , f_2 , and f_3 had IL within 5 dB of f_0 , the designed 180° phase shift ensures the modes will not threaten oscillator interfacing. The remaining spurious peaks, which are located at higher frequencies, can be sufficiently attenuated by employing a simple low-pass filter within the feedback loop.

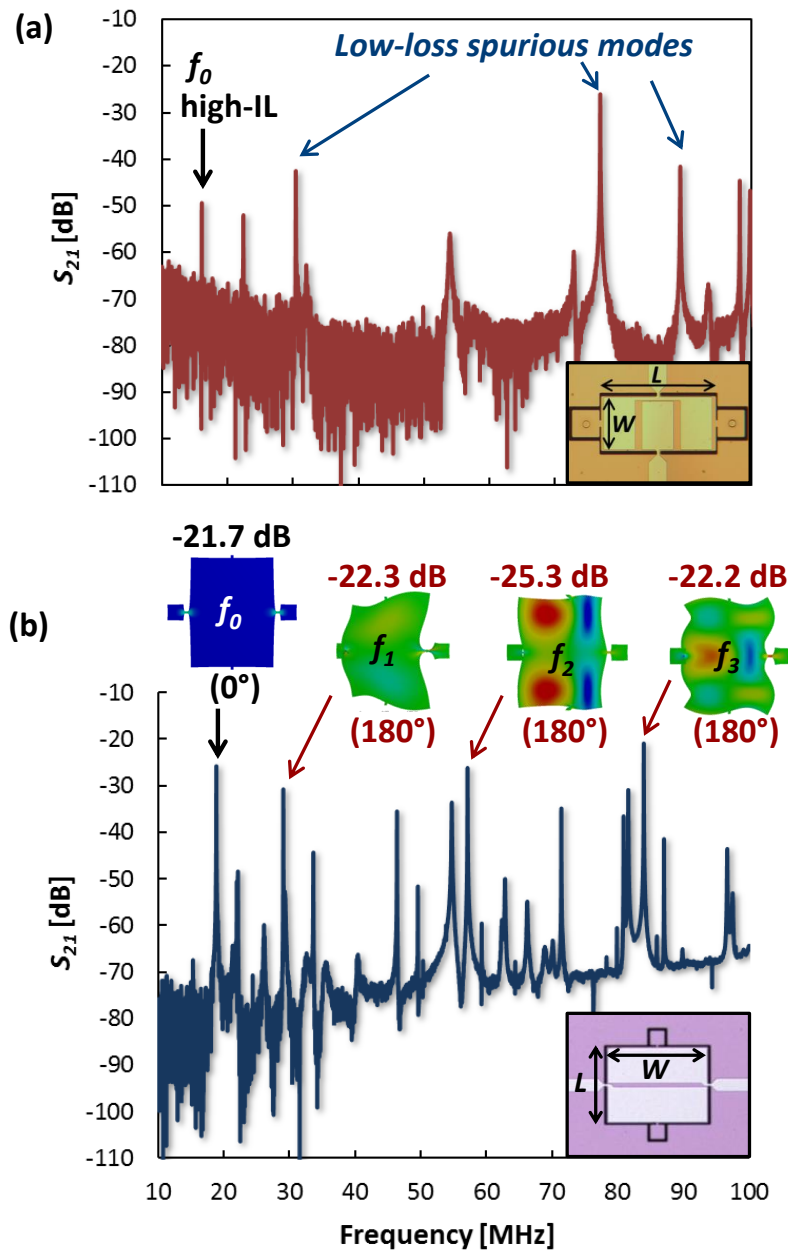


Figure 4.15: Wide-span frequency response for (a) 16-MHz sensor (inset: optical image); (b) 19-MHz sensor with improved IL and spurious suppression. Peaks within 5 dB IL of f_0 have 180° phase shift (inset: optical image of fabricated device).

4.3.2 FUNCTIONALIZATION FOR TOLUENE AND XYLENE SENSING

Prior to functionalization, the uncoated sensor was characterized in an ESPEC environmental chamber and reported a temperature coefficient of frequency (TCF) of -30 ppm/°C at 19 MHz. Since AlN-on-Si thermometers are easily incorporated into the sensor array, the large, linear TCF is useful for accurate monitoring and correction of temperature-induced frequency shift [75] as well as determination of relative humidity levels [76].

To validate sensor performance for VOC detection, the Nano eNabler was used to coat released devices with the appropriate functional material. Polyimide, polyethyleneimine (PEI), and similar polymers have been commonly used for detection of polar compounds (e.g. water vapor) [76]. However, the most frequently-appearing indoor chemical pollutants [77] are hydrocarbons consisting of non-polar molecules. Sorption-based resonant VOC sensing has employed polymers such as polyisobutylene (PIB), polydimethylsiloxane (PDMS) [78], and photoresist [79], which exhibit a strong affinity for non-polar compounds. In this work, PIB was selected based on favorable sorption characteristics for toluene and xylene.

PIB, which is commercially available in solid form (Sigma-Aldrich), is typically dissolved using organic solvents such as toluene or xylene. Since the Nano eNabler is designed for biological functionalization, deposition conditions can be controlled better for aqueous solutions. Nanoliter volumes of highly volatile substances (at room temperature, toluene vapor pressure = 2.92 kPa, xylene vapor pressure = 1.33 kPa) are likely to evaporate within seconds during deposition. In the same way that polymer patterning in section 4.2.3 required mixing PEI with a lower-vapor-pressure solvent, PIB

solution requires a second solvent such as diethyl phthalate (DEP), which has been used to facilitate non-polar polymer printing [80] (vapor pressure 0.22 Pa), to prevent evaporation. Trials for various PIB/toluene concentrations and ratios of PIB/toluene to DEP revealed that mixing as little as 0.1% DEP with a 2% PIB/toluene solution was optimal for complete polymer transfer onto annexed platforms without requiring multiple depositions to achieve uniformly thick PIB films (Figure 4.16).

The sensor functionalization process (Figures 4.17b-d) began with preparation of a 2% PIB/toluene solution, which was subsequently diluted in DEP. An SPT loaded with the resulting solution was used to deposit PIB by contacting the SPT to each platform. Following deposition, sensors were baked on a hotplate at 125 °C for two hours to remove any remaining solvent. LEXT confocal imaging of the 1- μm thick PIB patterns revealed a slight dome-shaped profile. Mass loading from the PIB causes f_0 to decrease after patterning; however, the initial Q of 3400 increases slightly to 3700 (Figure 4.18a).

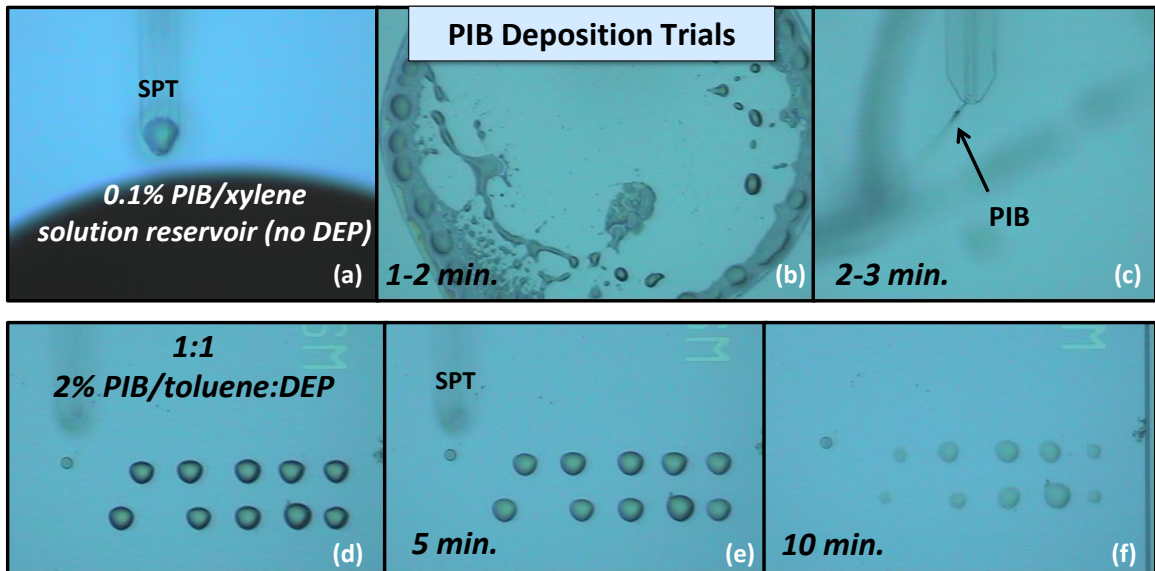


Figure 4.16: Optical images of Nano eNabler patterning trials with various PIB solutions: (a-c) 0.1% PIB/xylene solution with no DEP added, showing quick evaporation of a micro-pipetted drop in 3 minutes; (d-f) 1:1 ratio of 2% PIB/toluene to DEP. Optical images over a 10-minute time period show very little polymer remaining upon DEP evaporation.

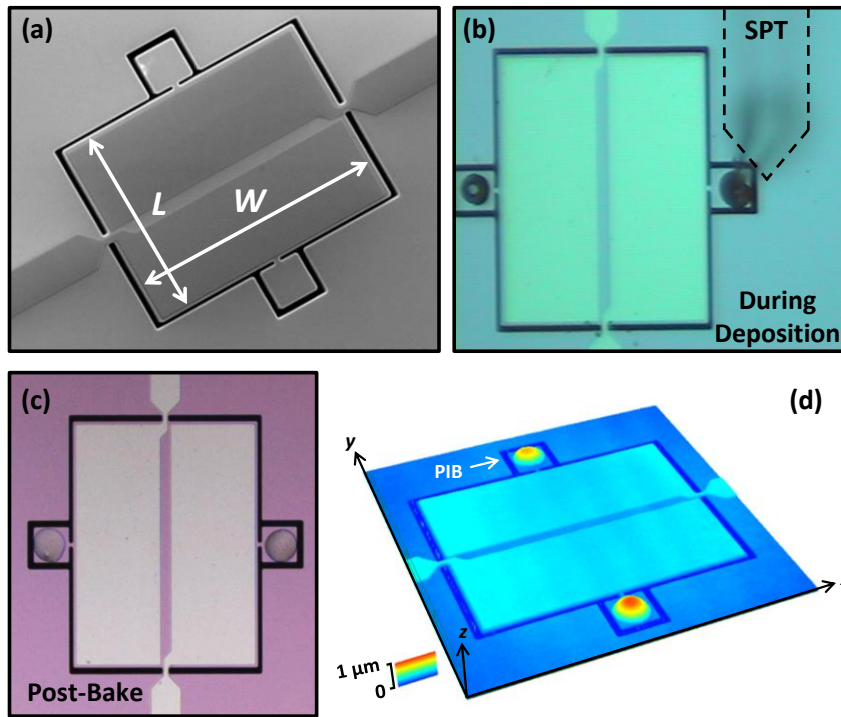


Figure 4.17: (a) SEM image of unpatterned AlN-on-Si sensor; (b) optical image of sensor during PIB patterning (SPT shown above right platform); (c) optical image of PIB-patterned sensor; (d) Olympus LEXT thickness profile of PIB on platforms (z -axis exaggerated to clearly illustrate PIB pattern shape).

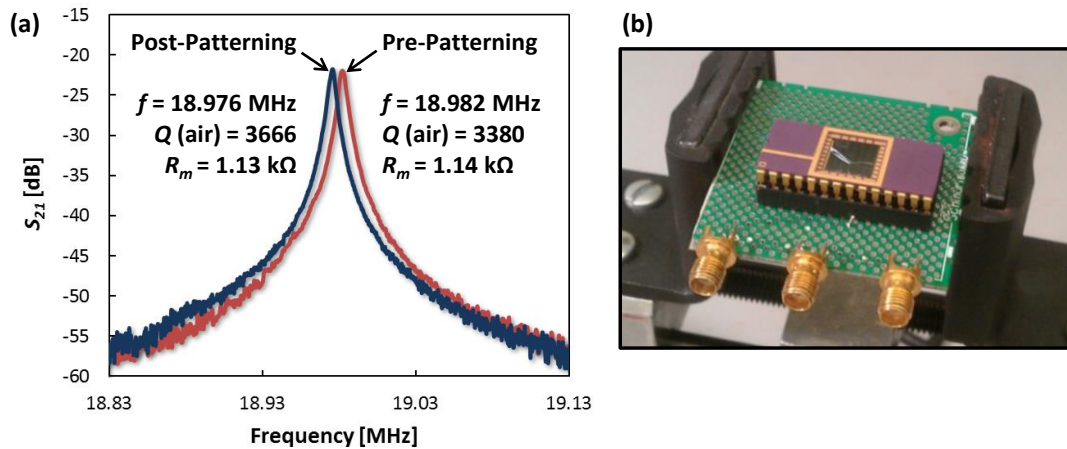


Figure 4.18: Measured frequency response before and after PIB patterning; (b) photo of customized test board for VOC sensor testing.

4.3.3 EXPERIMENTAL SETUP AND SENSOR MEASUREMENT RESULTS

Professor Oliver Brand provided equipment and laboratory space for VOC sensor characterization. Patterned devices were wirebonded to a 28-pin DIP chip carrier, which was inserted into a test board containing SMA connections to interface with an HP 4395A network analyzer (Figure 4.18b). The gas mixing setup described in [81] was used to generate three-minute exposures to various toluene and xylene concentrations, which were each followed by a three-minute nitrogen purge to refresh the PIB. Based on the saturation concentration of each VOC at room temperature and atmospheric pressure, the VOC concentration delivered to the sensor was controlled by adjusting flow ratios between N_2 and analyte lines (total flow rate = 80 mL/min). Frequency measurements were acquired at 15-second intervals and plotted over time (Figures 4.19 and 4.21). In all VOC tests conducted, the sensor response to toluene and xylene was reversible and repeatable after briefly exposing the PIB film to analyte-free air.

Toluene testing revealed a linear sensitivity of -0.09 Hz/ppm from 3600 to 14400 ppm toluene. To confirm that the observed frequency change was primarily due to mass loading in the PIB film, an uncoated sensor was measured upon exposure to 20600 ppm toluene, where a 224 Hz shift, nearly 10 \times lower than the PIB-patterned sensor, was measured. The Q_0 of 3700 was unaffected by subsequent mass loading from toluene exposure, exhibiting less than 10% reduction up to 14400 ppm toluene. In comparison, a 29-MHz mode from the same device (f_1) demonstrated a less linear sensing behavior. The initial Q_1 of 10,500 was reduced to 8500 after PIB patterning and degraded by nearly 50% at a toluene concentration of 14400 ppm (Figure 4.20).

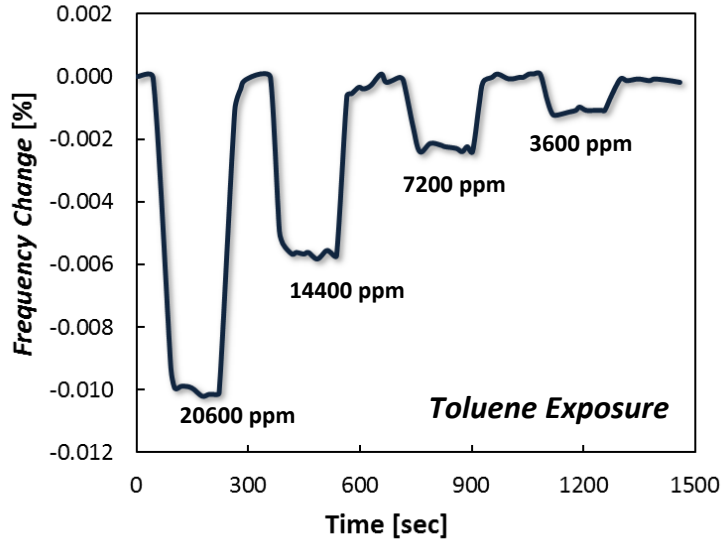


Figure 4.19: Measured frequency change for toluene concentrations of 20600 ppm, 14400 ppm, 7200 ppm, and 3600 ppm.

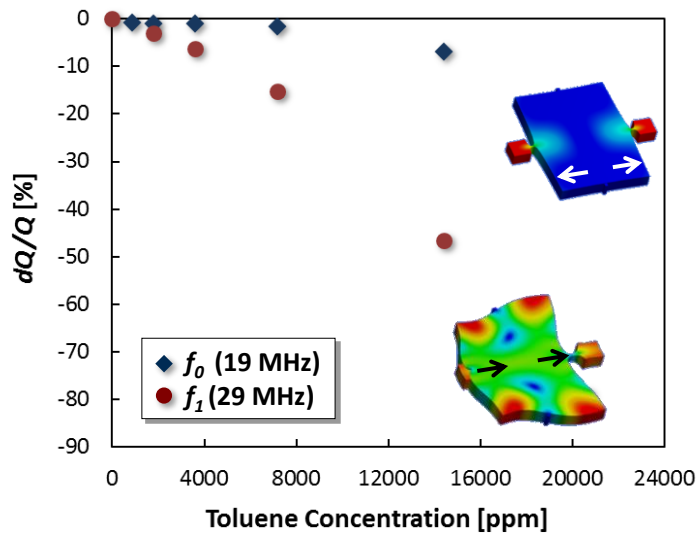


Figure 4.20: Measured change in Q vs. toluene concentration for sensing mode f_0 compared to 29-MHz mode f_1 ; arrows denote platform motion.

Since the saturation concentration of xylene is approximately three times lower than that of toluene at room temperature and atmospheric pressure, lower xylene concentrations were achievable using the same setup. Additionally, the xylene partition coefficient (ratio of analyte concentration in the polymer to the concentration in the surrounding environment) is two times larger than the toluene partition coefficient [38].

Therefore, xylene sorption is expected to be about twice as large as toluene sorption. Measurements revealed a linear sensitivity of -0.18 Hz/ppm from 625 to 3750 ppm xylene (Figure 4.21). Similar to toluene exposure results, Q_0 was minimally affected while Q_1 severely degraded with mass loading from xylene sorption in the PIB film (Figure 4.22).

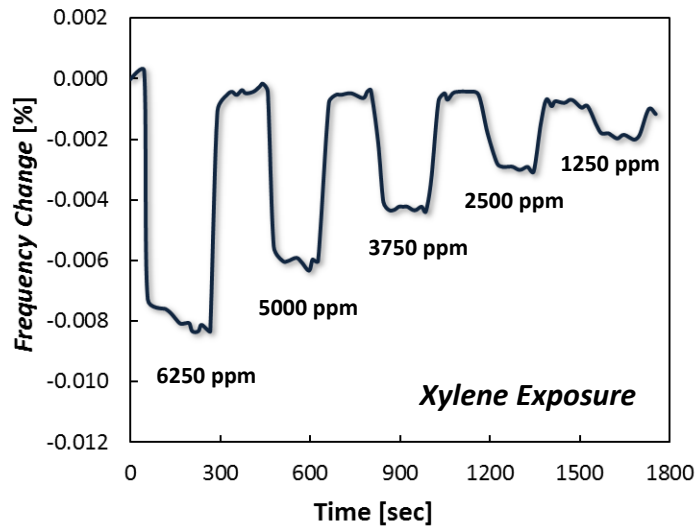


Figure 4.21: Measured frequency change for xylene concentrations of 6250 ppm, 5000 ppm, 3750 ppm, 2500 ppm, and 1250 ppm.

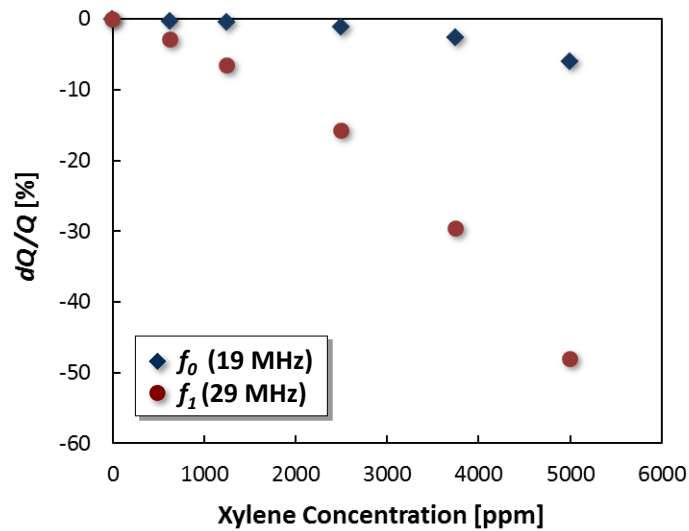


Figure 4.22: Measured change in Q vs. xylene concentration for f_0 and f_1 (for comparison).

4.3.4 HUMIDITY EFFECTS ON VOC MEASUREMENTS

Because true ambient air contains a mixture of gases rather than pure substances, effects of water vapor in the sensing environment were investigated by delivering moist air mixed with N₂ and toluene to the sensor. Relative humidity (RH) contributed to an additional downshift in frequency (Figure 4.23); however, sensor measurements with moist air (but no analyte) revealed that Q_0 and Q_1 exhibited less than 5% degradation

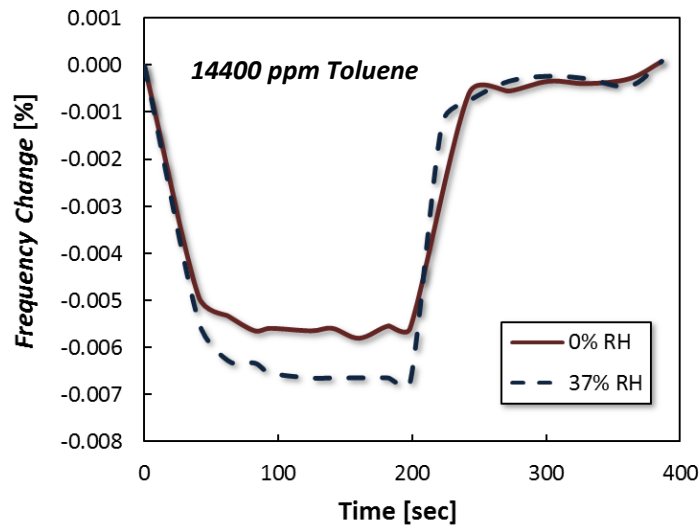


Figure 4.23: Measured frequency change for xylene concentrations of 6250 ppm, 5000 ppm, 3750 ppm, 2500 ppm, and 1250 ppm.

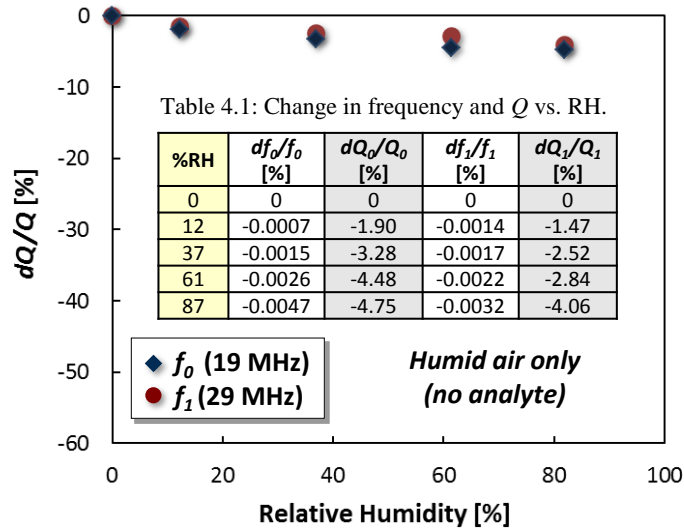


Figure 4.24: Measured change in Q vs. relative humidity (RH) for f_0 and f_1 of PIB-coated sensor.

from 0% to 82% RH (Figure 4.24, results summarized in Table 4.1). Considering the significant Q_f degradation upon mass loading due to toluene and xylene (Figures 4.20 and 4.22), it is reasonable to conclude that water vapor could not have been adsorbed by the PIB. Because this behavior is expected based on the non-polar affinity of PIB, the additional downshift in frequency is most likely related to surface adsorption onto the AlN film [82]. In future implementations, surface treatment on non-designated sensing areas can help prevent undesired adsorption for improved analyte selectivity.

Table 4.2 summarizes properties of the AlN-on-silicon sensor in this work along with other resonant toluene sensors in literature for fair comparison. This sensor demonstrates a high Q that remains unaffected by mass loading, therefore minimizing effects of undesired frequency error. Additionally, the low R_m (nearly three orders of magnitude lower than capacitive sensors [83]) facilitates low-power oscillator implementation. Sensitivity can be improved by selecting or engineering a material with optimal sorption properties for the target analyte as well as designing the resonator with enhanced gravimetric sensitivity [58].

The studied effects of temperature and humidity on sensor response further confirm the need for integrated sensing. Since the die area of 200 x 200 μm is significantly smaller than typical QCM, SAW, and cantilever sensors, large-scale resonator arrays can be practically implemented in a multi-sensing platform.

Table 4.2: Comparison of resonant toluene sensors in literature.

Ref.	Type/actuation method	f [MHz]	Q	R_m [k Ω]	Sensitivity [ppm _{freq.} /ppm _{toluene}]	Functional material	Dimensions
This work	AlN-on-Si	19	3700	1.1	.005 (3600 – 14400 ppm)	PIB	186 x 206 μ m
Johnston [78]	FBAR (ZnO)	1440	170	-	.005 (1000 – 5200 ppm)	PDMS	100 x 100 μ m
Debéda [84]	Cantilever (PZT)	0.07	142	-	.2 (260 – 1050 ppm)	PEUT	8 x 2 mm
Konno [83]	Capacitive (Si)	5	1826	750	.012 (1000 – 2000 ppm)	PBD	100 x 100 μ m
Sayago [85]	SAW (ST-X quartz)	158	-	-	.02 (25 – 200 ppm)	PIB	mm
Truax [38]	Disk (Si, thermal)	0.4	2600	-	0.1 (2000-16000 ppm)	PIB	400 x 340 μ m
Si [86]	QCM	10	-	-	.016 (200 – 1000 ppm)	P3HT	mm diameter

*Polymer functional material acronyms: polyisobutylene (PIB), polydimethylsiloxane (PDMS), polyetherurethane (PEUT), polybutadiene (PBD), poly(3-hexylthiophene) (P3HT).

5 TPOS DUAL-MODE RESONATORS AND OSCILLATORS FOR TEMPERATURE MEASUREMENT

Microelectromechanical system (MEMS) oscillators based on single-crystal silicon resonators are especially promising candidates for integrated timing and sensing applications. However, achieving a highly-stable oscillator output is challenging when the frequency of silicon-based devices varies with temperature by approximately -30 ppm/ $^{\circ}\text{C}$. Passive techniques such as engineering device geometry [61] and degenerate doping [87] have reduced the silicon TCF to as low as -3.6 ppm/ $^{\circ}\text{C}$ and -1.5 ppm/ $^{\circ}\text{C}$, respectively. Traditional methods using a layer of positive-TCF oxide to counteract the negative TCF of silicon [88] are susceptible to process variations and may also degrade the resonator Q . Rather than depositing surface oxide, embedding oxide pillars inside the silicon structure completely eliminates the first-order TCF of high- Q AlN-on-silicon resonators, resulting in just 90-180 ppm frequency drift over 120°C [59]. Even with significant advances in material compensation, electronic tuning is still necessary to achieve zero-TCF oscillators. Active temperature compensation has been demonstrated using MEMS-based oscillators [89-91], but investigation of thermometry methods for silicon-based oscillators are beneficial to both timing and sensing applications.

Accurate temperature measurement requires a sensor to be in close proximity to the oscillator or sensor system, thereby reducing discrepancies caused by thermal gradients. Compensating for temperature-induced frequency shift using the resonator itself has been explored in quartz oscillators, since frequency can be measured with high accuracy. Dual-mode (DM) excitation, which exploits the dependence of frequency on physical properties of the resonator, has been utilized to simultaneously monitor multiple

quantities (e.g. stress, mass, pressure, or temperature [92-94]). Tracking internal resonator temperature via DM operation provides a local measurement without external thermometers, which significantly reduces overall system footprint when integrated with CMOS electronics. While quartz-based DM oscillators have been heavily researched over the past few decades, the DM concept has only recently been demonstrated in silicon-based MEMS oscillators [75].

5.1 DUAL-MODE TEMPERATURE MEASUREMENT

5.1.1 PRINCIPLE OF OPERATION

Dual-mode temperature sensing requires simultaneous excitation of two resonance modes in a single device. Both modes experience identical changes in ambient temperature but have unique frequency dependence on temperature [16]. The frequency-temperature characteristics of f_1 and f_2 can be used to compensate reference frequency f_1 over temperature. The DM oscillator output, beat frequency f_b , is defined by a linear combination of the two modes:

$$f_b = \alpha \cdot f_1 - f_2. \quad (9)$$

Multiplicative constant α is an integer when f_2 is an α -order harmonic of f_1 [16]. If the modes are close in frequency, f_1 and f_2 are directly mixed to generate f_b [95].

The relative change in frequency f_0 with respect to temperature, or TCf_0 , can be expressed as

$$TC^n f_0 = \frac{1}{f_0} \frac{\partial^n f_0}{\partial T^n}. \quad (10)$$

Since silicon has a dominant first-order temperature coefficient, TCF refers to TC^1F here.

Based on (9) and (10), DM temperature sensitivity TCf_b is expressed as

$$TCf_b = \frac{\alpha \cdot f_1 \cdot TCf_1 - f_2 \cdot TCf_2}{f_b}. \quad (11)$$

As f_b approaches a minimum value, $\alpha \cdot f_1 \cong f_2$, which relates TCf_b to f_2 , f_b , and the difference in TCF between modes ($TCf_1 - TCf_2$, or ΔTCF):

$$TCf_b \cong \frac{f_2}{f_b} (TCf_1 - TCf_2). \quad (12)$$

The linear TCF of silicon ensures that TCf_b would also be a strongly linear function of temperature, which enables compensation of reference oscillator frequency f_1 over temperature.

5.1.2 DUAL-MODE OSCILLATOR CONSIDERATIONS

Real-time measurement and compensation requires circuitry to drive and sustain oscillations across a wide temperature range. Various architectures have been used to implement quartz DM oscillators, which can be categorized as either single-loop or dual-loop configuration [95, 96]. Single-loop (Colpitts) oscillators (Figure 5.1a) require fewer components than a dual-loop oscillator and can exploit transistor nonlinearities to inherently provide f_b as an output [95, 96].

Dual-loop DM oscillators (Figure 5.1b) can be implemented if separate gain and phase control are required. The Barkhausen stability criterion, which states that a circuit will sustain oscillations under certain loop gain and phase conditions, must be satisfied at both frequencies in a DM oscillator. Unity loop gain is achieved by ensuring that the transimpedance amplifier (TIA) provides sufficient gain to compensate resonator motional resistance (R_m). Phase conditions are met if the combined TIA and resonator phase results in zero loop phase shift.

In addition to resonator phase and motional resistance R_m , Q of both modes directly affects oscillator phase noise and consequently, temperature measurement linearity [75]. Careful design of resonators with proper phase, low R_m , and high Q ensures successful DM oscillator interfacing.

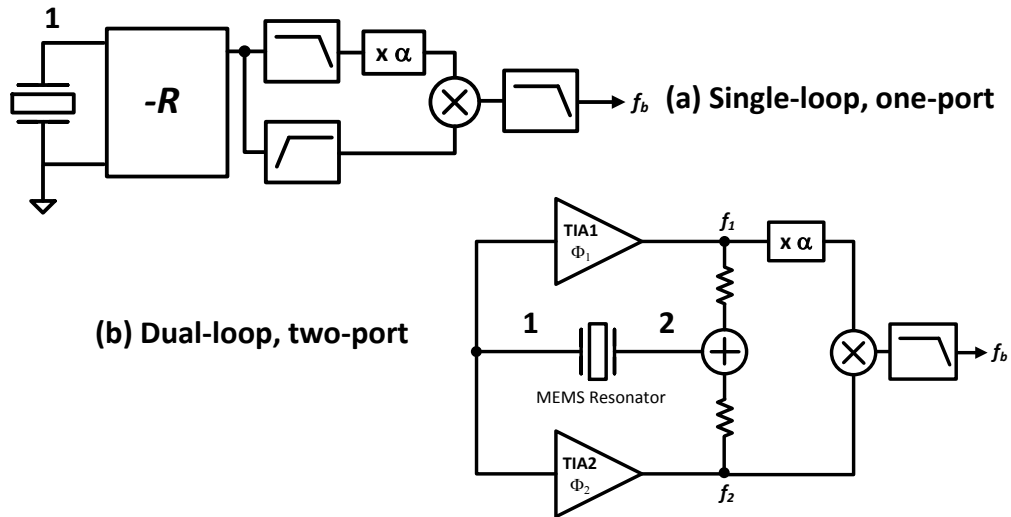


Figure 5.1: (a) Single-loop Colpitts oscillator with one-port resonator; (b) dual-loop DM oscillator with two-port MEMS resonator in feedback with TIAs followed by mixing, multiplication, and filtering blocks to generate output frequency f_b .

5.1.3 TPOS DUAL-MODE RESONATORS

Quartz-based DM stress and temperature measurement exploited a temperature-compensated C-mode and an uncompensated B-mode with TCF ~ -26 ppm/ $^{\circ}\text{C}$ [92-94]. Although two modes with such different temperature characteristics are not readily available in silicon, a similar micromachined thermometry concept has been employed in [64]. The dual-resonator sensor utilized a surface oxide-compensated resonator and uncompensated resonator to obtain a large ΔTCF between the two modes, and small f_b was obtained by designing f_2 close to f_1 . The dual-resonator thermometer was more sensitive than single-mode temperature sensing, but using two devices increases die area and may cause measurement inaccuracies. A self-temperature sensing approach using Lamé and square-extensional modes in [97] provides a single-resonator alternative. However, both [64] and [97] are based on electrostatically-transduced (capacitive) resonators, which have high motional impedance and create difficulties in oscillator implementation. The required DC polarization voltage (V_p) further increases power consumption and may contribute to undesired measurement inaccuracies via temperature-induced V_p variations.

On the other hand, piezoelectric actuation enables multiple-mode excitation in a single device without DC voltages. Thin film piezoelectric-on-substrate (TPoS) technology combines the advantages of piezoelectric transduction with a low-loss material such as silicon, which exhibits high- Q and enhanced power handling over piezoelectric-only resonators [39].

5.2 ZNO-ON-SI DUAL-MODE OSCILLATOR

A dual-frequency oscillator in [98] was built from a TPoS resonator with discrete circuitry designed to switch between modes. To eliminate manual switching, we present a DM oscillator comprising a ZnO-on-Si resonator interfaced with custom-designed integrated circuits (ICs), which demonstrates the first micromachined alternative to DM quartz thickness-shear “C” mode oscillators [16, 96].

5.2.1 SYSTEM ARCHITECTURE

The ZnO-on-Si DM oscillator simultaneously excites fundamental and third-order length-extensional frequencies (f_1 and f_3) by the architecture shown in Figure 5.2. The resonator is connected in feedback with a 0° TIA, which locks into oscillations at f_1 , and a 180° TIA that locks into oscillations at f_3 . The resistive divider comprising R_1 and R_2 isolates oscillator outputs f_1 and f_2 to minimize loading effects. In a complete DM interface and readout system, filters outside the feedback loops remove unwanted signal components at each amplifier output. f_1 is then multiplied and mixed with f_3 , after which the signal is filtered again to extract f_b ($f_b = 3f_1 - f_3$). While all system blocks would

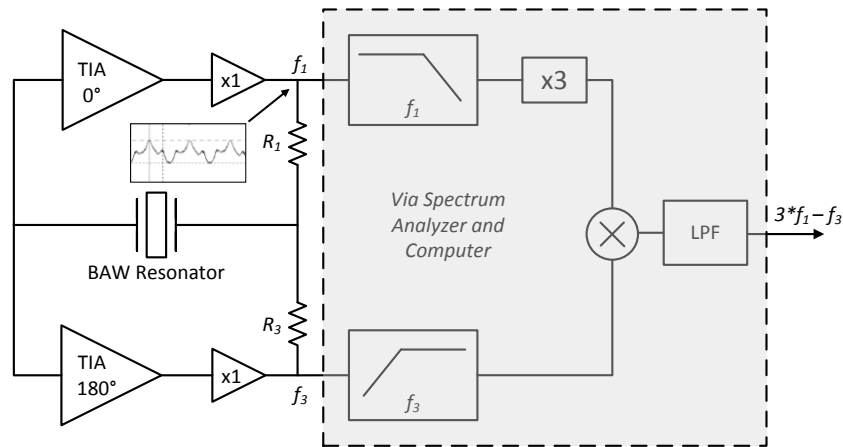


Figure 5.2: Block diagram of dual-mode (DM) interface and readout architecture for ZnO-on-Si BAW resonator.

ultimately be integrated on-chip, measurements for this work were performed via spectrum analyzer and data post-processing to extract f_b .

Expressing (9) as $f_b = 3 \cdot f_1 - f_3$ to describe the selected modes, (11) becomes

$$TCf_b \cong \frac{3 \cdot f_1 \cdot TCf_1 - f_3 \cdot TCf_3}{f_b}. \quad (13)$$

If $3 \cdot f_1 \cong f_3$ as in [16], (13) is approximated by

$$TCf_b \cong \frac{f_3}{f_b} (TCf_1 - TCf_3), \quad (14)$$

highlighting the strong dependence of TCf_b on TCF difference between first and third modes ($TCf_1 - TCf_3$, or ΔTCF). Additionally, the ratio $3f_1/f_b$ can be adjusted to enhance TCf_b .

5.2.2 DUAL-MODE RESONATOR DESIGN

Fundamental and third-order length-extensional modes (f_1 and f_3) can be sensed using an interdigitated electrode configuration. Matching input and output electrodes to alternating strain fields of the third-order mode creates a 180° electrical phase difference between resonator input and output at f_3 (Figure 5.3). Since the entire device undergoes uniform expansion and contraction at f_1 , no phase change occurs between input and output. The 180° phase difference between modes ensures that each resonance mode is

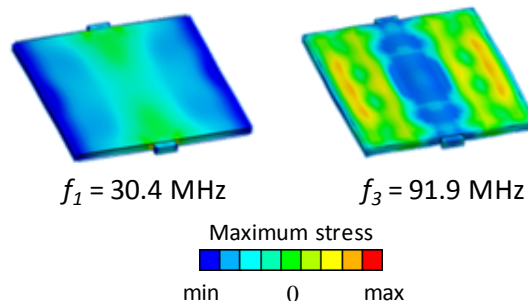


Figure 5.3: ZnO-on-Si BAW mode shapes at f_1 and f_3 .

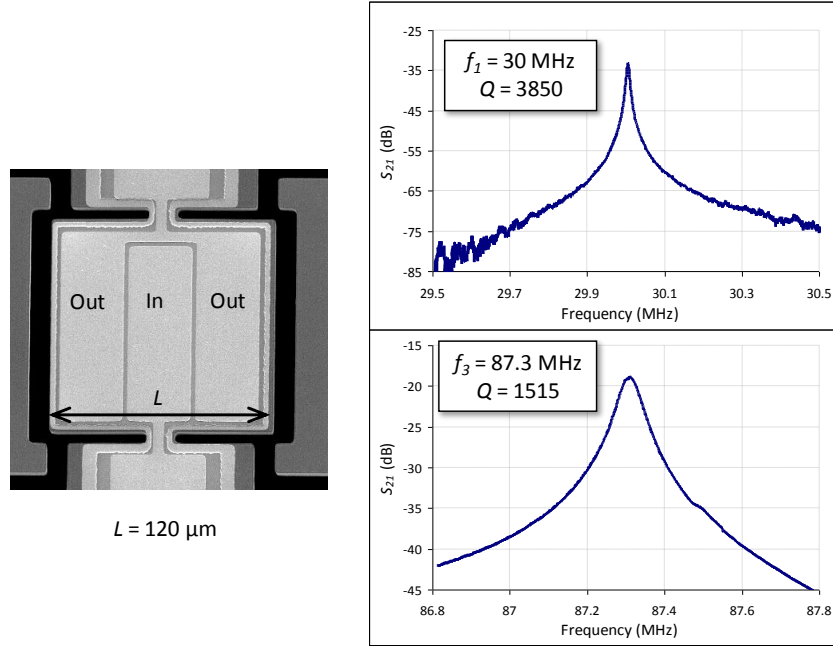


Figure 5.4: SEM image and frequency response of ZnO-on-Si DM resonator.

isolated from the other and enables individual tuning to produce an optimized signal at the DM oscillator output that meets the Barkhausen criterion for sustained oscillations [95]. The measured frequency response of f_1 and f_3 using the proposed electrode configuration is shown in Figure 5.4.

5.2.3 INTERFACE CIRCUITRY

Each feedback loop in the DM oscillator contains two amplifiers. A front-end TIA (AMI 0.6 μm) provides the required phase shift to lock into oscillations at both frequencies – 0° for f_1 and 180° for f_3 . A discrete buffer (TI OPA656) follows each TIA to isolate the resistive voltage divider load from the IC output. The voltage divider sums the two signals and feeds them back to the resonator input.

Each CMOS IC consists of a front-end TIA with an inverting pair connected in feedback by M_f (Figure 5.5). $V_{\text{bias},\varphi}$ (resonator phase φ equals 0° or 180°) is separately

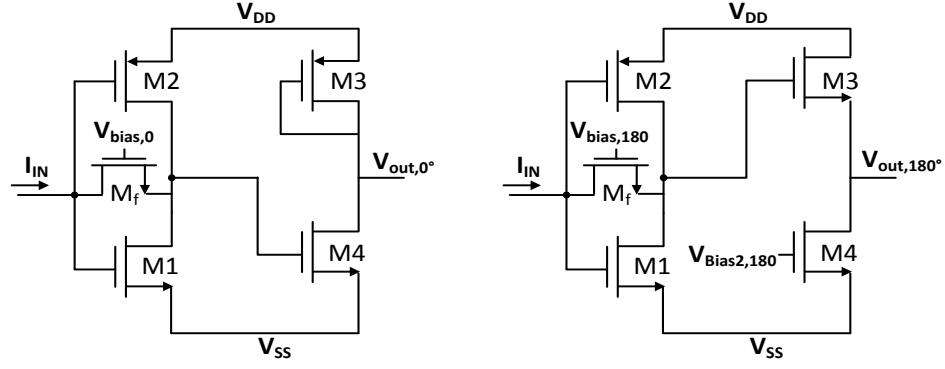


Figure 5.5: Schematics of interface ICs for f_1 (left) and f_3 (right).

adjusted in both feedback loops to prevent the desensitization effect characterized by (15) from pulling the loop out of dual-oscillations. A second amplification stage is added after each TIA to minimize loading effects of parasitic capacitances at the resonator input and output terminals. These amplifiers also provide the additional phase swing needed to create a total shift of 0° around the feedback loop. Since the TIA inherently provides 180° phase shift, a common source output stage provides an additional 180° for the f_1 IC. A source-follower amplifier maintains the total loop phase shift at 180° in the f_3 IC.

To sustain dual oscillations, the loop gain of each signal path is controlled such that $A_{f3} \sim A_{f1}$. When a system contains two interfering signals of different amplitudes, the signal with larger amplitude will act on third-order nonlinearities in the amplifier and attenuate the amplifier gain, as given by (15):

$$a'_1 = a_1 \left(1 + \frac{3a_3}{2a_1} V_i^2 \right) \quad (15)$$

where a_1 represents the small signal gain of the amplifier, a_3 the gain compression caused by the interfering signal on the third-order nonlinearity of the amplifier ($a_3/a_1 < 0$), and V_i the amplitude of the interfering signal [99]. If one signal is significantly larger than the other, the resulting attenuation of the feedback amplifier causes the mode with lower

amplitude to drop out of oscillation. Therefore, gain tuning is added to ensure that oscillations are maintained while simultaneously generating both frequencies.

5.2.4 OSCILLATOR MEASUREMENT AND CHARACTERIZATION

The resonator was independently excited at f_1 (30 MHz) and f_3 (87.3 MHz) and measured in single-mode (SM) oscillation conditions. Both loops were then simultaneously connected in feedback with the resonator for DM operation. Oscillator functionality was verified by an external measurement setup. SM operation of f_1 or f_3 produced a sinusoidal wave with single frequency component on the oscilloscope (Figure 5.6) and corresponding peaks (with harmonics of f_1) on the spectrum analyzer output (Figure 5.7). DM operation produced an output containing both f_1 and f_3 (Figure 5.7). The spectrum analyzer showed distinct peaks at f_1 and f_3 in DM operation, with an additional peak at $f_{mix} = f_3 - f_1$ (57.3 MHz) (Figure 5.7). This peak resulted from mixing between the two modes across the interface electronics, which was confirmed by examining the spectra in SM operation of f_1 or f_3 (f_{mix} only exists in simultaneous excitation).

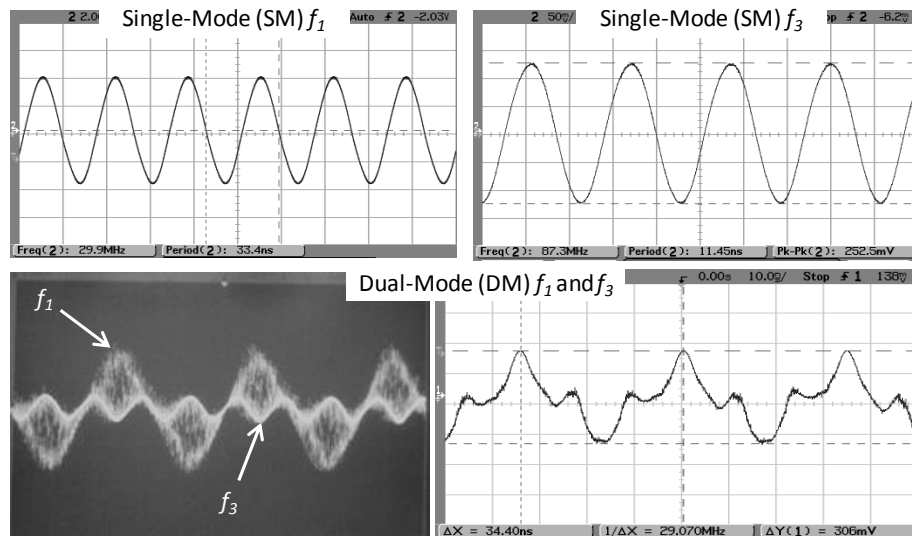


Figure 5.6: (top) Measured oscillator response for f_1 and f_3 SM excitation; (bottom left) DM excitation at f_1 and f_3 ; (bottom right) DM output signal after averaging.

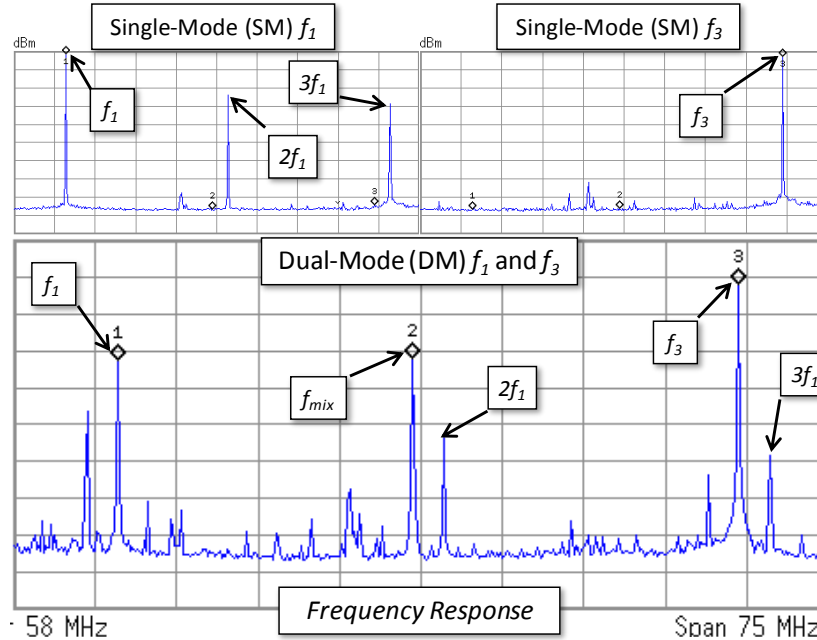


Figure 5.7: (top) Spectral response for f_1 and f_3 SM excitation; (bot.) DM excitation with f_{mix} at 57.3 MHz.

The phase noise performance of f_3 in SM and DM excitation (Figure 5.8) was measured using the Agilent N5500A phase noise test set. The lower output power of during DM operation prevented f_1 measurement. In DM operation, a 10-20 dBc degradation between $f=1\text{kHz}$ and $\sim 1\text{MHz}$ is observed; however, as f approaches 1 MHz, the DM architecture phase noise improves beyond that of SM excitation. Closer examination of f_3 reveals the presence of a secondary tone near resonance in DM operation, which was not observed in SM excitation of f_3 . Amplifier nonlinearity was suspected to cause cross-modulation between f_1 and f_3 and generate a frequency close to f_3 , which resulted in a $1/f^2$ phase noise profile (-20 dB/dec) at small offsets and a constant noise floor at large offset [100]. The secondary mode may also cause the analyzer to lock into this mode during measurement, resulting in a sharper drop in phase noise performance than expected.

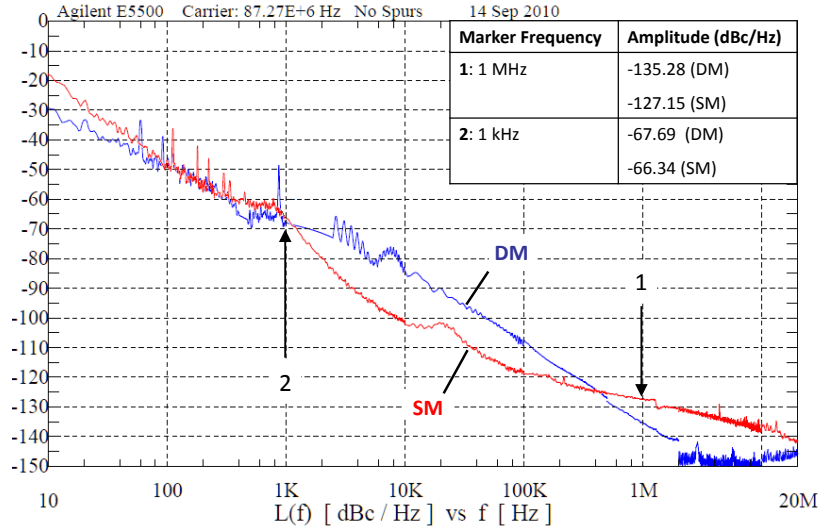


Figure 5.8: Measured f_3 phase noise response in SM and DM configuration.

Following phase noise analysis, the DM oscillator was placed in an ESPEC SH-240 chamber, where the temperature was cycled from -40°C to 100°C . f_1 and f_3 were measured with an Agilent E4407B spectrum analyzer across temperature. TCf_1 and TCf_3 , the TCF values of each frequency in DM operation, were determined to be $-34\text{ ppm}/^{\circ}\text{C}$ and $-40\text{ ppm}/^{\circ}\text{C}$, respectively (Figure 5.9). Extracted TCf_b was $+162\text{ ppm}/^{\circ}\text{C}$, showing an enhancement in temperature sensitivity compared to measuring f_1 or f_3 separately. Because f_b is fairly large at 3 MHz, TCf_b can be more accurately predicted using (13) rather than (14).

Resonator Q loading in simultaneous DM excitation causes significant jitter (frequency uncertainty) at f_1 and f_3 [75], which directly affects the accuracy of frequency--and ultimately temperature--measurement. To determine the effects of Q_{f_1} and Q_{f_3} on the output signal linearity, several devices were tested over temperature, after which the correlation coefficient of the temperature measurement (R^2) was plotted against Q_{min} , the minimum Q of the two operating modes (Figure 5.10). Significant variation exists between TCF measurements for a low Q_{min} , resulting in poor linearity and a low R^2 .

However, increasing Q_{min} improves temperature measurement linearity, suggesting a logarithmic relationship between Q_{min} and R^2 . Thus, high Q of both modes is crucial to performing accurate temperature measurements using DM oscillators.

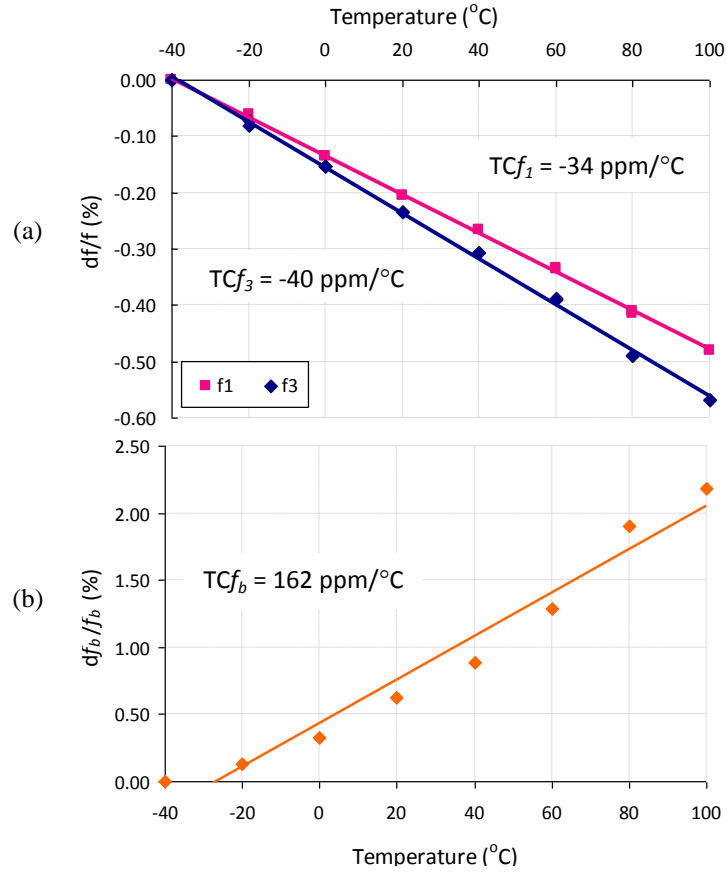


Figure 5.9: Measured temperature response of (a) f_1, f_3 ; (b) f_b .

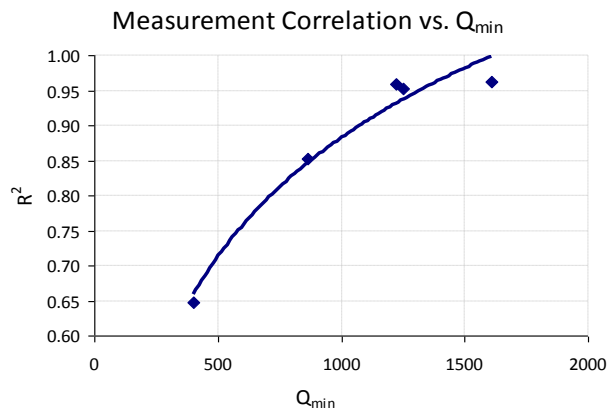


Figure 5.10: Measurement correlation (R^2) vs. Q_{min} .

5.3 OPTIMIZED ALN-ON-SI DUAL-MODE RESONATORS

Based on (12), a large f_2 combined with small f_b provides enhanced DM temperature sensitivity (ratio f_2/f_b). In-plane bulk modes of AlN-on-Si resonators provide lithographically-defined frequencies that can be exploited for DM operation. Further TCf_b improvements are achievable by maximizing ΔTCF ($TCf_1 - TCf_2$), which is influenced by temperature coefficients of independent elastic constants (TCc_{11} , TCc_{12} , and TCc_{44}) and their contributions to the selected modes [101].

5.3.1 LIMITATIONS OF FUNDAMENTAL AND HIGHER-ORDER MODES

DM quartz thermometers based on first and third harmonic C-modes have demonstrated f_b values in the 150-kHz range ($f_b = 3 \cdot f_1 - f_3$) [16, 95]. In previous DM demonstrations, TPoS resonators employed first and third width-extensional (WE) modes [75, 98], which tend to suffer from larger f_b . One factor causing WE/WE3 resonators to deviate from the ideal situation ($\alpha = 3$) is support size, which creates non-uniformities in the f_1 strain pattern and shifts the frequency from the nominal value. However, finite element simulations show that even with zero support size, f_b reaches a lower limit for the given dimensions (Figure 5.11). Since width W determines frequency, the only variable dimension is length L , which also provides minimal f_b reduction as measured in fabricated resonators (Figure 5.12).

Because f_1 and f_3 have the same elastic dependencies, small ΔTCF is also expected. For the devices measured in Figure 5.12, $\Delta TCF = -0.5$ ppm/°C yields $TCf_b \sim -37$ ppm/°C, which provides virtually no improvement over single-mode measurement. Since extensional modes in TPoS resonators possess similar temperature-frequency behavior and large f_b , alternative modes for TCf_b enhancement are investigated.

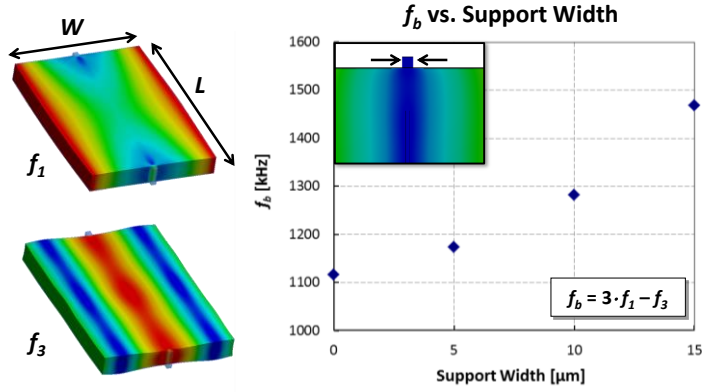


Figure 5.11: (left) strain distribution for DM AlN-on-Si resonator based on first and third width-extensional (WE/WE3) modes; (right) simulated f_b vs. support width for a 27-MHz resonator ($W = 156 \mu\text{m}$).

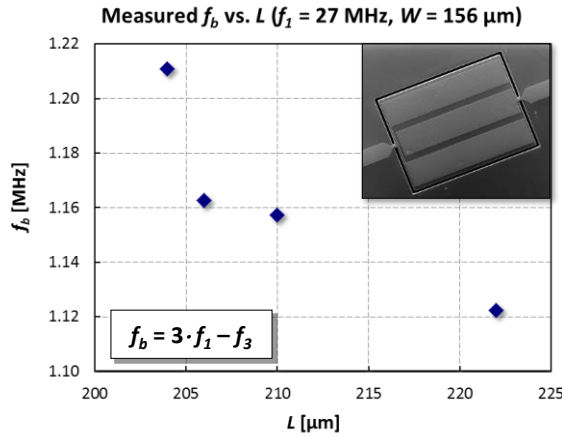


Figure 5.12: Measured f_b vs. length L for AlN-on-Si WE/WE3 resonator; (inset) SEM image of device with interdigitated electrodes to excite WE and WE3 modes.

5.3.2 TCF_B ENHANCEMENT BY BEAT FREQUENCY REDUCTION

In-Plane Width-Extensional and Width-Shear Modes

The WE mode frequency is nearly independent of resonator length (L) and is defined by

$$f_{WE} = \frac{v}{2W'} \quad (16)$$

where v is the effective longitudinal wave velocity. On the other hand, the width-shear (WS) mode (Figure 5.13) exhibits a significant dependence on L , which can be exploited to define specific f_b values by controlling the distance between WS and WE modes ($f_b = f_{WS} - f_{WE}$) (Figure 5.14). Utilizing WS and WE modes for DM operation provides inherently small f_b by directly mixing two frequencies rather than utilizing fractional multiplication to obtain a desired f_b [96]. $L/W = 1.31$ corresponds to the case when $f_{WS} = f_{WE}$, or zero f_b . Because f_b is determined by a ratio rather than absolute dimensions, DM excitation using WS and WE modes is less sensitive to lithography and process variations. Furthermore, the WS/WE resonator electrode configuration provides a 180°

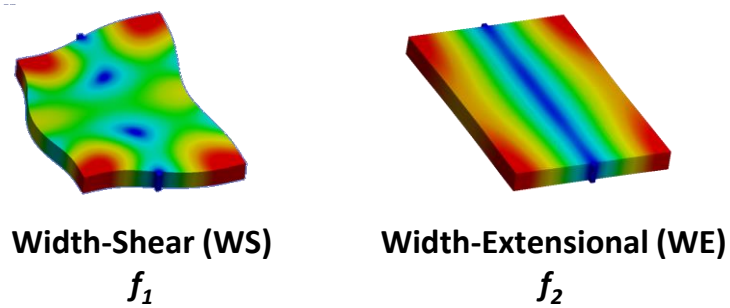


Figure 5.13: ANSYS mode shapes of width-shear (WS) and WE modes for dual-mode operation.

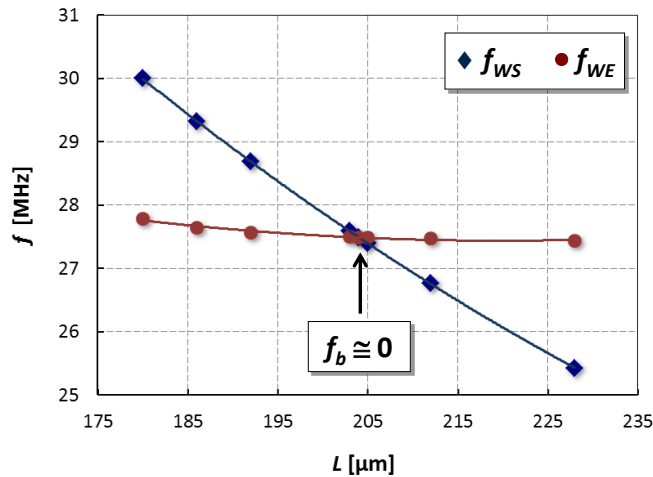


Figure 5.14: Simulated frequency of width-shear (WS) and WE modes vs. L for $W = 156 \mu\text{m}$, corresponding to $f_{WE} = 27 \text{ MHz}$.

phase shift between modes when operated in two-port configuration [74], which effectively isolates one mode from the other in a dual-loop oscillator.

TC_{C11} , TC_{C12} , and TC_{C44} values from [101] were used to model silicon elastic properties in ANSYS to determine WS and WE mode behavior over temperature. $TCf_{WS} = -31.1$ ppm/°C and $TCf_{WE} = -32.5$ ppm/°C were predicted by pre-stressed modal analyses. WS/WE resonators with $f_{WE} = 27$ MHz were designed with f_b ranging from 17 kHz to 1.5 MHz.

Resonators were fabricated on a 20- μ m thick SOI substrate by the process described in chapter 3 and characterized in an ESPEC temperature chamber. The measured frequency response of several devices, obtained with an Agilent E8364B network analyzer, agreed well with simulated f_b values (Figure 5.15). The slightly lower measured TCf_{WS} and TCf_{WE} values (-30.1 ppm/°C and -31.1 ppm/°C) can be attributed to variation in doping concentration (simulations assumed boron-doped silicon with 4 Ω -cm resistivity, while fabricated device resistivity ranged from 1 to 20 Ω -cm). The highest extracted TCf_b was 1480 ppm/°C for a device with $f_b = 17$ kHz (Figure 5.16), nearly 50 \times

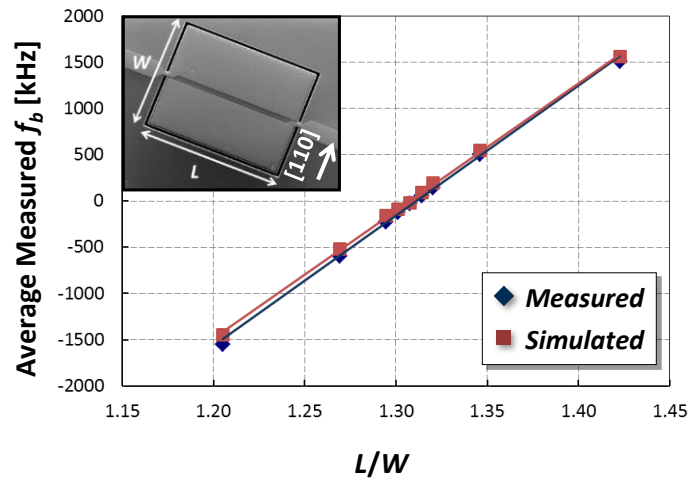


Figure 5.15: Measured vs. simulated f_b for WS/WE resonator designs with $W = 156$ μ m, L varied to modify f_b values ($f_b = f_{WS} - f_{WE}$); (inset) SEM image of WS/WE resonator ($W = 156$ μ m, $L = 204$ μ m).

larger than single-mode measurement of TCf_{WS} or TCf_{WE} . Table 5.1 summarizes measured results for WS/WE resonators.

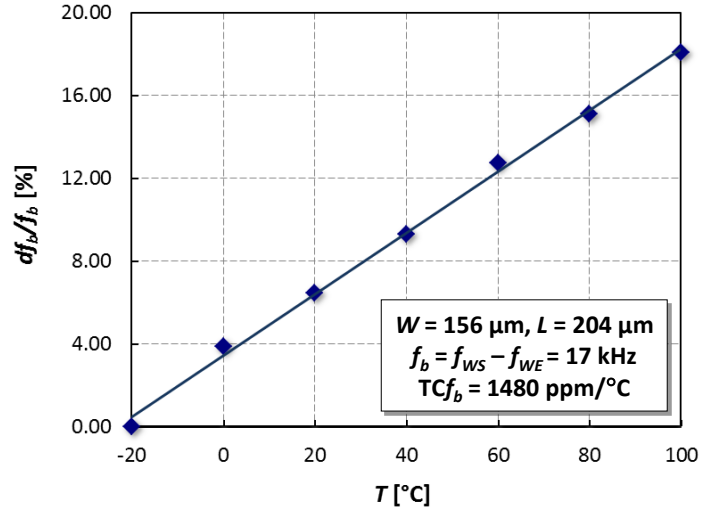


Figure 5.16: Extracted TCf_b of WS/WE DM resonator with $f_b = 17$ kHz; measured $TCf_{WS} = -30.1$ ppm/°C, $TCf_{WE} = -31.1$ ppm/°C.

Table 5.1: Summary of WS/WE mode DM resonator performance.

L [μm]	Q_{WS}	TCf_{WS} [ppm/°C]	Q_{WE}	TCf_{WE} [ppm/°C]	$ f_b $ [kHz]	$ TCf_b $ [ppm/°C]
204	9320	Sim. -31.0	2942	Sim. -32.5	17	1482
205	13864		3128		48	553
206	14803		3805		134	243
210	15428	Meas. -30.1	5492	Meas. -31.1	507	88
222	16173		6448		1531	49

Simulated vs. measured TCf_{WS} and TCf_{WE} , with extracted f_b and TCf_b of fabricated 27-MHz WS/WE resonators ($W = 156$ μm).

WS/WE Mode Oscillator Interfacing

Acoustic coupling between modes as a result of non-linear effects [102] can cause significant Q_{WE} degradation when WS and WE modes converge (Figure 5.17). Since Q affects frequency stability through oscillator phase noise, interference between modes must be minimized. Devices with smaller f_b may benefit from one-port excitation using two single-loop oscillators, which effectively isolates one mode from the other (Figure 5.18b). However, mode isolation is also achievable using a three-terminal configuration with common input and separate output electrodes for f_{WS} and f_{WE} (rather than the current layout shown in Figure 5.18a).

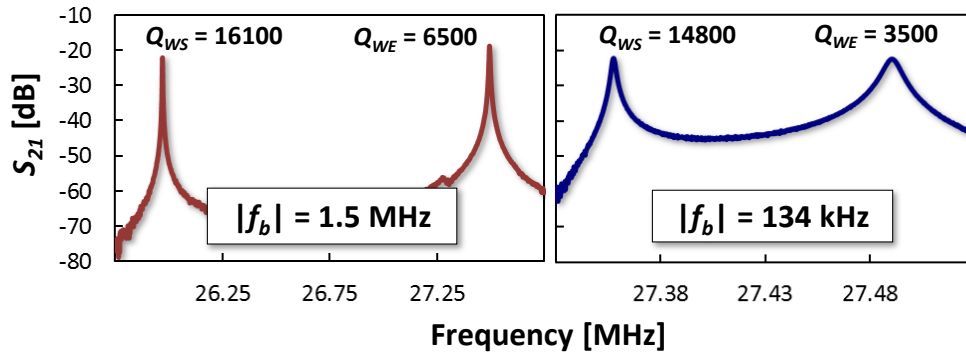


Figure 5.17: Measured response of DM resonators with $|f_b| = 1.5$ MHz and 134 kHz ($|f_b| = |f_{WS} - f_{WE}|$), showing Q_{WE} degradation when f_{WS} and f_{WE} converge.

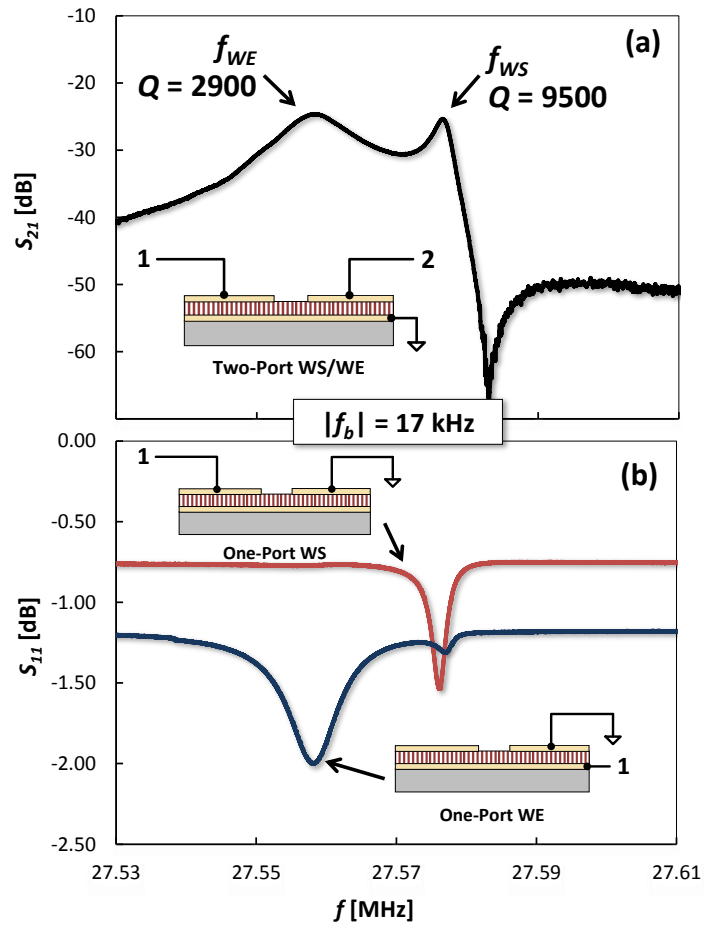


Figure 5.18: WS/WE DM terminal configurations: (a) dual-loop oscillator with two-port operation; (b) two separate one-port oscillators, which provide better isolation of each mode.

5.3.3 EFFECT OF ORIENTATION ON WS/WE RESONATOR TCF

AlN-on-Si WS/WE resonators provide substantial f_b reduction as well as a $2\times$ larger ΔTCF than the WE/WE3 configuration. However, further ΔTCF enhancement would contribute to increased sensitivity as well as relaxed f_b requirements.

Because Young's Modulus (E) in single-crystal silicon is determined by elastic constants c_{ij} and crystal direction, device orientation influences the temperature-frequency behavior of each mode. While WE-mode resonators on (100) substrates have exploited the [100] direction for nearly full compensation for $\text{TC}f_{WE}$ [103], devices in this work are re-oriented to increase WS/WE resonator ΔTCF beyond 1 ppm/ $^{\circ}\text{C}$.

[100]-aligned WS/WE resonators had a simulated $\text{TC}f_{WS} = -30.6$ ppm/ $^{\circ}\text{C}$ and $\text{TC}f_{WE} = -32.7$ ppm/ $^{\circ}\text{C}$ ($\Delta\text{TCF} = 2.1$ ppm/ $^{\circ}\text{C}$). Devices were designed by a similar methodology to [110]-aligned devices, yielding a matched f_b ratio L/W of 1.71. In the [100] direction, $W = 156$ μm corresponds to $f_{WE} = 25$ MHz ($E_{[100]} < E_{[110]}$).

Fabricated devices had a measured $\Delta\text{TCF} = 1.9$, nearly $2\times$ greater than [110]-oriented WS/WE resonators (Figure 5.19). Because f_{WS} is easily driven into nonlinear operation [74], f_{WE} is more likely to be used as a reference and requires lower R_m , which is achieved through increased electrode area by the required L/W ratio (Figure 5.20).

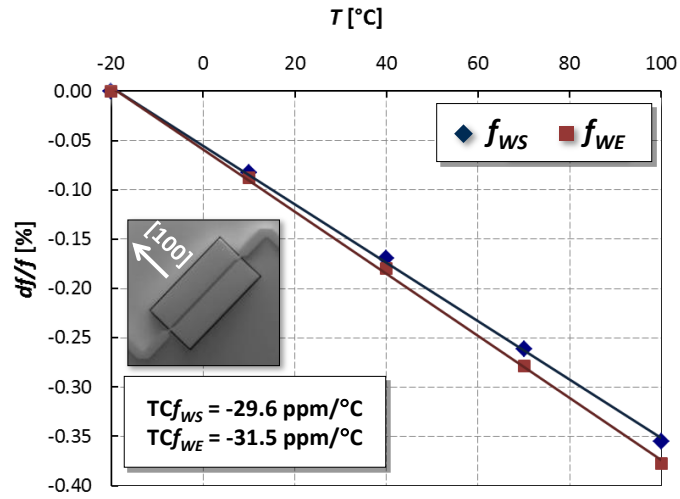


Figure 5.19: Measured TCf_{WS} and TCf_{WE} for [100]-aligned WS/WE resonator, exhibiting 2× larger ΔTCF than [110]-aligned devices; (inset) SEM image of [100]-aligned resonator.

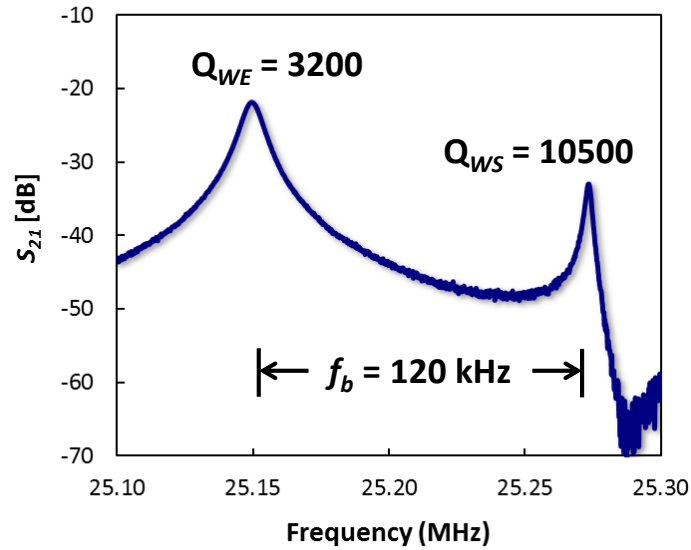


Figure 5.20: Measured response of [100]-oriented WS/WE resonator with $f_b = 120$ kHz ($W = 156$ μm , $L = 268$ μm).

5.3.4 DUAL-MODE EXCITATION FOR TEMPERATURE-STABLE BEAT FREQUENCY

While DM WS/WE mode resonators are applicable to high-sensitivity on-chip thermometry, they can also be employed as temperature-stable references, which are required for counter circuits that would be ultimately used to measure the resonator frequency change with temperature.

Equating the right-hand side of (11) to zero provides the requirements to achieve temperature-insensitive f_b in DM resonators:

$$f_2 = \alpha \cdot f_1 \frac{TCf_1}{TCf_2}. \quad (17)$$

Although $\alpha \cdot f_1$ and f_2 have non-zero TCF, f_b (generated by mixing the two signals) will remain constant over temperature. For a DM resonator with known values of TCf_1 and TCf_2 , $\alpha \cdot f_1$ and f_2 must be designed to satisfy conditions in (17). Because f_{WS} can be modified to a specific ratio of f_{WE} , WS/WE resonators can provide f_b that is either temperature-sensitive or temperature-insensitive.

A [100]-aligned WS/WE resonator with $TCf_{WS} = -29.6$ ppm/°C and $TCf_{WE} = -31.5$ ppm/°C requires f_{WS} to equal $(1.06) \cdot f_{WE}$. A 25-MHz device fulfilling the aforementioned condition ($f_{WS} = 26.8$ MHz, $f_{WE} = 25.3$ MHz) was fabricated and characterized over temperature (Figure 5.21). The extracted $TC^1 f_b$ of 2.4 ppm/°C and $TC^2 f_b$ of 3.3 ppb/°C² correspond to a frequency drift of 266 ppm from -20°C to 100°C (Figure 5.22), which is lower than degenerately-doped resonators [104] or geometrically-engineered capacitive resonators [105].

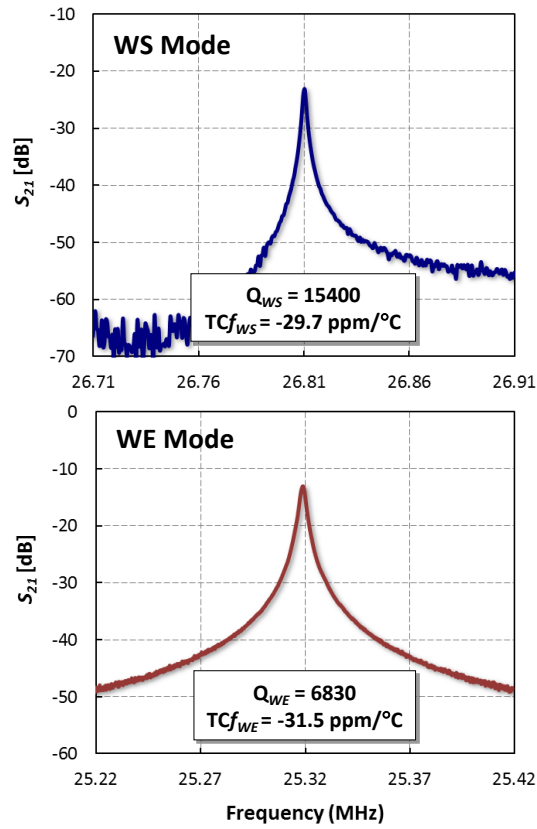


Figure 5.21: Measured response for f_{WS} and f_{WE} of [100]-aligned resonator with $f_b = 1.5 \text{ MHz}$ and near-zero TCf_b ($W = 156 \text{ }\mu\text{m}$, $L = 242 \text{ }\mu\text{m}$).

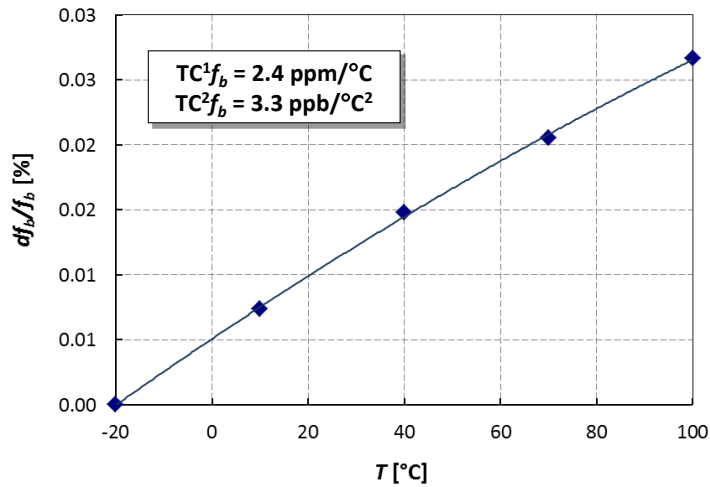


Figure 5.22: Extracted TCf_b of [100]-aligned WS/WE DM resonator with nearly temperature-stable f_b .

6 TOWARDS INTEGRATED MICROMECHANICAL KINETIC ENERGY HARVESTING

Readily-available low-frequency mechanical energy, such as human walking at 1-2 Hz [106] and other common vibration sources up to 150 Hz [107], can be collected and transformed into useful electric power. However, because kinetic energy harvesting (KEH) devices require large mass to operate at low frequencies, it is challenging to miniaturize such devices without increasing the operation frequency. For example, piezoelectric cantilever harvesters can generate sufficient power to operate wireless temperature sensors [108], but maximum power is only achievable at the device resonance frequency in hundreds of Hz or greater (Figure 6.1a). Thus, lower-frequency vibrations cannot be converted with the same efficiency.

6.1 MULTI-DEGREE-OF-FREEDOM ENERGY HARVESTING

Although environmental vibrations occur across multiple degrees of freedom (multi-DOF), most energy harvesters operate as a single-DOF mass-spring system [109]. To provide power regardless of device orientation with respect to the vibration source, typical devices must be duplicated and oriented along different axes, further increasing system size and complicates integration. A multi-axis device eliminates the need to manually align the harvester for maximum power. Realizing micromachined out-of-plane and in-plane harvesters on the same die is the first step towards achieving this goal.

6.2 MECHANICAL FREQUENCY UPCONVERSION

As electromechanical transducer resonance frequency increases, higher power levels can be captured for constant input vibration amplitudes [109]. However, the

amount of useful ambient energy decreases at higher frequencies. Mechanical frequency upconversion has been explored as a method to combine low-frequency ambient energy scavenging with resonant MEMS devices. Recently reported harvesters utilize an inertial mass that collects environmental energy in a wide frequency range and actuates high-frequency transducers to increase the power output (Figure 6.1b) [110, 111]. However, the overall volume, including external magnets, is in hundreds of mm³ or larger.

6.3 ALN-ON-SI MEMS KINETIC ENERGY HARVESTERS

Devices with integrated upconverting transducers are designed to enhance power output while maintaining a small footprint, multi-axis KEH (Figure 6.2). Low-frequency in-plane and out-of-plane vibrations are harvested and upconverted to higher frequencies without post-process assembly or large external transducers.

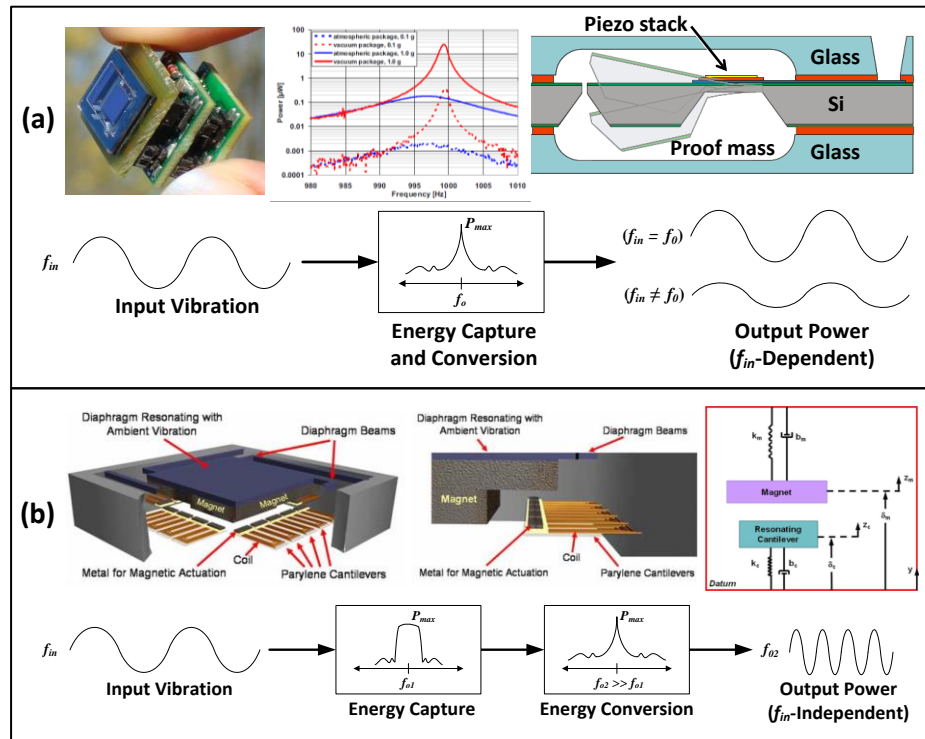


Figure 6.1: Schematic diagrams depicting conversion mechanism in previously reported MEMS resonant kinetic energy harvesters: (a) without mechanical frequency upconversion [112]; (b) with mechanical frequency upconversion [113].

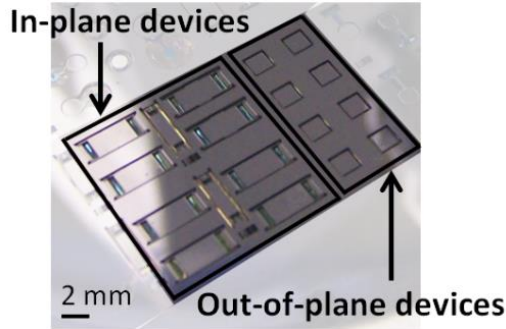


Figure 6.2: Backside view of a silicon die with in-plane and out-of-plane kinetic energy harvesters fabricated side-by-side.

6.3.1 OUT-OF-PLANE ENERGY HARVESTER

The out-of-plane harvester comprises a seismic mass tethered to the substrate with integrated AlN-on-Si beam transducers. The mass captures low-frequency ambient vibrations in an out-of-plane translational mode (Figure 6.3, top). Additionally, the mass motion couples energy into the transducer high-frequency fundamental clamped-clamped beam mode (Figure 6.3, bottom). To sense a high-strain region of the beam deflection, where the most charge is generated by the piezoelectric effect, transducer electrodes and AlN cover the area near the substrate anchor point.

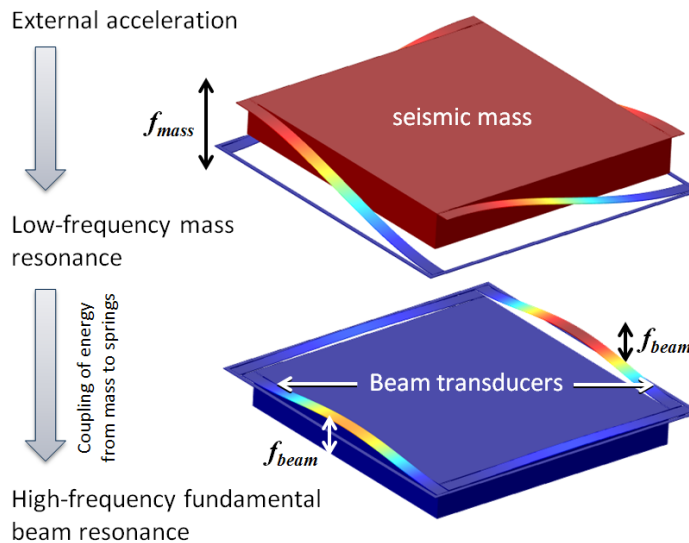


Figure 6.3: Out-of-plane harvester mode shapes ($f_{mass} = 149$ Hz and $f_{beam} = 13.7$ kHz) and basic principle of operation.

6.3.2 IN-PLANE ENERGY HARVESTER

Rather than orienting out-of-plane harvesters to detect in-plane vibrations, a second integrated design is presented. The in-plane KEH device consists of a seismic mass with free-standing cantilever micro-picks (μ -picks) located in the center of the mass (Figure 6.4a). The mass exhibits translational motion in response to low-frequency vibrations (Figure 6.4b). When external acceleration generates sufficient force, each μ -pick “snaps” an AlN-on-Si spring transducer that subsequently vibrates at higher frequencies (Figure 6.4c). The spring transducer top electrode connects regions of identical strain polarity to collect charge when kHz in-plane modes are excited by the μ -picks (Figure 6.5).

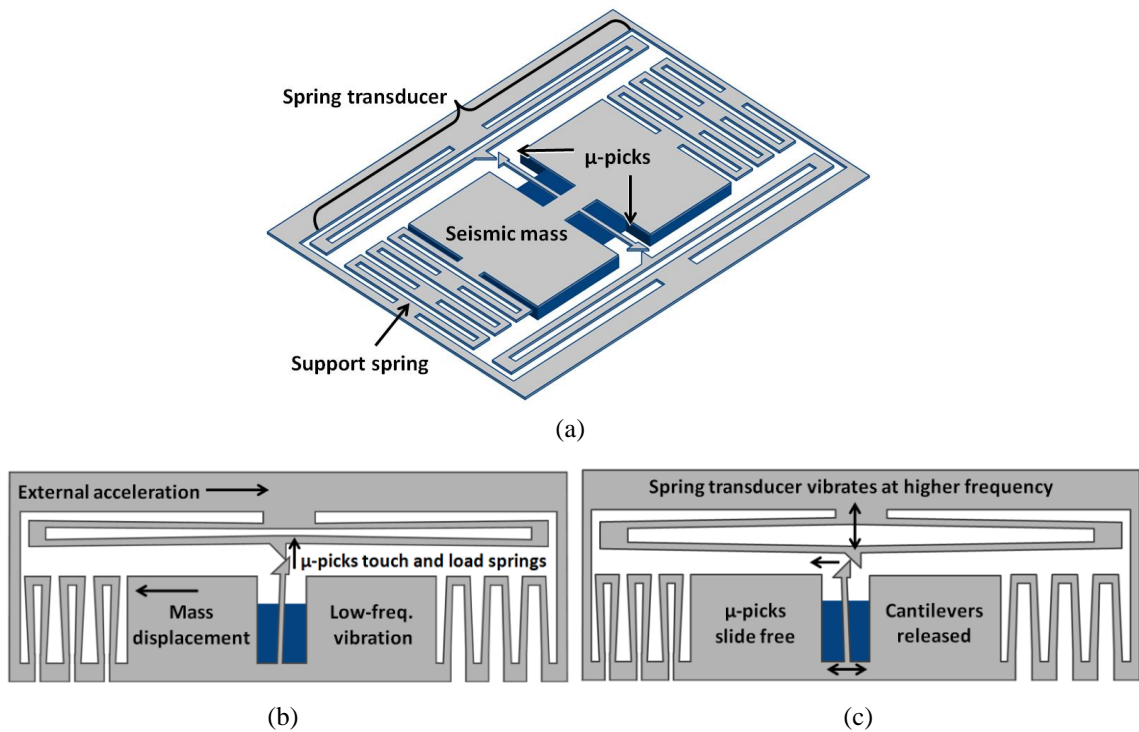


Figure 6.4: Conceptual diagram of in-plane harvester: (a) rest position, (b) side view of low-frequency seismic mass vibration, (c) side view of high-frequency spring transducer vibration.

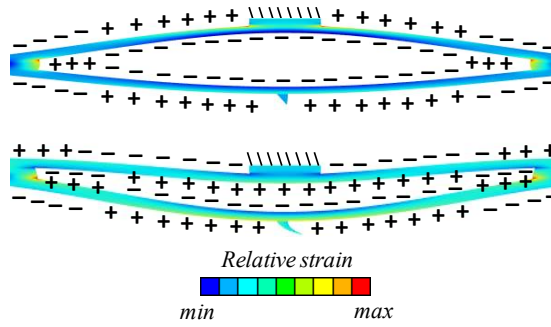


Figure 6.5: Spring transducer strain patterns showing charge formation for in-plane modes at 2.23 kHz (upper) and 6.24 kHz (lower).

6.4 FABRICATION PROCESS INTEGRATION

The TPoS fabrication process lends itself well to realizing low-frequency energy harvesting devices (10 – 100s of Hz) and high-frequency resonators on the same substrate. AlN-on-Si KEH devices were fabricated a 5- μm device SOI wafer using the process described in section 3.2.3, with minor modifications to provide the necessary mass for low-frequency operation and the capability for in-plane vibration harvesting (Figure 6.6). First, rather than completely remove the handle Si, the backside oxide mask was used to create the seismic mass, connected to the device layer through the buried oxide. Immediately after backside cavity patterning, an additional mask layer was used to selectively etch the backside oxide and control seismic mass thickness, which enables any number of devices on the same wafer to be customized for a particular operating frequency or power requirement. Secondly, topside HF release formed z -shock stops to ensure that in-plane harvesters maintain μ -pick alignment (Figure 6.7). Immediately following HF release, devices were placed in a supercritical dryer to prevent shock stops from adhering to the handle layer through stiction forces.

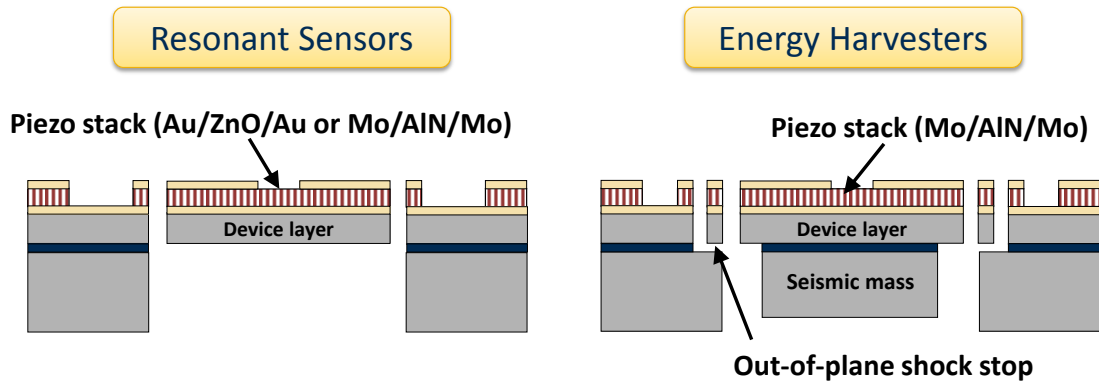


Figure 6.6: Cross-section view of TPoS sensors and energy harvesters on SOI substrate.

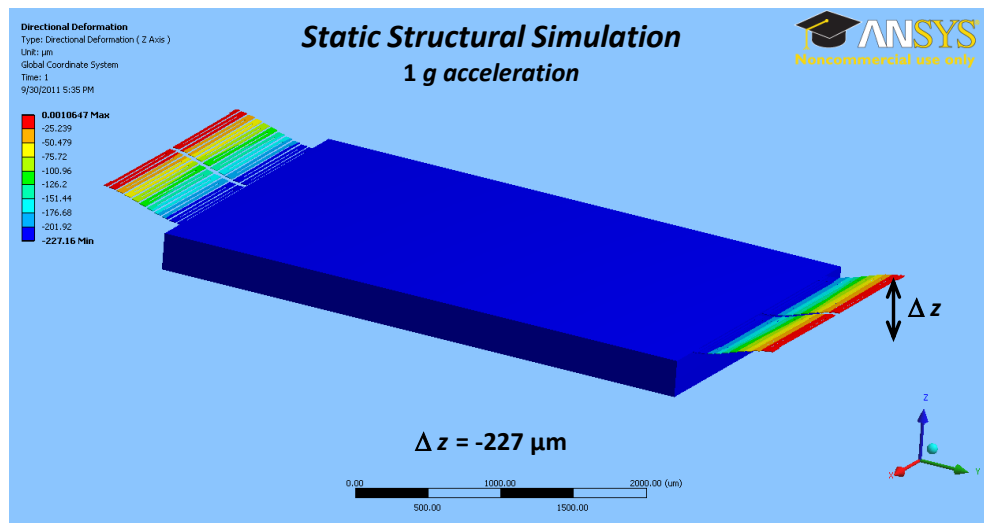


Figure 6.7: Static structural simulation showing 260- μm thick seismic mass deflection resulting from 1g gravitational acceleration, demonstrating the need for shock stops to maintain in-plane alignment with μ -picks.

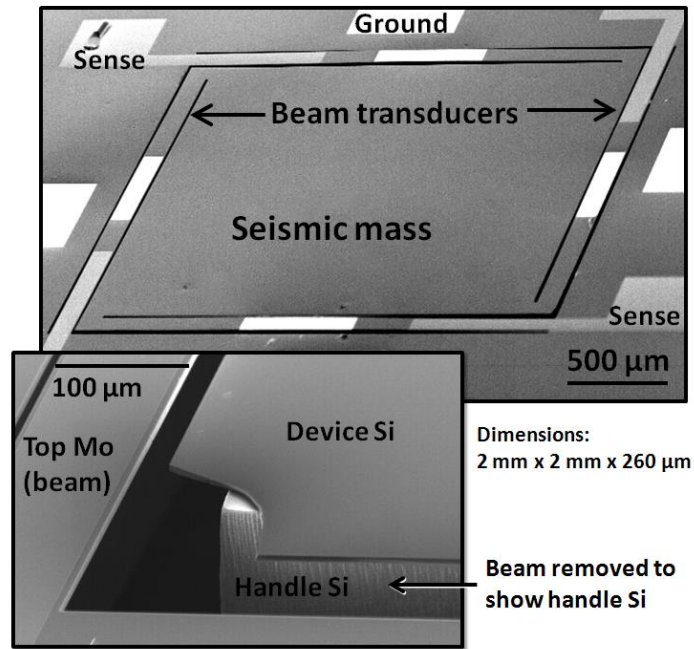


Figure 6.8: SEM images of out-of-plane harvester. AlN and top Mo are patterned to sense the fundamental clamped-clamped beam mode, exposing bottom Mo in the beam center.

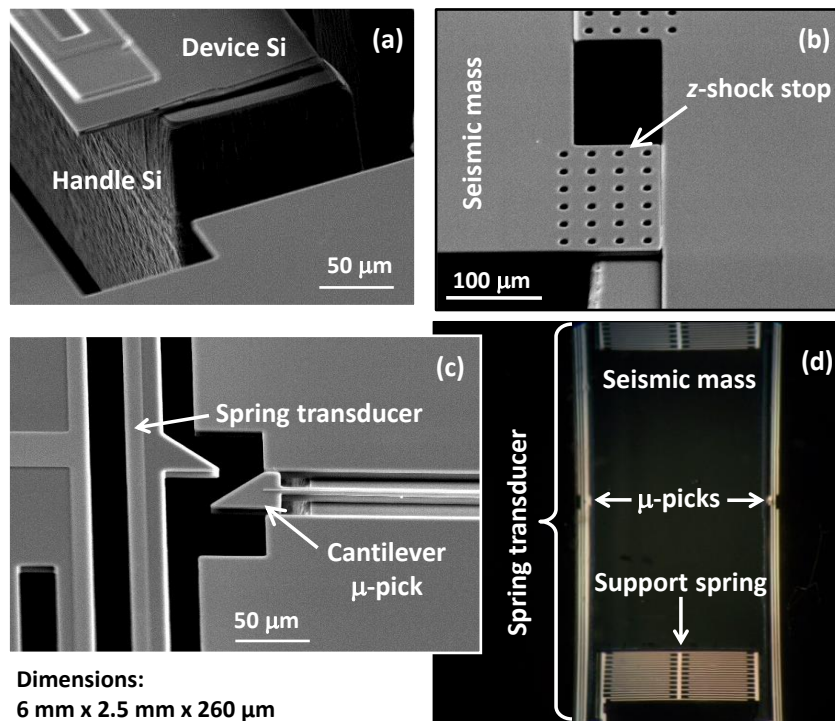


Figure 6.9: (a) SEM image of in-plane harvester z-shock stop removed to show seismic mass formed by handle Si; (b) SEM image of intact shock stop resting on handle Si (anchored to substrate); (c) SEM image of μ -picks and spring transducer; (d) backside optical view of entire device.

6.5 KEH DEVICE CHARACTERIZATION

Devices were mounted on a stage that provides sinusoidal out-of-plane or in-plane acceleration a_{in} with frequency f_{in} (Figure 6.10). All four beam transducer outputs from the out-of-plane devices were wirebonded and connected in parallel while a single spring transducer output from the in-plane device was connected for testing (Figure 6.11). Output current was fed through a load resistance R_L to a transimpedance amplifier (TIA). The TIA output voltage, which is proportional to the converted current, was measured by an oscilloscope.

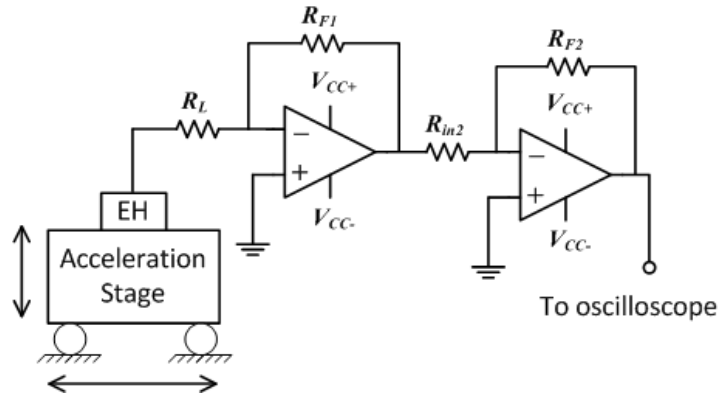


Figure 6.10: Schematic of KEH device measurement setup for out-of-plane harvesters and in-plane harvesters. A vertical shaker table (MB Dynamics, Inc.) was used for out-of-plane testing while an accelerometer setup (built in-house by former colleagues) was utilized for in-plane testing.

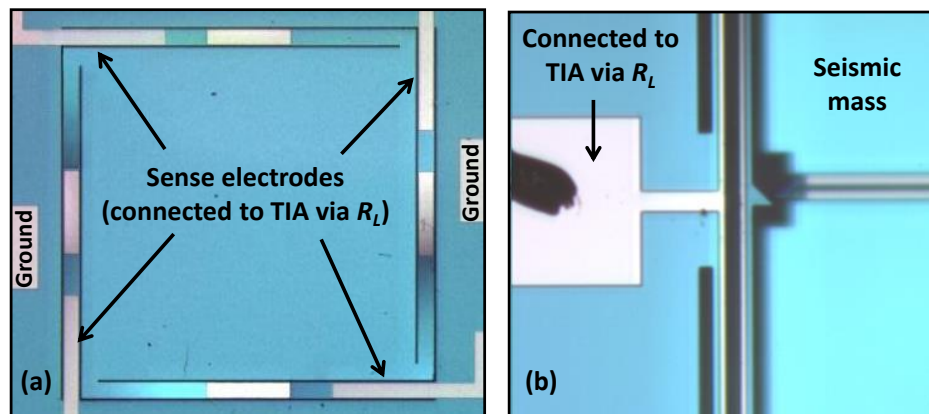


Figure 6.11: Optical images indicating electrical connections made to testing setup: (a) all top electrodes of the out-of-plane harvester were wirebonded for testing; (b) a single spring transducer of the in-plane harvester was connected.

6.5.1 OUT-OF-PLANE ENERGY HARVESTER

The out-of-plane harvester was first characterized over various accelerations at an input frequency close to the seismic mass resonance. A sinusoidal output signal $f_{out} = f_{in} = 126$ Hz was generated by the harvester, while increasing a_{in} produced large transient current spikes occurring with frequency f_{spike} in addition to the sinusoidal signal. When a_{in} was increased to $0.7g$, f_{spike} also became equal to f_{in} (Figure 6.12).

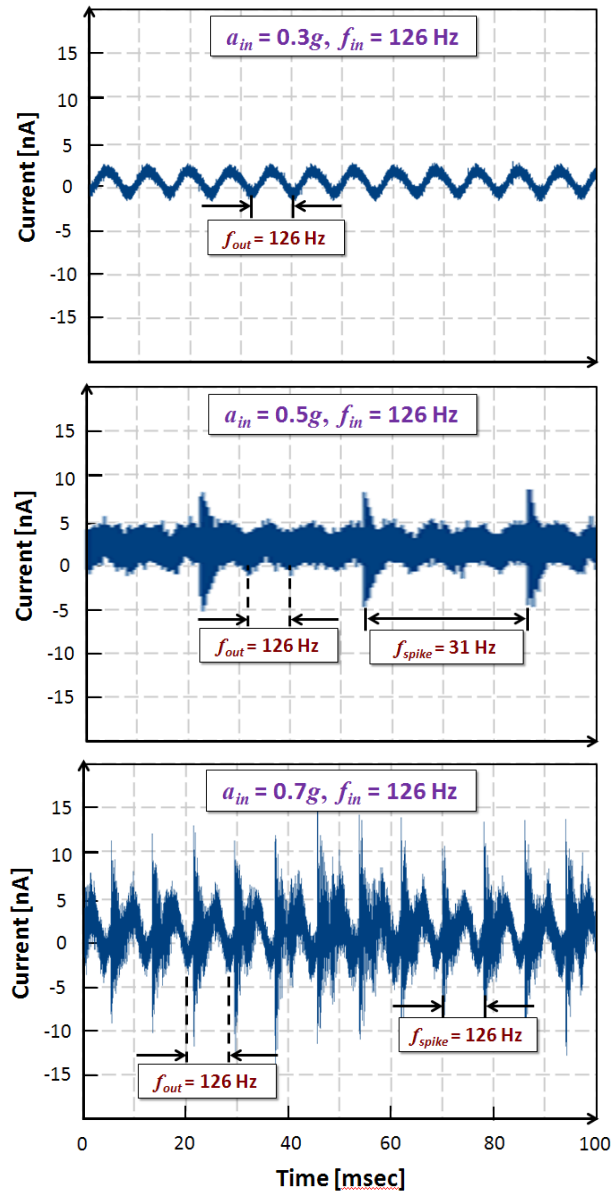


Figure 6.12: Out-of-plane beam transducer output at $a_{in} = 0.3$ g, $a_{in} = 0.5$ g, and $a_{in} = 0.7$ g.

The output current impulses were found to have a main spectral component at f_{ring} 12 kHz (Figure 6.13), which corresponds to the fundamental beam mode. A peak power of 3.23 nW was measured in response to a 134-Hz, 0.6g acceleration input.

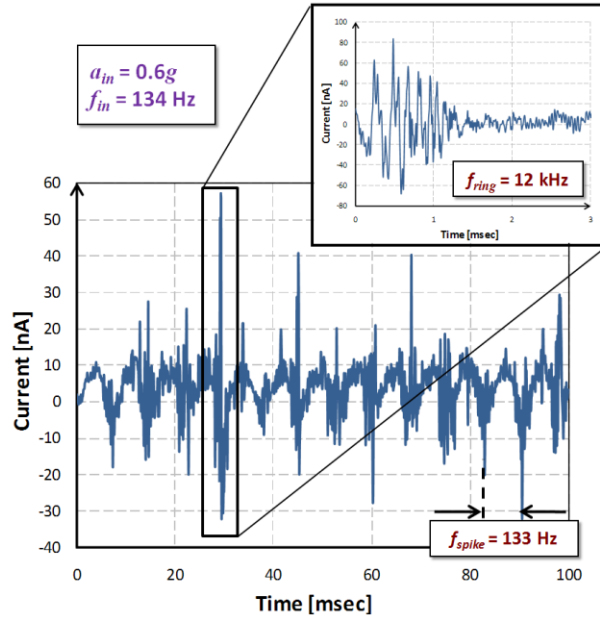


Figure 6.13: Out-of-plane beam transducer output with periodic upconversion spikes; (inset) close-up view of signal ring-down with 12kHz spectral component.

6.5.2 IN-PLANE ENERGY HARVESTER

Similar acceleration characterization was performed for the in-plane harvester at lower frequencies (Figure 6.14). Limitations of the test setup caused frequency to change slightly with acceleration amplitude. Preliminary measurements showed that a minimum acceleration of 0.45g was required to induce periodic actuations of the spring transducer with an f_{spike} equal to f_{in} . Missed actuations may result from imperfect μ -pick alignment due to slight tilting of the sample.

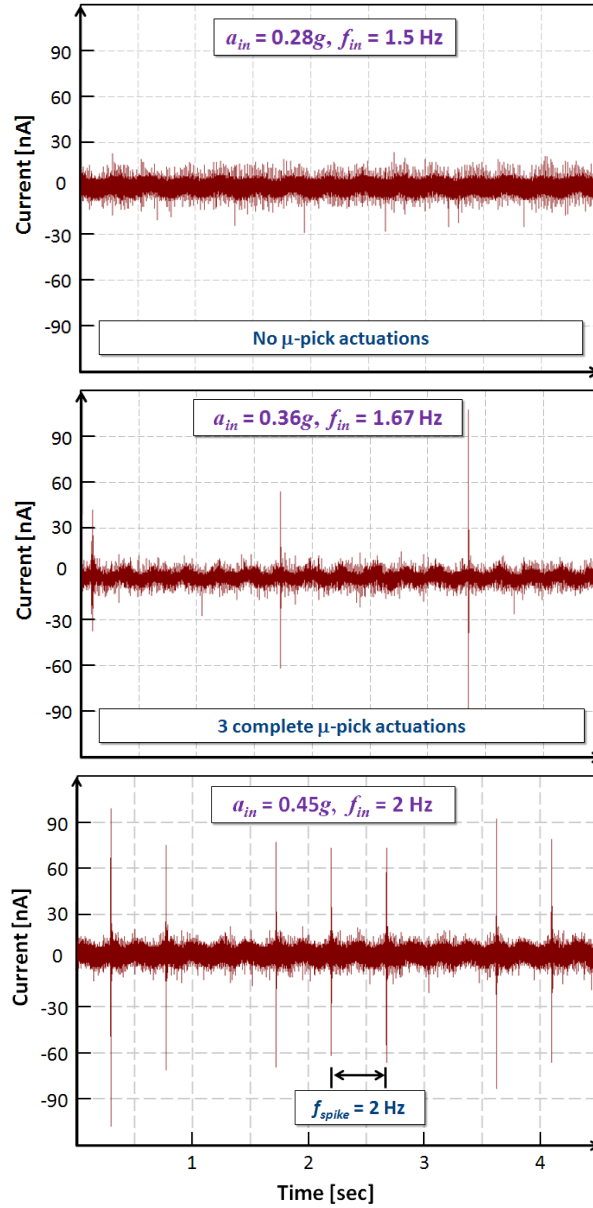


Figure 6.14: In-plane spring transducer output at various accelerations ($R_L = 560 \Omega$).

For $a_{in} = 0.45g$ and $f_{in} = 2$ Hz, complete actuations of one in-plane spring transducer occurred with $f_{spike} = f_{in}$. A single upconversion spike produced a peak power of 2.27 nW (Figure 6.15). Spectral analysis confirmed signal components at $f_{ring} = 2$ kHz and 7 kHz contained in the upconversion spikes, which are in close agreement with simulated spring modes.

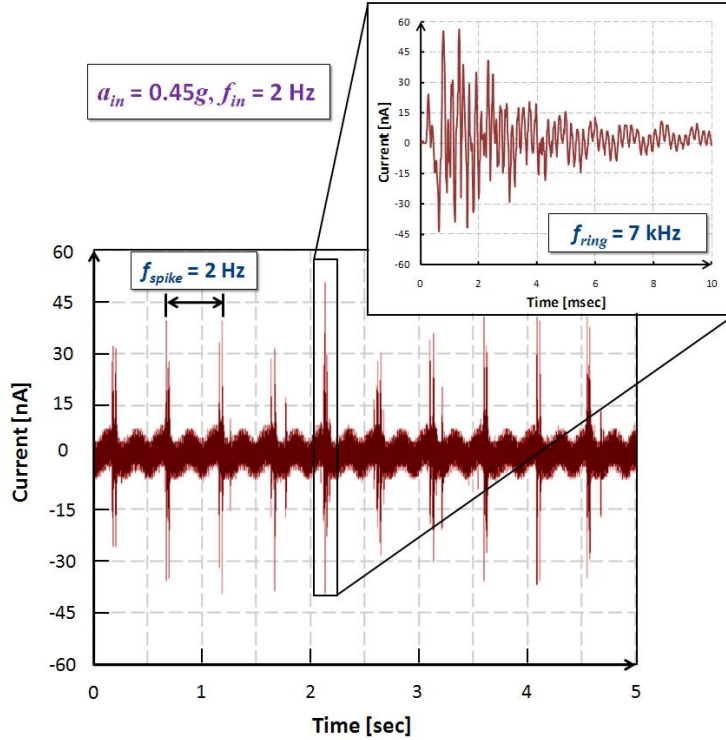


Figure 6.15: In-plane spring transducer output with upconversion spikes ($R_L = 560 \text{ k}\Omega$); (inset) close-up view of 7 kHz signal ring-down.

While testing limitations prevented simultaneous measurement of both spring transducers, the total output current should nearly double as a result of the transducer symmetry [111]. The cantilever transducers on the seismic mass, which are also covered with piezoelectric material, can be measured in conjunction with the spring transducer output to maximize power output harvested from the KEH device.

Power calculations were based on the measured output current and R_L . While $R_L = 560 \text{ }\Omega$ was used for in-plane acceleration characterization, measurements with R_L values up to $560 \text{ k}\Omega$ (Figure 6.16) confirmed that the output power can be maximized by selecting R_L to approach the source impedance of the harvester.

This work introduced micromachined multi-axis AlN-on-Si KEHs as a solution to scavenge low-frequency mechanical energy from the environment. Both out-of-plane and

in-plane devices utilized integrated frequency upconversion transducers that increased the power output beyond the already-harvested energy at the tested input frequencies.

The fabrication process accommodates for multiple degrees-of-freedom by incorporating out-of-plane and in-plane harvesters on the same substrate. Additionally, the fabrication process allows for multiple operating frequencies and increased power output by controlling the seismic mass thickness.

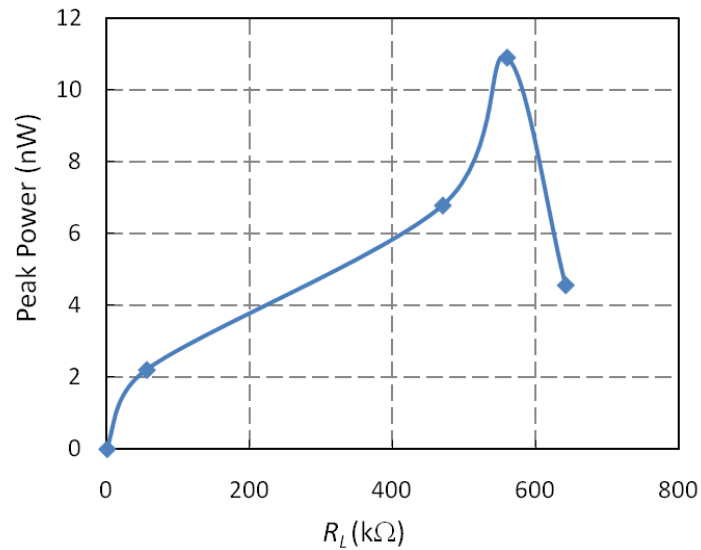


Figure 6.16: Measured peak power vs. R_L for in-plane harvester.

7 CONCLUSIONS AND FUTURE DIRECTIONS

This dissertation presented a MEMS-based environmental monitoring platform comprising TPoS gravimetric resonators and kinetic energy harvesters. Resonators with annexed platforms were shown to be suitable candidates for portable integrated gas sensing as pure mass sensors that can be further optimized for high performance and low-power operation.

7.1 TECHNICAL CONTRIBUTIONS

- I. Silicon BAW resonators with annexed platforms for gravimetric sensing
 - A. Optimization and characterization of TPoS gravimetric resonators: the enabling device of the TPoS micro-platform was designed for high Q and low R_m with optimized sensing mode excitation and spurious mode suppression, which are essential for low-power oscillator interfacing and sensor readout. The annexed platform design enables the sensor to maintain high Q upon mass loading.
 - B. TPoS resonators for RH&T sensing: ZnO-on-Si resonators were designed, fabricated, and selectively functionalized for gravimetric relative humidity measurement. The RH sensor response was thermally corrected using an identical, uncoated resonator to measure temperature, enabling this functionality to be easily realized in an array configuration where devices are fabricated side-by-side. However, dual-mode temperature sensing can eventually be applied to integrated RH&T sensing with a single device.
 - C. TPoS resonators for VOC sensing: AlN-on-Si sensors were functionalized for toluene and xylene detection, maintaining high Q during exposure. Humidity and

temperature effects on sensor response were also studied, confirming the need for integrated RH&T sensing to calibrate the VOC sensor response.

II. TPoS resonators for dual-mode temperature measurement

A. Simultaneous dual-mode oscillator for self-temperature sensing: the first silicon-based DM oscillator for self-temperature sensing was demonstrated using ZnO-on-Si BAW resonators. The differing TCFs of two modes were exploited to accurately and locally measure device temperature with a 4× greater temperature sensitivity than single-mode measurement. The effects of simultaneous excitation on oscillator phase noise were also characterized and determined to be a strong function of the minimum Q of the two modes.

B. TPoS resonators for enhanced dual-mode temperature sensing: AlN-on-Si resonators exploiting alternative resonance modes for DM operation achieved reduced beat frequency through geometry engineering and increased Δ TCF through device orientation. For reduced- f_b DM resonators based on width-shear and width-extensional modes, nearly 50× greater temperature sensitivity was achieved compared to using fundamental and third-order width-extensional modes for DM operation.

III. TPoS kinetic energy harvesting devices

A. Multi-axis AlN-on-Si kinetic energy harvesters: devices with fully-integrated upconverting transducers were fabricated by a process that is fully compatible with TPoS resonators and sensors. Out-of-plane and in-plane vibrations were captured by devices with transducers operating in the kHz range, producing peak output power in the nW range.

7.2 FUTURE WORK

While exciting progress has been made towards the goal of a miniaturized multi-sensing platform, various challenges remain for future investigation.

7.2.1 WAFER-LEVEL SENSOR FUNCTIONALIZATION AND OPTIMIZATION

The Nano eNabler proved to be a useful tool for polymer printing and sensor characterization. However, the TPoS platform should ultimately be compatible with batch micromachining processes such as lithographic patterning and stamping. A hybrid serial/parallel approach would provide the benefits of selective patterning while expediting functionalization and achieving better repeatability and uniformity.

Further material characterization is also required to improve sensor performance as well as provide optimal, repeatable functional layers regardless of processing technique. While top-down patterning has been used to functionalize sensors with non-traditional materials, bottom-up techniques have been successfully used in recent years [81]. Thus, a combination of material types could provide unprecedented selectivity and sensitivity improvements.

7.2.2 WAFER-LEVEL PACKAGING FOR TPoS MICRO-PLATFORM

Although TPoS resonant sensors are capable of high- Q operation without vacuum encapsulation, any micro-sensor requires minimal protection from the environment to ensure that dust or other large particles do not interfere with long-term operation. Wafer-level polymer packaging is a low-cost option that can be made compatible with the TPoS process [114]. Of course, sensor performance under packaged conditions should also be taken into consideration.

7.2.3 ENERGY HARVESTER RELIABILITY AND PERFORMANCE OPTIMIZATION

The proof-of-concept KEH devices presented in this thesis demonstrated that the TPoS platform can be successfully applied to other devices of importance to portable and wireless systems. However, further understanding is required to address scaling limits and implementation challenges.

Materials and Methods for Improved Reliability

Long-term tests were not conducted on μ -pick reliability, but repeated stress on moving parts is expected to contribute to wear and eventual device, especially in-plane devices (Figure 7.1). One option is to use sputtering or atomic layer deposition (ALD) to coat frictional surfaces with materials such as hafnium diboride and titanium nitride, which have been shown to protect surfaces.

While thicker device layer substrates would improve robustness of the transducer springs, the increased operating frequency must be considered in the design phase. A different structural material, rather than increased dimensions and features of current TPoS devices, could provide the compliance needed for lower frequency harvesting.

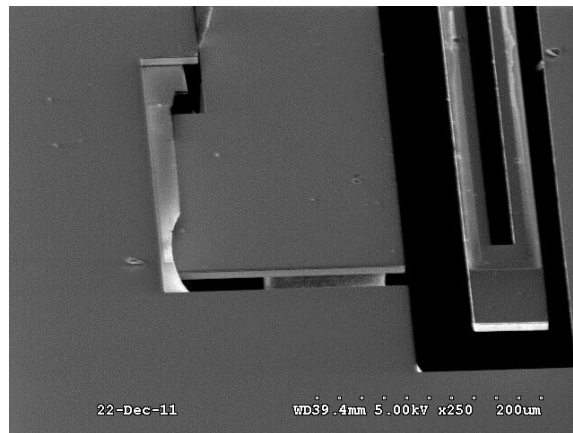


Figure 7.1: SEM image of in-plane harvester with mis-aligned shock stop.

To Upconvert or Not To Upconvert?

The difference between harvested power from low-frequency vs. upconverted frequency must be thoroughly investigated. Because the maximum harvestable input power from the seismic mass is larger than that of the spring or beam transducers (based on volume), it is important to determine exactly how much benefit, if any, upconversion provides in regards to power enhancement.

7.2.4 ENERGY HARVESTER IMPLEMENTATION AND INTERFACING

Single-Device Multi-Axis Energy Harvesters

Although devices presented in this thesis were optimized for single-axis energy harvesting, multi-axis kinetic energy scavenging capabilities would be highly beneficial for applications where die real estate is crucial. Integrated multi-DOF designs would be a great contribution to the TPoS micro-platform.

Energy Harvester Signal Conditioning Circuitry

In practical implementation, the MEMS device is only part of an entire energy harvesting system (Figure 7.2). Successful energy extraction requires appropriate signal conditioning and rectification circuitry as well as on-chip storage, such as supercapacitors or micro-batteries. While device and electronics integration are facilitated by the TPoS platform, system architectures dependent on the transduction mechanism must be considered to maximize deliverable energy to wireless and autonomous sensor nodes.

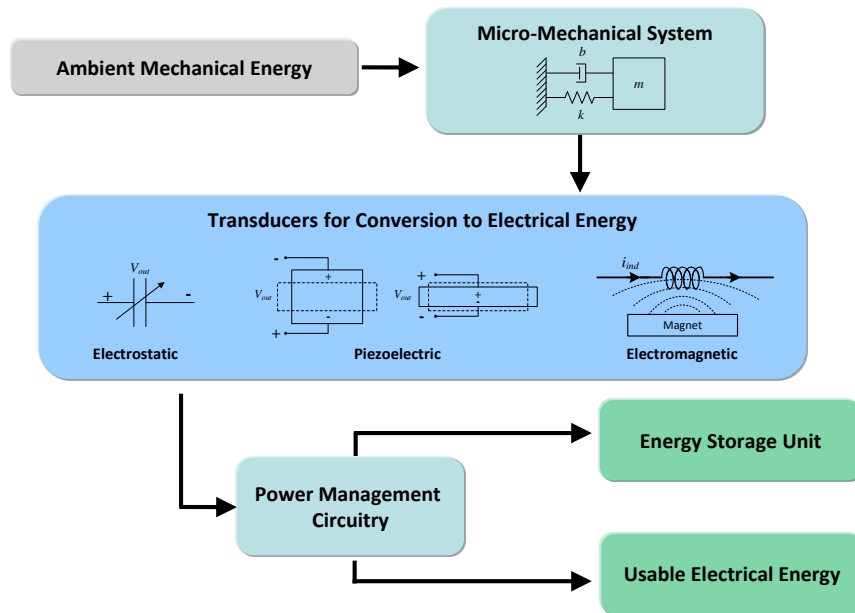


Figure 7.2: Schematic diagram of a MEMS energy harvesting system describing the process of harvesting ambient mechanical energy with a micro-mechanical system, converting it to usable electrical energy by various transduction mechanisms, and processing it for storage and eventual delivery.

REFERENCES

- [1] D. S. Ballantine, R. M. White, S. J. Martin, A. J. Ricco, G. C. Frye, E. T. Zellars, and H. Wohltjen, *Acoustic Wave Sensors - Theory, Design, and Physico-Chemical Applications*: Elsevier, 1997.
- [2] S. M. Sze, *Semiconductor sensors*: Wiley New York, 1994.
- [3] J. C. Eloy, "MEMS Industry Evolution: From Devices to Function," Yole Développement, 2010.
- [4] M. Gikas, "Samsung Galaxy S4 performance is top-notch," Consumer Reports, 2013.
- [5] M. A. Ryan, K. S. Manatt, S. Gluck, A. V. Shevade, A. K. Kisor, H. Zhou, L. M. Lara, and M. L. Homer, "The JPL Electronic Nose: Monitoring Air in the US Lab on the International Space Station," in *IEEE Sensors J.*, 2010, pp. 1242 - 1247.
- [6] F. Röck, N. Barsan, and U. Weimar, "Electronic Nose: Current Status and Future Trends," *Chemical Reviews*, vol. 108, pp. 705-725, 2008.
- [7] (2012). *What Are the Six Common Air Pollutants?* Available: <http://epa.gov/air/urbanair/>
- [8] L. A. Wallace, "Project Summary: The Total Exposure Assessment Methodology (TEAM) Study," U.S. EPA, 1987.
- [9] P. Ciccioli, A. Cecinato, E. Brancaleoni, A. Brachetti, and M. Frattoni, "Polar volatile organic compounds (VOC) of natural origin as precursors of ozone," *Environ Monit Assess*, vol. 31, pp. 211-217, 1994/05/01 1994.
- [10] J. Barlow. "Rising Ozone Levels Pose Challenge to U.S. Soybean Production, Scientists Say," 2003. Available: earthobservatory.nasa.gov/Newsroom/view.php?id=23565
- [11] "Beyond CO2: Sensing VOCs in Indoor Air Protects Health, Saves Energy," AppliedSensor, Inc., 2009.
- [12] G. Peng, U. Tisch, O. Adams, M. Hakim, N. Shehada, Y. Y. Broza, S. Billan, R. Abdah-Bortnyak, A. Kuten, and H. Haick, "Diagnosing lung cancer in exhaled breath using gold nanoparticles," *Nat Nano*, vol. 4, pp. 669-673, 2009.
- [13] (June 2003). *General Information for TGS Sensors*. Available: <http://www.figarosensor.com/products/general.pdf>
- [14] (2009). *ESRL Global Monitoring Division - Education and Outreach*. Available: http://www.esrl.noaa.gov/gmd/infodata/faq_cat-3.html
- [15] R. Biswas, C. G. Ding, I. Puscasu, M. Pralle, M. McNeal, J. Daly, A. Greenwald, and E. Johnson, "Theory of subwavelength hole arrays coupled with photonic crystals for extraordinary thermal emission," *Phys. Rev. B*, vol. 74, 2006.
- [16] D. E. Pierce, Y. Kim, and J. R. Vig, "A temperature insensitive quartz microbalance," *IEEE Trans. Ultrason. Ferroelect. Freq. Control*, vol. 45, pp. 1238-1245, 1998.

- [17] W. H. King, "Piezoelectric Sorption Detector," *Anal. Chem.*, vol. 36, pp. 1735-1739, 1964.
- [18] G. K. Ho, "Design and characterization of silicon micromechanical resonators," Ph.D., Georgia Institute of Technology, 2008.
- [19] J. T. M. van Beek, K. L. Phan, G. J. A. M. Verheijden, G. E. J. Koops, C. van der Avoort, J. van Wingerden, D. E. Badaroglu, J. J. M. Bontemps, and R. Puers, "A piezo-resistive resonant MEMS amplifier," in *Electron Devices Meeting, 2008. IEDM 2008. IEEE International*, 2008, pp. 1-4.
- [20] B. Cagdaser and B. E. Boser, "Resonant drive: sense and high voltage electrostatic drive using single MEMS capacitor and low voltage electronics," in *Micro Electro Mechanical Systems, 2005. MEMS 2005. 18th IEEE International Conference on*, 2005, pp. 142-146.
- [21] S. Pourkamali, "High frequency capacitive single crystal silicon resonators and coupled resonator systems," Ph.D., Georgia Institute of Technology, 2006.
- [22] A. K. Samaroo, G. Casinovi, and F. Ayazi, "Passive TCF Compensation in High Q Silicon Micromechanical Resonators," in *IEEE International Conference on Micro Electro Mechanical Systems (MEMS)*, 2010, pp. 116-119.
- [23] A. Rahafrooz, A. Hajjam, B. Tousifar, and S. Pourkamali, "Thermal actuation, a suitable mechanism for high frequency electromechanical resonators," in *Micro Electro Mechanical Systems (MEMS), 2010 IEEE 23rd International Conference on*, 2010, pp. 200-203.
- [24] A. Hajjam, A. Rahafrooz, J. C. Wilson, and S. Pourkamali, "Thermally actuated MEMS resonant sensors for mass measurement of micro/nanoscale aerosol particles," in *Sensors, 2009 IEEE*, 2009, pp. 707-710.
- [25] R. Abdolvand, "Thin-film piezoelectric-on-substrate resonators and narrowband filters," Ph.D., Georgia Institute of Technology, 2008.
- [26] R. Abdolvand, Z. Hao, and F. Ayazi, "A Temperature-Compensated ZnO-on-Diamond Resonant Mass Sensor," in *IEEE Sensors Conference*, 2006, pp. 1297-1300.
- [27] J. Alder and J. McCallum, "Piezoelectric crystals for mass and chemical measurements," *Analyst(London. 1877. Print)*, vol. 108, pp. 1169-1189, 1983.
- [28] Z. Ying, Y. Jiang, X. Du, G. Xie, J. Yu, and H. Wang, "PVDF coated quartz crystal microbalance sensor for DMMP vapor detection," *Sens. Actuators, B*, vol. 125, pp. 167-172, 2007.
- [29] C. K. O'Sullivan and G. G. Guilbault, "Commercial quartz crystal microbalances - theory and applications," *Biosensors and Bioelectronics*, vol. 14, pp. 663-670, 1999.
- [30] H. Kawai, "The Piezoelectricity of Poly (vinylidene Fluoride)," *Jpn. J. Appl. Phys.*, vol. 8, pp. 975-976, 1969.
- [31] Y. B. Jeon, R. Sood, J. h. Jeong, and S. G. Kim, "MEMS power generator with transverse mode thin film PZT," *Sens. Actuators, A*, vol. 122, pp. 16-22, 2005.

- [32] S. Bathurst, H. W. Lee, and S. G. Kim, "Direct printing of lead zirconate titanate thin films for microelectromechanical systems," 2008, pp. 391-394.
- [33] K. Hashimoto, *RF Bulk acoustic wave filters for communications*: Artech House Publishers, 2009.
- [34] H. Campanella, "Localized-mass detection based on thin-film bulk acoustic wave resonators (FBAR): Area and mass location aspects," *Sens. Actuators, A*, vol. 142, pp. 322-328, 2008.
- [35] R. Aigner, "SAW and BAW technologies for RF filter applications: A review of the relative strengths and weaknesses," in *Ultrasonics Symposium, 2008. IUS 2008. IEEE*, 2008, pp. 582-589.
- [36] S. H. Lee, E. W. Massey, R. S. Westafer, and W. D. Hunt, "A Novel Method to Investigate Dependence of SAW Resonator Sensor Signatures on Localized Surface Perturbations," in *Sensors, 2006. 5th IEEE Conference on*, 2006, pp. 1203-1206.
- [37] L. A. Beardslee, K. S. Demirci, Y. Luzinova, B. Mizaikoff, S. M. Heinrich, F. Josse, and O. Brand, "Liquid-Phase Chemical Sensing Using Lateral Mode Resonant Cantilevers," *Anal. Chem.*, vol. 82, pp. 7542-7549, 2010.
- [38] S. B. Truax, K. S. Demirci, L. A. Beardslee, Y. Luzinova, A. Hierlemann, B. Mizaikoff, and O. Brand, "Mass-Sensitive Detection of Gas-Phase Volatile Organics Using Disk Microresonators," *Anal. Chem.*, vol. 83, pp. 3305-3311, 2011.
- [39] R. Abdolvand and F. Ayazi, "Enhanced power handling and quality factor in thin-film piezoelectric-on-substrate resonators," in *IEEE Ultrasonics Symposium*, 2007, pp. 608-611.
- [40] J. Khan, R. H. Katz, and K. S. J. Pister, "Emerging Challenges: Mobile Networking for 'Smart Dust'," *Journal of Communications and Networks*, vol. 2, pp. 188-196, 2000.
- [41] W. Pan and F. Ayazi, "Thin-film piezoelectric-on-substrate resonators with Q enhancement and TCF reduction," in *Proc. IEEE MEMS*, 2010, pp. 727-730.
- [42] S. Trolier-McKinstry and P. Muralt, "Thin film piezoelectrics for MEMS," *Journal of Electroceramics*, vol. 12, pp. 7-17, 2004.
- [43] C. A. T. Center, *Zeolite, a Versatile Air Pollutant Adsorber*: US Environmental Protection Agency, Office of Air Quality Planning and Standards, 1998.
- [44] H. Huang, J. Zhou, S. Chen, L. Zeng, and Y. Huang, "A highly sensitive QCM sensor coated with Ag⁺-ZSM-5 film for medical diagnosis," *Sens. Actuators, B*, vol. 101, pp. 316-321, 2004.
- [45] S. Mintova and T. Bein, "Nanosized zeolite films for vapor-sensing applications," *Microporous and Mesoporous Materials*, vol. 50, pp. 159-166, 2001.
- [46] M. A. Urbiztondo, I. Pellejero, M. Villarroja, J. Sesé, M. P. Pina, I. Dufour, and J. Santamaría, "Zeolite-modified cantilevers for the sensing of nitrotoluene vapors," *Sens. Actuators, B*, vol. 137, pp. 608-616, 2009.

- [47] R. Binions, A. Afonja, S. Dungey, D. W. Lewis, I. P. Parkin, and D. E. Williams, "Discrimination Effects in Zeolite Modified Metal Oxide Semiconductor Gas Sensors," *IEEE Sensors J.*, vol. 11, pp. 1145-1151, 2011.
- [48] J.-C. Yang, "Nanoporous zeolite and solid-state electrochemical devices for nitrogen-oxide sensing," The Ohio State University, 2007.
- [49] A. L. Robinson, V. Stavila, T. R. Zeitler, M. I. White, S. M. Thornberg, J. A. Greathouse, and M. D. Allendorf, "Ultrasensitive Humidity Detection Using Metal–Organic Framework-Coated Microsensors," *Anal. Chem.*, vol. 84, pp. 7043-7051, 2012/08/21 2012.
- [50] M. D. Allendorf, R. J. T. Houk, L. Andruszkiewicz, A. A. Talin, J. Pikarsky, A. Choudhury, K. A. Gall, and P. J. Hesketh, "Stress-Induced Chemical Detection Using Flexible Metal–Organic Frameworks," *Journal of the American Chemical Society*, vol. 130, pp. 14404-14405, 2008.
- [51] A. H. Khoshaman and B. Bahreyni, "Application of Metal Organic Framework crystals for sensing of volatile organic Gases," in *Sensors, 2011 IEEE*, 2011, pp. 1101-1104.
- [52] G. Jasiński, P. Jasiński, and B. Chachulski, "Nano-porous alumina humidity sensors," *Metrology and Measurement Systems*, vol. 15, pp. 195-204, 2008.
- [53] M. Björkqvist, J. Paski, J. Salonen, and V.-P. Lehto, "Temperature dependence of thermally-carbonized porous silicon humidity sensor," *physica status solidi (a)*, vol. 202, pp. 1653-1657, 2005.
- [54] M. Haug, K. D. Schierbaum, G. Gauglitz, and W. Göpel, "Chemical sensors based upon polysiloxanes: comparison between optical, quartz microbalance, calorimetric, and capacitance sensors," *Sens. Actuators, B*, vol. 11, pp. 383-391, 1993.
- [55] K. Bodenhofer, A. Hierlemann, G. Noetzel, U. Weimar, and W. Gopel, "Performances of Mass-Sensitive Devices for Gas Sensing: Thickness Shear Mode and Surface Acoustic Wave Transducers," *Anal. Chem.*, vol. 68, pp. 2210-2218, 1996.
- [56] M. T. S. R. Gomes, P. S. T. Nogueira, and J. A. B. P. Oliveira, "Quantification of CO₂, SO₂, NH₃, and H₂S with a single coated piezoelectric quartz crystal," *Sens. Actuators, B*, vol. 68, pp. 218-222, 2000.
- [57] J. W. Grate and D. A. Nelson, "Sorptive polymeric materials and photopatterned films for gas phase chemical microsensors," *Proceedings of the IEEE*, vol. 91, pp. 881-889, 2003.
- [58] Z. Hao, R. Abdolvand, and F. Ayazi, "A High-Q Length-Extensional Bulk-Mode mass Sensor with Annexed Sensing Platforms," in *IEEE MEMS*, 2006, pp. 598-601.
- [59] R. Tabrizian, G. Casinovi, and F. Ayazi, "Temperature-stable high-Q AlN-on-silicon resonators with embedded array of oxide pillars," in *Solid-State Sensors, Actuators, and Microsystems Workshop*, Hilton Head, SC, 2010, pp. 100-101.
- [60] A. K. Samarao and F. Ayazi, "Temperature Compensation of Silicon Micromechanical Resonators via Degenerate Doping," in *IEEE Int. Electron Dev. Meeting*, 2009, pp. 789-792.

- [61] A. K. Samaroo, G. Casinovi, and F. Ayazi, "Passive TCF Compensation in High Q Silicon Micromechanical Resonators," in *IEEE Int. Conf. Microelectromech. Syst.*, Hong Kong, 2010, pp. 116-119.
- [62] M. G. Lawrence, "The Relationship between Relative Humidity and the Dewpoint Temperature in Moist Air: A Simple Conversion and Applications," *Bulletin of the American Meteorological Society*, vol. 86, pp. 225-233, February 01 2005.
- [63] L. Chen, C. Lee, and W. Cheng, "MEMS-based humidity sensor with integrated temperature compensation mechanism," *Sensors & Actuators: A. Physical*, vol. 147, pp. 522-528, 2008.
- [64] C. Jha, G. Bahl, R. Melamud, S. Chandorkar, M. Hopcroft, B. Kim, M. Agarwal, J. Salvia, H. Mehta, and T. Kenny, "CMOS-compatible dual-resonator MEMS temperature sensor with milli-degree accuracy," in *Proc. Transducers '07 & Eurosensors XXI*, 2007, pp. 10-14.
- [65] M. Penza and G. Cassano, "Relative humidity sensing by PVA-coated dual resonator SAW oscillator," *Sens. Actuators, B*, vol. 68, pp. 300-306, 2000.
- [66] M. Blaschke, T. Tille, P. Robertson, S. Mair, U. Weimar, and H. Ulmer, "MEMS Gas-Sensor Array for Monitoring the Perceived Car-Cabin Air Quality," *IEEE Sensors J.*, vol. 6, pp. 1298-1308, 2006.
- [67] R. Zhou, A. Hierlemann, U. Weimar, D. Schmeizer, and W. Gopel, "Mass Sensitive Detection Of CO₂ By Aminogroup-functionalized Polymers," in *Solid-State Sensors and Actuators, 1995 and Eurosensors IX. Transducers '95. The 8th International Conference on*, 1995, pp. 886-889.
- [68] N. Lazarus, S. S. Bedair, C. C. Lo, and G. K. Fedder, "CMOS-MEMS Capacitive Humidity Sensor," *J. Microelectromech. Syst.*, vol. 19, pp. 183-191, 2010.
- [69] B. Chachulski, J. Gebicki, G. Jasinski, P. Jasinski, and A. Nowakowski, "Properties of a polyethyleneimine-based sensor for measuring medium and high relative humidity," *Measurement Science and Technology*, vol. 17, pp. 12-16, 2006.
- [70] A. Schroth, K. Sager, G. Gerlach, A. Häberli, T. Boltshauser, and H. Baltes, "A resonant polyimide-based humidity sensor," *Sens. Actuators, B*, vol. 34, pp. 301-304, 1996.
- [71] A. Glück, W. Halder, G. Lindner, H. Müller, and P. Weindler, "PVDF-excited resonance sensors for gas flow and humidity measurements," *Sens. Actuators, B*, vol. 19, pp. 554-557, 1994.
- [72] B. Morten, G. De Cicco, and M. Prudenziati, "A thick-film resonant sensor for humidity measurements," *Sens. Actuators, A*, vol. 37-38, pp. 337-342, 1993.
- [73] R. Henderson. (2004) Gas Detection for VOC Measurement. *Occupational Health & Safety*.

- [74] M. Pardo, L. Sorenson, and F. Ayazi, "An Empirical Phase-Noise Model for MEMS Oscillators Operating in Nonlinear Regime," *IEEE Transactions on Circuits and Systems I*, vol. 59, pp. 979-988, 2012.
- [75] M. J. Dalal, J. L. Fu, and F. Ayazi, "Simultaneous dual-mode excitation of piezo-on-silicon micromechanical oscillator for self-temperature sensing," in *Proc. IEEE MEMS*, Cancun, Mexico, 2011, pp. 489-492.
- [76] J. L. Fu and F. Ayazi, "Dual-mode piezo-on-silicon resonant temperature and humidity sensor for portable air quality monitoring systems," in *Proc. IEEE SENSORS Conf.*, Hawaii, 2010, pp. 2131-2135.
- [77] "Top 20 Indoor Chemical Pollutants," *Air Quality Sciences*. Available: <http://www.aeris.org/DesktopDefault.aspx?tabindex=2&tabid=64>
- [78] M. L. Johnston, H. Edrees, I. Kymissis, and K. L. Shepard, "Integrated VOC vapor sensing on FBAR-CMOS array," in *Micro Electro Mechanical Systems (MEMS), 2012 IEEE 25th International Conference on*, 2012, pp. 846-849.
- [79] A. Hajjam, A. Logan, and S. Pourkamali, "Fabrication and characterization of MEMS-based resonant organic gas sniffers," in *Sensors, 2011 IEEE*, 2011, pp. 1105-1108.
- [80] W. Montes and T. C. Marsh, "Printing Non-Polar Polymers Using the BioForce Nano eNabler Open Channel Micro-patterning Tool," BioForce Nanosciences Application Note, 2008.
- [81] L. A. Beardslee, S. Truax, J. H. Lee, S. Pavlidis, P. Hesketh, K. M. Hansen, R. Kramer, and O. Brand, "Selectivity enhancement strategy for cantilever-based gas-phase VOC sensors through use of peptide-functionalized carbon nanotubes," in *Proc. IEEE MEMS*, 2011, pp. 964-967.
- [82] Y. Kurihara, T. Endoh, and K. Yamada, "The influence of moisture on surface properties and insulation characteristics of AlN substrates," *Components, Hybrids, and Manufacturing Technology, IEEE Transactions on*, vol. 12, pp. 330-334, 1989.
- [83] M. Konno, T. Ikehara, S. Murakami, R. Maeda, M. Kimura, T. Fukawa, and T. Mihara, "Novel MEMS oscillator using in-plane disk resonator with sensing platform and its mass sensing characteristics," in *16th International Solid-State Sensors, Actuators and Microsystems Conference (TRANSDUCERS)*, 2011, pp. 518-521.
- [84] H. Debéda, R. Lakhmi, C. Lucat, and I. Dufour, "Use of the longitudinal mode of screen-printed piezoelectric cantilevers coated with PEUT for toluene detection: comparison with silicon cantilevers," *Sens. Actuators, B*, 2013.
- [85] I. Sayago, M. J. Fernández, J. L. Fontecha, M. C. Horrillo, C. Vera, I. Obieta, and I. Bustero, "Surface acoustic wave gas sensors based on polyisobutylene and carbon nanotube composites," *Sens. Actuators, B*, vol. 156, pp. 1-5, 8/10/ 2011.
- [86] P. Si, J. Mortensen, A. Komolov, J. Denborg, and P. J. Møller, "Polymer coated quartz crystal microbalance sensors for detection of volatile organic compounds in gas mixtures," *Analytica Chimica Acta*, vol. 597, pp. 223-230, 8/10/ 2007.

- [87] A. K. Samarao and F. Ayazi, "Temperature Compensation of Silicon Resonators via Degenerate Doping," *Electron Devices, IEEE Transactions on*, vol. 59, pp. 87-93, 2012.
- [88] K. Lakin, K. McCarron, and J. McDonald, "Temperature compensated bulk acoustic thin film resonators," in *Proc. IEEE Ultrason.Symp.*, 2000, pp. 855-858.
- [89] R. Melamud, P.M. Hagelin, C.M. Arft, C. Grosjean, N. Arumugam, P. Gupta, G. Hill, M. Lutz, and a. F. A. A. Partridge, "MEMS enables oscillators with sub-ppm frequency stability and sub-ps jitter," in *Solid-State Sensors, Actuators, and Microsystems Workshop*, Hilton Head, SC, 2012, pp. 66-69.
- [90] K. Sundaresan, G. K. Ho, S. Pourkamali, and F. Ayazi, "Electronically temperature-compensated silicon bulk acoustic resonator reference oscillators," *IEEE Journal of Solid-State Circuits*, vol. 42, pp. 1425-1434, 2007.
- [91] H. M. Lavasani, W. Pan, B. P. Harrington, R. Abdolvand, and F. Ayazi, "Electronic temperature compensation of lateral bulk acoustic resonator reference oscillators using enhanced series tuning technique," *IEEE Journal of Solid-State Circuits*, vol. 47, pp. 1381-1393, 2012.
- [92] J. A. Kusters, M. C. Fischer, and J. G. Leach, "Dual mode operation of temperature and stress compensated crystals," in *32nd Annual Symposium on Frequency Control. 1978*, 1978, pp. 389-397.
- [93] B. K. Sinha, "Stress Compensated Orientations for Thickness-Shear Quartz Resonators," in *Thirty Fifth Annual Frequency Control Symposium. 1981*, 1981, pp. 213-221.
- [94] R. Besson, J. Boy, B. Glotin, Y. Jinzaki, B. Sinha, and M. Valdois, "A dual-mode thickness-shear quartz pressure sensor," *IEEE Trans. Ultrason. Ferroelect. Freq. Control*, vol. 40, pp. 584-591, 1993.
- [95] A. V. Kosykh, I. V. Abramson, and R. P. Bagaev, "Dual-mode crystal oscillators with resonators excited on B and C modes," in *Frequency Control Symposium, 1994. 48th., Proceedings of the 1994 IEEE International*, 1994, pp. 578-586.
- [96] S. S. Schodowski, "Resonator self-temperature-sensing using a dual-harmonic-mode crystal oscillator," in *Frequency Control, 1989., Proceedings of the 43rd Annual Symposium on*, 1989, pp. 2-7.
- [97] M. Koskenvuori, V. Kaajakari, T. Mattila, and I. Tittonen, "Temperature measurement and compensation based on two vibrating modes of a bulk acoustic mode microresonator," in *IEEE MEMS*, 2008, pp. 78-81.
- [98] R. Abdolvand, H. Mirilavasani, and F. Ayazi, "Single-Resonator Dual-Frequency Thin-Film Piezoelectric-on-Substrate Oscillator," in *IEEE International Electron Devices Meeting, IEDM*, 2007, pp. 419-422.
- [99] R. Meyer and A. Wong, "Blocking and desensitization in RF amplifiers," *IEEE Journal of Solid-State Circuits*, vol. 30, pp. 944-946, 1995.

- [100] R. Poore, "Accurate simulation of mixer noise and oscillator phase noise in large RFICs," in *Microwave Conference Proceedings, 1997. APMC '97, 1997 Asia-Pacific, 1997*, pp. 357-360 vol.1.
- [101] C. Bourgeois, E. Steinsland, N. Blanc, and N. F. de Rooij, "Design of resonators for the determination of the temperature coefficients of elastic constants of monocrystalline silicon," in *Frequency Control Symposium, 1997., Proceedings of the 1997 IEEE International*, 1997, pp. 791-799.
- [102] J. P. Valentin, C. P. Guerin, and R. J. Besson, "Indirect Amplitude Frequency Effect in Resonators Working on Two Frequencies," in *Thirty-Fifth Annual Frequency Control Symposium*, 1981, pp. 122-129.
- [103] H. J. McSkimin, "Measurement of Elastic Constants at Low Temperatures by Means of Ultrasonic Waves--Data for Silicon and Germanium Single Crystals, and for Fused Silica," *J. Appl. Phys.*, vol. 24, pp. 988-997, 1953.
- [104] T. Pensala, A. Jaakkola, M. Prunnila, and J. Dekker, "Temperature compensation of silicon MEMS Resonators by Heavy Doping," in *Ultrasonics Symposium (IUS), 2011 IEEE International*, 2011, pp. 1952-1955.
- [105] A. K. Samarao, G. Casinovi, and F. Ayazi, "Passive TCF compensation in high Q silicon micromechanical resonators," 2010, pp. 116-119.
- [106] D. E. Newland, "Pedestrian excitation of bridges—recent results," in *Tenth International Congress on Sound and Vibration*, 2003, pp. 1–15.
- [107] S. Roundy, "On the Effectiveness of Vibration-based Energy Harvesting," *Journal of Intelligent Material Systems and Structures*, vol. 16, p. 809, 2005.
- [108] R. Elfrink, V. Pop, D. Hohlfeld, T. M. Kamel, S. Matova, C. de Nooijer, M. Jambunathan, M. Goedbloed, L. Caballero, M. Renaud, J. Penders, and R. van Schaijk, "First autonomous wireless sensor node powered by a vacuum-packaged piezoelectric MEMS energy harvester," in *IEDM 2009*, 2009, pp. 1-4.
- [109] C. B. Williams, C. Shearwood, M. A. Harradine, P. H. Mellor, T. S. Birch, and R. B. Yates, "Development of an electromagnetic micro-generator," *Circuits, Devices and Systems, IEEE Proceedings*, vol. 148, pp. 337-342, 2001.
- [110] T. Galchev, H. Kim, and K. Najafi, "Non-resonant bi-stable frequency-increased power scavenger from low-frequency ambient vibration," in *Transducers 2009*, 2009, pp. 632-635.
- [111] I. Sari, T. Balkan, and H. Kulah, "An Electromagnetic Micro Power Generator for Low-Frequency Environmental Vibrations Based on the Frequency Upconversion Technique," *J. Microelectromech. Sys.*, vol. 19, pp. 14-27, 2010.
- [112] R. Elfrink, V. Pop, D. Hohlfeld, T. M. Kamel, S. Matova, C. de Nooijer, M. Jambunathan, M. Goedbloed, L. Caballero, M. Renaud, J. Penders, and R. van Schaijk, "First autonomous wireless sensor node powered by a vacuum-packaged piezoelectric MEMS energy harvester," in *IEEE International Electron Devices Meeting (IEDM)*, 2009, pp. 1-4.

- [113] I. Sari, T. Balkan, and H. Kulah, "An Electromagnetic Micro Power Generator for Low-Frequency Environmental Vibrations Based on the Frequency Upconversion Technique," *Journal of Microelectromechanical Systems*, vol. 19, pp. 14-27, 2010.
- [114] P. Monajemi, P. J. Joseph, P. A. Kohl, and F. Ayazi, "Wafer-level MEMS packaging via thermally released metal-organic membranes," *J. Micromech. Microeng.*, vol. 16, pp. 742-750, 2006.